CURING NANO-FILLED THERMOSETTING RESINS WITH RF FIELDS FOR ADVANCED MANUFACTURING SIMULATIONS AND EXPERIMENTS

A Thesis

by

SUCHI K. DESAI

Submitted to the Graduate and Professional School of
Texas A&M University
in partial fulfillment of the requirements for the degree of

MASTER OF SCIENCE

Chair of Committee,	Micah Green
Committee Members,	Mohammad Naraghi
	Hung-Jen Wu
Head of Department,	Victor Ugaz

August 2022

Major Subject: Chemical Engineering

ABSTRACT

In this report, we study the reaction kinetics of bisphenol A diglycidyl ether (DGEBA) and a curing agent (Jeffamine T403) and demonstrate new techniques to print multi-layered structures using localized RF heating and curing.

We first characterized isothermal curing of DGEBA resin using rheometry and Differential Scanning Calorimetry to understand the curing kinetics. The *in situ* curing behavior of RF-heated DGEBA-CNT resin was monitored using a rheometer to show that RF heating allows for rapid volumetric heating and curing of thermosetting resins.

We developed a technique to build up a multi-layered printed structure using RF heating and localized curing. Multi-layered structures were printed by moving the RF applicator relative to the resin reservoir, selectively curing the resin exposed to the field; this process was repeated for each layer. Thermal and mechanical characterization was performed for RF printed samples, and conventionally cured (oven-cured) samples. The two samples show similar glass transition temperatures and storage moduli, but the RF-heated samples show a more uniform morphology and better mechanical properties. The selective curing process was also modeled using multiphysics simulation of curing kinetics and heat transfer; the simulation calculates the conversion and temperature at each point in space and time. Simulation results show that our proposed technique can be used to create complex structures like the Texas A&M logo, thus demonstrating the scope of this method in printing complex structures.

In the last study, currently in progress, we demonstrate that the use of a co-planar RF applicator, which generates an electric field, to rapidly heat and cure DIW-printed, nano-filled epoxy composites. This proposed method involves a layer-by-layer, print and cure cycle which

allows for printing high resolution, multi-layered structures. Here, each printed layer is partially cured using RF heating before a new layer is deposited. This print-and-cure cycle allows the printed structure to maintain its integrity and hold its own weight without collapsing as subsequent layers are printed. Commercial epoxy resin with varied nano-filler loadings were examined as DIW candidates. Rheological characterization was used to assess curing kinetics and printing behavior, and RF sweeps were used to determine RF heating capabilities of the candidate resins. After printing, the thermo-mechanical properties, surface finish, and shape retention of RF-cured samples were evaluated and found to be comparable against samples conventionally cured in an oven. This method of manufacturing establishes RF heating as a suitable alternative to conventional methods, thereby facilitating rapid, free-form processing of thermosetting resins.

Acknowledgements

I would like to thank my principal investigator and committee chair, Dr. Micah Green for his guidance, inspiration, and support in the completion of my thesis. Dr. Green has always challenged me to push my limits and nudged me in the right direction through his research insights and constructive criticism. Dr. Green has made my graduate school experience both enjoyable and fulfilling and I am grateful for all that he has done for me as an academic advisor.

I would also like to thank Dr. Naraghi and Dr. Wu for taking precious time out of their busy schedule and agreeing to be a part of my committee. In addition, I am also grateful to Ashley Henley for helping me out with the forms, signatures, and documentations required at every step of my master's journey.

I would like to express my appreciation to Anubhav Sarmah for being my mentor and training me on all the required equipment's in our laboratory. I would like to pay special regards to my research group colleagues Dr. Guler Bengusu Tezel, Gabriel Zolton, Ethan Harkin, and Kailash Arole for helping me with their research advice. I am also thankful to other members of the group for their constructive feedback during group meetings. I feel lucky to have found such great friends, colleagues and mentors at Texas A&M University who supported me through my master's journey.

Lastly, I would like to thank my constant support system, my mom and dad; as well as my best friends Evan Sonnier and Michaela Patterson. You all have pushed me through the years to achieve more than I thought was possible.

Contributors

This work was supervised by a thesis committee consisting of my advisor, Dr. Micah Green from Artie McFerrin department of Chemical engineering and my committee members, Dr. Mohammad Naraghi from Department of Aerospace Engineering and Dr. Hung-Jen Wu from Department of Chemical Engineering at Texas A&M University.

My training was administered by Anubhav Sarmah, a Chemical Engineering Ph.D. candidate in Dr. Green's research group when I joined the group. Characterization experiments mentioned in this study were performed by Anubhav Sarmah while I assisted as I was an undergraduate student when most of these experiments were performed.

Rheology experiments mentioned in Chapter 2 were performed by a team of three: Anubhav Sarmah, Dr. Guler Bengusu Tezel, a visiting Chemical Engineering professor from Turkey, and myself. Rheology experiments mentioned in Chapter 4 were also performed by a team of three: Anubhav Sarmah, Ava Crowley, an undergraduate Chemical Engineering student in Dr. Green's research group, and myself.

I would also like to extend thanks to Ethan Harkin and Gabriel Zolton for assisting me during printing experiments mentioned in Chapter 4 and operating the HyRel printer. Scanning Electron Microscopy images data was provided by Kailash Arole, a Chemical Engineering Ph.D. candidate in Dr. Green's research group.

All other work conducted for the thesis was completed by the student independently.

Funding Sources

This graduate study was not supported by any funding sources.

Nomenclature

RF	Radio Frequency
CNT	Carbon nanotubes
MWCNTs	Multi-walled carbon nanotubes
DGEBA	Bisphenol A diglycidyl ether
DIW	Direct Ink Write

Table of Contents

	Page
Abstract	ii
Acknowledgements	iv
Contributors	v
Nomenclature	vi
List of Figures	ix
List of Tables	xiv
Chapter 1: Background	1
1.1: Importance of thermosetting polymers in industry	1
1.2: Chemistry and curing kinetics of thermosetting resins	1
1.3: Current manufacturing	2
1.4: Radio Frequency heating	4
Chapter 2: Kinetics of carbon nanotube-loaded epoxy curing: rheometry, differential scanning calorimetry, and radio frequency heating	9
2.1: Experimental methods	9
2.2: Results and Discussion	11
2.3: Conclusion	30
Chapter 3: Rapid manufacturing via selective Radio Frequency heating and curing of thermosetting resins	31
3.1: Experimental methods	31
3.2: Results and Discussion	37
3.3: Conclusion	59
Chapter 4: Additive manufacturing of thermosetting resins using Direct Ink Write printing and RF heating	60
4.1: Experimental methods	61
4.2: Results and Discussion	68

4.3: Conclusion…… 83

Chapter 5: Thesis Conclusion……. 85

Appendix: MATLAB codes……. 88

References…… 102

List of Figures

Figure 1.1 Model truck (A) was bisected by cutting the truck bed off. (B) Truck and bed interface was filled with CNT-loaded Betamate epoxy and connected to the RF source. (C) Interface containing the epoxy rapidly heated and the temperature was monitored with the FLIR camera. (D) Finished, welded truck was able to support weight (1.4 kg) in the truck bed……6

Figure 1.2 (A) Temperature vs time response for varying wt % of Hi-Nicalon fibers in polycarbosilane aligned parallel to the field. (B) FTIR spectrum showing extent of curing of polycarbosilanes: 20 wt % fibers in polycarbosilane cured completely. (C) FLIR image showing heating of fiber on fringing field applicator. (D) SEM image of resulting composite for 20 wt % SiC fibers in PCS [20]……7

Figure 1.3 When graphene oxide (GO) is exposed to RF waves, the GO samples are reduced by the RF treatment. RF waves resistively heat GO with electric fields in seconds to form reduced GO [18]……7

Figure 2.1 (a) Schematic showing out-of-oven RF-assisted curing and printing in resin bath. The RF applicator is moved relative to the resin at a constant speed using a linear stage to print a continuous sample, (b) Cross-section view shows the fringing field heating the filled resin and allowing the sample to cure……10

Figure 2.2 The variation of G' and G'' moduli with curing time at different temperatures at (a) 80 $^{\circ}$C, (b) 90 $^{\circ}$C, (c) 100 $^{\circ}$C, (d) 110 $^{\circ}$C……12

Figure 2.3 (a) The variation of complex viscosity with curing time at different temperatures and (b) Initial complex viscosity values at t = 10 s measured at different temperatures……13

Figure 2.4 Variation of degree of cure, a with curing time at different curing temperatures. Computed from Figure 3.2 data using equation (2.2)……13

Figure 2.5 Curing rate, da/dt versus degree of cure, a, of Epoxy- CNT sample at different temperatures (a) 80 $^{\circ}$C, (b) 90 $^{\circ}$C, (c)100 $^{\circ}$C, (d) 110 $^{\circ}$C in rheometer. The solid curves are fitting results from model equation, and the symbols are experimental data……15

Figure 2.6 Arrhenius plot of epoxy-5%CNT system using (a) Rheometer and (b) DSC measurements. Reaction rate constants, (k values) listed in Tables 3.1 and 3.2 are plotted as functions of temperature……17

Figure 2.7 Differential scanning calorimetry heat flow curve of epoxy-5%CNT for isothermal curing at 80 °C, 90 °C, 100 °C, 110 °C……19

Figure 2.8 Variation of degree of cure, a with curing time at different curing temperatures using DSC. Computed from Figure 3.7 data using equation (2.5)……20

Figure 2.9 Curing rate, da/dt, versus degree of cure, a, of epoxy-CNT sample at different temperatures (a) 80 °C, (b) 90 °C, (c) 100 °C, (d) 110 °C in DSC. The solid curves are fitting results from model equation, and the symbols are experimental data……21

Figure 2.10 Temperature vs. time plot of CNT-loaded epoxy heated using Radio Frequency field and maintained at target temperatures (a) 90 ^{o}C (b)100 ^{o}C, (c)110 ^{o}C (d) 120 ^{o}C for 1 minute. Thermal images captured after reaching target temperatures using FLIR camera……25

Figure 2.11 G' and G'' variations with RF exposure times at different temperatures (a) 90 $^{\circ}$C, (b) 100 $^{\circ}$C, (c) 110 $^{\circ}$C, (d) 120 $^{\circ}$C. At t = 0, RF time (min) axis shows the value of G', G'' of epoxy-CNT at 25 $^{\circ}$C. RF heated sample is loaded rapidly in a pre-heated rheometer; G', G'' values are reported from the starting point of rheological measurements……27

Figure 2.12 Complex viscosity variations with RF heating times at different temperatures. At t = 0 on RF time (min) axis shows the value of complex viscosity value of epoxy-CNT at 25 $^{\circ}$C. RF heated sample is loaded rapidly in a pre-heated rheometer; complex viscosity values are reported from the starting measurement points of rheological measurements……28

Figure 3.1 Schematic representing multi-layered additive manufacturing of thermosetting epoxy resin using radio-frequency assisted heating and curing. (A) Cross-sectional view of an RF applicator curing a structure in one layer of uncured resin; (B) Structure formed after repeated additions of uncured resin layers and selectively RF heating it to form a multi-layered structure; (C) Final cured structure extracted from a reservoir of uncured epoxy……36

Figure 3.2 Maximum temperature vs. time plot for stationary RF heating of 5 wt.% CNT loaded epoxy resin. Power modulated to maintain T_{target} = 250 °C (marked in red). Inset: thermal image at steady state captured using FLIR camera……38

Figure 3.3 (a) Maximum temperature vs. time plot of 1D scan (0.067 mm/s) and print of 5 wt.% CNT loaded epoxy resin using RF heating. Inset: the printed 1D sample with dimensions of 34 mm x 5 mm, (b) 2D ring printed from a reservoir of epoxy using RF heating and curing. The RF applicator was moved relative to a resin reservoir using an x-y stage to induce localized heating and curing. Dimensions of printed structure: 15 mm inner radius, 20 mm outer radius……39

Figure 3.4 (a) The cross-sectional view of a multi-layer 1D print with a thickness of 0.8 mm for each layer, (b) Epoxy curing in a reservoir with selective, localized heating. The RF applicator was moved relative to a resin reservoir using a linear stage to induce localized heating and curing. Uncured resin in the reservoir washed away using acetone……41

Figure 3.5 Target Zone and Hot Zone (due to diffusion) of the resin during RF Heating……42

Figure 3.6 Thermo-Gravimetric Analysis (TGA) plots for samples cured using RF heating, RF heating followed by oven post-cure, and conventional oven curing……43

Figure 3.7 Differential Scanning Calorimetry (DSC) plots for samples cured using RF heating, RF heating followed by oven post-cure, and conventional oven curing……44

Figure 3.8 Dynamic Mechanical Analysis (DMA) plots for samples cured using (a) RF heating, (b) RF heating followed by oven post-cure, and (c) conventional oven curing. A 17.5 mm single cantilever beam procedure was followed at frequency of 1 Hz……46

Figure 3.9 Scanning Electron Microscopy (SEM) images of cross-section of nano-filled epoxy sample cured using (a, c) RF heating, and (b, d) conventional oven curing……48

Figure 3.10 Mechanial Testing of samples cured using RF Heating and Oven Heating……49

Figure 3.11 Absorbance vs wavelength of uncured resin immediately after making sample and 30 minutes after making the sample……50

Figure 3.12 (a) Maximum temperature vs. time plot of localized heating and curing of a stationary resin sample (the power is on for 600 seconds). (b) Surface plot of conversion changing with time at fixed point in space (y-direction)……52

Figure 3.13 Maximum temperature vs. time plot of localized heating and curing of a 1D line with a length of 18 mm. This graph corresponds to Figure 3.14……53

Figure 3.14 Surface plot of temperature and conversion changing with time (t = 150s, 300 s, 550 s) and space to print a 1D line with a length of 18 mm. The heat source was moved relative to the resin at a speed of 0.033 mm/s……54

Figure 3.15 Maximum temperature vs. time plot of localized heating and curing of a 2D circle with a radius of 10 mm. This graph corresponds to Figure 3.16……54

Figure 3.16 Surface plot of temperature and conversion changing with time (t = 450 s, 900 s, 1800 s) and space to print a 2D circle with a radius of 10 mm. The heat source was moved relative to the resin at a speed of 0.033 mm/s……55

Figure 3.17 (a) Surface plot of conversion in space for the Texas A&M logo printed using localized heating and curing. Each letter of the logo was printed separately; (b) The post-cure and post-extraction surface plot of the final printed structure……56

Figure 3.18 Plot of the x and y locations of the input heat source path. This graph corresponds to Figure 3.17……57

Figure 3.19 Simulation of 3D-printed helical spring: (Top) Plot of the (x,y,z) locations of the input heat source path for the 3D spring. Red dots indicate cured locations. (Bottom) X(x,y) at different z-slices for the final cured part……58

Figure 4.1 Schematic representing the direct-ink write printing process using radio-frequency assisted heating and curing. Step 1 represents the DIW printing process; step 2 demonstrates the RF heating and partial curing process; and step 3: shows the deposition of a new printed layer, after which the print-and-cure cycle is repeated…….63

Figure 4.2 Schematic of simulation system. A two-dimensional (x-z) system with thermal transport (Q_{ext}) in the y-direction……66

Figure 4.3 Yield stress obtained from oscillatory stress sweeps for varied CNT loadings (3 wt.%, 4 wt.%, 5 wt.%, and 7 wt.%)……69

Figure 4.4 Three interval stead-shear thixotropy results for varied CNT loadings (3 wt.%, 4 wt.%, 5 wt.%, and 7 wt.%). The three regions in this test are as follows: an initial rest period (0.01 s^{-1}), a high shear-rate step (1000 s^{-1}), and the recovery period (0.01 s^{-1})……70

Figure 4.5 Maximum heating rate calculated for varied CNT loadings (3 wt.%, 4 wt.%, 5 wt.%, and 7 wt.%). Radio-frequency sweeps were performed with a constant power of 1 watt and frequencies ranging from 0-200 MHz……71

Figure 4.6 Dynamic Mechanical Analysis (DMA) plots for samples manufactured using (a) DIW printing and RF heating and curing, and (b) conventional oven curing in a mold. A 35 mm dual cantilever beam procedure was followed at frequency of 1 Hz……72

Figure 4.7 Scanning Electron Microscopy (SEM) images of cross-section of nano-filled epoxy sample manufactured using conventional oven curing in a mold (a-b), and DIW printing and RF heating (c-d)……..74

Figure 4.8 Tensile testing results for ASTM D638 type IV tensile bars manufactured using DIW printing and RF heating, and conventional oven curing in a mold using an Instron load frame with a 30 kN load cell……..75

Figure 4.9 Wall printed (a) without RF partial cure after each printed layer (collapsed after 6 layers), and (b) with RF partial cure after each printed layer (structure did not collapse after 10 printed layers)……..76

Figure 4.10 Structures manufactured using direct ink write printing and RF heating and curing. (a) Single-trace hexagon with 3 printed layers of height 0.1 mm per layer. (b) Cylinder with 12 layers of height 0.2 mm per layer. (c) A complex gear print with 3 layers of height 0.1 mm per layer……78

Figure 4.11 Surface plot of temperature and conversion of a wall changing with time (t = 1750 seconds, 3500 seconds, 7000 seconds) and space……79

Figure 4.12 Surface plot of conversion as a function of space at final time. The structures have a layer height of (a) 0.001 m, and (b) 0.002 m. Other parameters like residence time, target temperature, and system parameters remain unchanged……..80

Figure 4.13 (a) Surface plot of conversion of a cylinder as a function of space at final time, and (b) surface plot of temperature of a cylinder as a function of space at halfway time……81

Figure 4.14 (a) Surface plot of conversion of a turret as a function of space at final time, and (b) Plot of the x and y locations of the input print path and heat source path……..82

List of Tables

Table 2.1 Kamal-Sourour model kinetic parameters at different isothermal curing temperatures…… 16

Table 2.2 Model kinetic parameters from DSC at different isothermal curing temperatures……22

Table 2.3 Comparison of G′ and G″ values for RF heating and without RF heating……29

Table 3.1 Glass Transition Temperatures measured using Differential Scanning Calorimetry for samples cured using RF heating, RF heating followed by post curing in an oven, and conventional oven curing……..44

Chapter 1: Background

1.1. Importance of thermosetting polymers in industry

Thermosetting polymers are stable, high-performance materials that are crosslinked by heating and curing. Cured thermoset structures are valuable because they are mechanically strong with superior strength, and hardness, as well as highly resistant to thermal and chemical degradation. These properties make thermoset composites a popular choice for a wide range of applications such as electronics, construction equipment panels, heat resistant shields, and various parts in the automotive and aerospace industries. Applications of thermosetting materials range from battery frameworks to aerospace and automotive structures [1].

1.2. Chemistry and curing kinetics of thermosetting resins

Thermoset resins, in an uncured state, exist as monomers in a liquid state. As the curing reaction progresses, the polymer chains begin to form a crosslinked network. After this point, the liquid or rubbery resin gradually becomes solidified as the space for segment mobility decreases due to formation of a crosslinked network. The curing reaction for thermosetting polymers is an irreversible reaction, i.e., once the resin is crosslinked to form a solid structure, the crosslinked structure is semi-permanent [2].

The curing reaction kinetics have been studied previously, and several models have been developed to assess the degree of cure for a polymer as it is undergoing the curing process. One of the models used often is the Kamal model [3], and its modified version, known as the Kamal-Sourour model (**Equation 1.1 and 1.2** respectively).

$$\frac{d\alpha}{dt} = (k_1 + k_2\alpha^m)(1-\alpha)^n \qquad (1.1)$$

$$\frac{d\alpha}{dt} = (k\alpha^m)(1-\alpha)^n \qquad (1.2)$$

Here, α is the degree of cure, $d\alpha/dt$ is the curing rate, k_1 and k_2 are the reaction rate constants, and *m* and *n* are empirical reaction constants that reflect reaction orders and define the initiation and propagation stages of curing. This model differs from traditional reaction rate equations seen in chemical engineering [for example: rate = $k\alpha$]. The primary difference lies in the term $(1-\alpha)$, which signifies that when the degree of cure, α, is either zero or 1, the curing rate becomes zero. This means that the reaction rate will approach a maximum value when the degree of cure is greater than zero, and less than 1. Thus, when the degree of cure is zero, and the polymer is in a liquid state, the curing reaction will not progress; there needs to be some degree of cure for the reaction to progress. This also means that there must be some initial crosslinking of the monomers present in the liquid state to start the curing reaction. Similarly, as the degree of cure approaches 1, the crosslinking process solidifies the structure, which results in a lack of remaining crosslinkable groups; thus, slowing down the curing reaction until it ultimately ceases.

The temperature at which the thermosetting polymer is cured has a significant impact on the curing process, and the rate of the curing reaction. Previous studies have shown that the reaction rate is significantly slower at lower temperatures (at $T < 50$ °C the time required to cure completely is ~24 hours), whereas higher temperatures increase the curing reaction rate, and thus, decrease the time required to cure the polymer. The curing reaction is an exothermic reaction, as such, it can cause the reaction to run away if the heat of reaction generated from the curing process overwhelms the system.

1.3. Current manufacturing

The conventional manufacturing process for thermosetting epoxy resins involves designing and producing molds, followed by curing of the resin matrix in such molds using high

temperature ovens. The curing schedules required often last for 24-48 hours, thus, making this process energy, labor, and time consuming. The current conventional methods also set limits on achievable part geometries and processing times due to a dependence on molds [4, 5]. Furthermore, curing of thermoset part in an oven can lead to possible introduction of voids in the structure, which affects the structural integrity of the final part. The cause of void formation is the convective nature of oven heating which causes the outer layer of the sample to heat and cure before the interior layers, thereby resulting in trapped air within the cured structure.

One of the applications of thermosetting epoxies in industry is in carbon fiber composites. Fiber reinforced composites are composed of a stiffer fiber, like carbon fiber, that is embedded in a softer matrix, like epoxy resins [6, 7]. Carbon-epoxy composites demonstrate high specific stiffness and specific strength, which makes them suitable for production of light-weight structures with higher load-bearing capacities [8]. Such mechanical properties have made carbon-epoxy composites an integral part in automotive, aerospace, and marine industries, civil engineering applications, as well as sports equipment and other technical applications [9].

Recently, various nanofillers have been dispersed in polymer matrices to improve the mechanical, thermal, and electrical properties of the final material for industrial applications. The common fillers used for polymer reinforcement include carbon black, graphene, graphene oxide, and layered silicate nano-clay [10, 11]. For lightweight polymer nanocomposites, CNTs are one the best contenders due to their superior thermal and electrical characteristics, as well as their enhanced strength and high specific stiffness [12]. CNTs are unique tubular structures of nanometer diameter and high aspect ratio, as well as a high surface-to-volume ratio [13]. The elemental carbon in the sp^2 hybridization can form honeycomb atomic arrangements; this

graphite-like atomic arrangement of carbon atoms in CNTs results in amazing mechanical properties, with the average value for Young's modulus of isolated single walled carbon nanotubes (SWCNTs) being ~1.25 TPa [14].

Despite their numerous applications and enhanced properties, epoxy-CNT composites also pose unique challenges. One of these challenges includes control of dispersion of the nanotubes in the resin. If the dispersion is not controlled, it leads to reduced performance of the nano-filler, and reduced reproducibility of experiments, thereby resulting in discrepancies amongst previous studies on carbon nanocomposites [15]. In almost all prior work with nanocomposites, the nanomaterial is added to the resin to improve the final material properties, like mechanical strength, and conductivity; however, in our case, we focus on using the filler to enable new methods of processing resins.

1.4. Radio Frequency heating

RF waves are electromagnetic fields with a frequency within the range of 20 kHz to 300 GHz. Previous studies focus on the use of microwaves, but more recently, our group has shown that carbon nanomaterials heat up rapidly in response to RF fields [5, 6, 16-21]. RF waves allow for a safer and more versatile alternative compares to microwaves. RF susceptor materials include graphite, graphene oxide, laser-induced graphene, carbon black and carbon fibers. These conductive materials, when dispersed in polymer matrices, heat rapidly when exposed to RF waves.

RF heating offers several benefits. Dielectric heating using RF fields can help avoid numerous challenges faced by conventional methods of heating. Advantages include volumetric and targeted heating. Bulk specimen with RF susceptors can be heated volumetrically, or inside-

to-outside, using RF fields; this method reduces the need for large ovens or furnaces to heat the specimens. For applications that require heating on specific locations like bonding, RF fields provide targeted heating. Targeted heating avoids the need to heat the entire structure, which can introduce residual thermal stresses in the assembly once it cools. Other key benefits offered by RF heating include greater penetration depths than microwaves, which allows for better heating in thicker materials. RF waves are also capable of better selectivity [22].

RF heating has shown potential to reduce fabrication time and provide an energy efficient alternative for numerous applications. Applications include materials processing where targeted and volumetric heating are needed such as inter-layer adhesions in 3D printed thermoplastics [5], bonding thermoplastic surfaces together (**Figure 1.1**) [21], curing pre-ceramic polymer composites (**Figure 1.2**) [20], reduction of graphene oxide (**Figure 1.3**) [18], and processing of thermosetting prepregs [6]. Compared to traditional heating and processing methods, RF heating provides faster heating rates with lower infrastructure requirements and better energy efficiency; non-contact RF applicators or capacitors can be used for out-of-oven processing, allowing for distributed manufacturing.

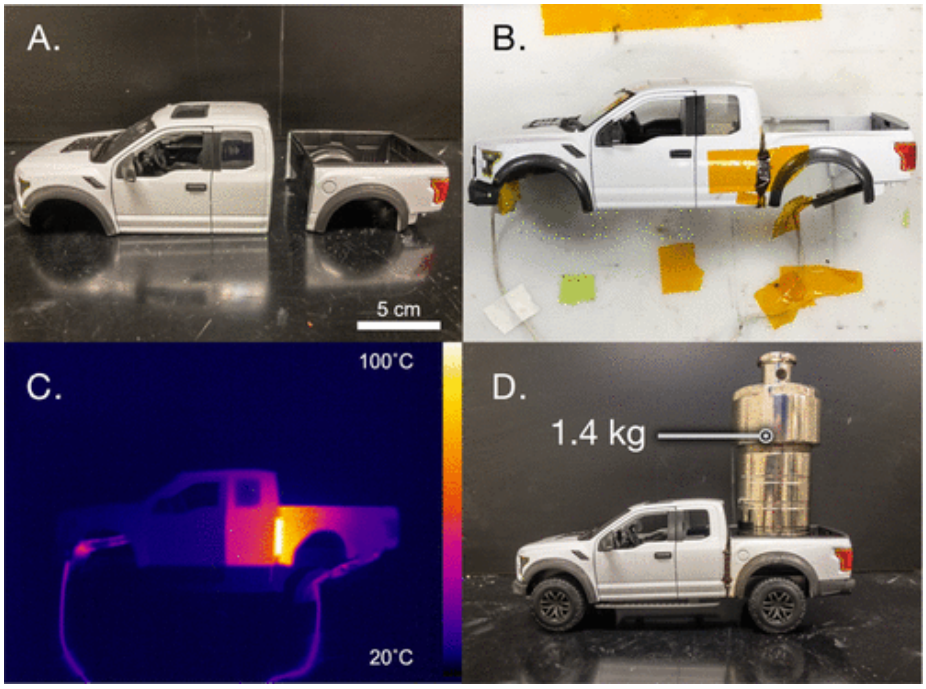

Figure 1.1: Model truck (A) was bisected by cutting the truck bed off. (B) Truck and bed interface was filled with CNT-loaded Betamate epoxy and connected to the RF source. (C) Interface containing the epoxy rapidly heated and the temperature was monitored with the FLIR camera. (D) Finished, welded truck was able to support weight (1.4 kg) in the truck bed [22].

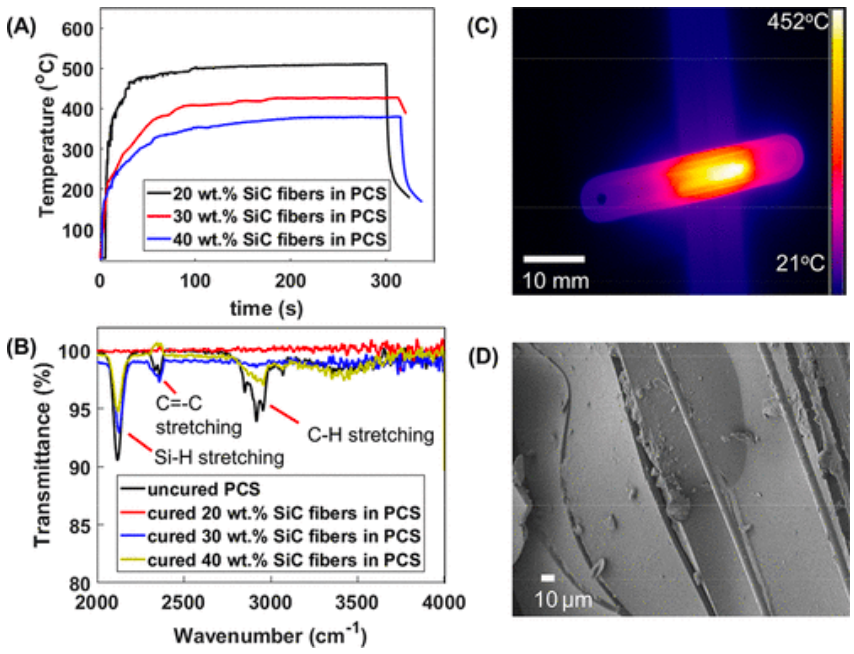

Figure 1.2: (A) Temperature vs time response for varying wt.% of Hi-Nicalon fibers in polycarbosilane (PCS) aligned parallel to the field. (B) FTIR spectrum showing extent of curing of polycarbosilanes (PCS): 20 wt.% fibers in polycarbosilane cured completely. (C) FLIR image showing heating of fiber on fringing field applicator. (D) SEM image of resulting composite for 20 wt.% Silicon Carbide (SiC) fibers in PCS [20].

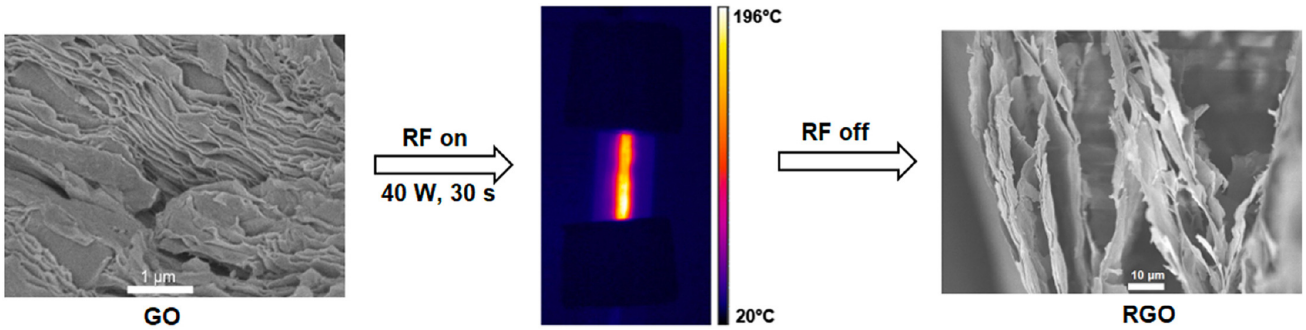

Figure 1.3: When graphene oxide (GO) is exposed to RF waves, the GO samples are reduced by the RF treatment. RF waves resistively heat GO with electric fields in seconds to form reduced GO.

Carbon nanotubes (CNTs) show excellent RF response; they heat up rapidly and reach high temperatures easily [17]. When carbon nanotubes (CNTs) are dispersed in a thermosetting epoxy matrix, the CNTs make the resin RF responsive, thus, allowing rapid, out-of-oven heating and curing of thermosets when exposed to a patterned RF field. Due to the rapid and uniform volumetric heating and curing, RF heating helps prevent aggregation or dispersion issues as well.

In this thesis, we first study the rheological properties and curing kinetics of a CNT-filled thermosetting polymer and demonstrate two new techniques to print multi-layered structures using localized RF heating and curing.

Chapter 2: Kinetics of carbon nanotube-loaded epoxy curing: rheometry, differential scanning calorimetry, and radio frequency heating

In this chapter, we study the reaction kinetics of bisphenol A diglycidyl ether and a trifunctional primary amine. We studied the isothermal curing of DGEBA-CNT resin using rheometry and Differential Scanning Calorimetry to understand the curing kinetics. We monitored *in situ* curing behavior of RF heated DGEBA-CNT resin using a rheometer and show that RF heating allows for rapid volumetric heating and curing of thermosetting resins.

2.1. Experimental methods

2.1.1. Materials

Bisphenol A diglycidyl ether (DGEBA or BADGE) epoxide was used in this study and purchased from Sigma Aldrich. A low viscosity curing agent, Jeffamine T403 polyetheramine was used as the hardener. The weight ratio of epoxide to curing agent was 100:49 (epoxide: curing agent). 5 wt.% of non-functionalized multi-walled carbon nanotubes (MWCNTs) from Cheaptubes were added to the mixture. The matrix was mixed in a planetary mixture for 10 minutes and degassed in a vacuum oven for 10 minutes to ensure uniform dispersion.

2.1.2. RF heating and rheological measurements

A stationary, fringing field applicator fabricated by laser-etching copper traces on FR4 substrate was used for this experiment. The copper traces acting as capacitors had a spacing of 4 mm, resulting in a fringing field coming out-of-plane of the applicator. The RF waves were generated using a RIGOL DSG815 signal generator, which were then amplified using a PRANA GN 500 amplifier and supplied to the applicator via a coaxial cable. RF heating setup is shown in **Figure 2.1** [17, 21, 23]. A glass slide with 3 mL of the epoxy-CNT matrix was placed on the RF

applicator, and a frequency of 132 MHz was used. The power was modulated manually to hit the desired target temperature. The RF heated sample was immediately transferred to a pre-heated rheometer to measure rheological properties. After loading the sample in the rheometer, a waiting time of 2 minutes was observed to ensure the RF heated sample had reached the specified isothermal measurement temperature. The initial average values of storage modulus (G'), loss modulus (G''), and complex viscosity were recorded to avoid curing of RF heated samples in the rheometer.

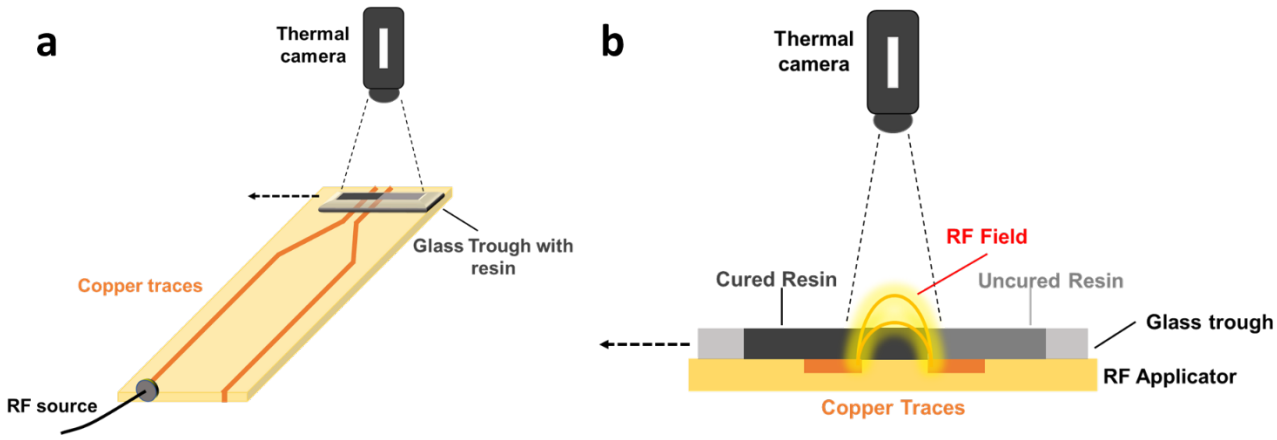

Figure 2.1: (a) Schematic showing out-of-oven RF-assisted curing and printing in resin bath. The RF applicator is moved relative to the resin at a constant speed using a linear stage to print a continuous sample, (b) Cross-section view shows the fringing field heating the filled resin and allowing the sample to cure.

2.2. Results and discussion

2.2.1. Rheo-kinetic analysis

Oscillatory time sweep tests were performed on the epoxy-CNT mixture under isothermal conditions [24]. The results are shown in **Figure 2.2 and 2.3.** During the curing process, time-dependent rheological changes of thermosets were analyzed using rheo-kinetics. G' variation with time can be used to calculate the degree of cure because G' is generally proportional to the density of the network formed by crosslinking. For rheo-kinetics of the isothermal curing reaction, the degree of cure (α) is defined using the following **Equation 2.1** [25]:

$$\alpha = \frac{G'(t) - G'(t=0)}{G'(t=\infty) - G'(t=0)} \qquad (2.1)$$

Here, G'(t = 0) and G'(t) are the moduli at the beginning and at time t of the curing reaction respectively. G'(t = ∞) is the value of the dynamic modulus at the end of the curing process. For the epoxy-CNT mixture, the degree of cure values were calculated using **Equation 2.1**, and were plotted against curing time in **Figure 2.4** based on rheological results obtained from oscillatory time sweep tests. At each of the four temperatures, the degree of cure approaches a unit value after a specified curing time. The curing time decreases as the curing temperature increases. These changes are dependent on the viscosity changes over the curing time. The general expression suggested by the Kamal-Sourour model, **Equation 2.2**, has been used to describe the curing rheo-kinetics of thermosets.

$$\frac{d\alpha}{dt} = (k\alpha^m)(1-\alpha)^n \qquad (2.2)$$

Here, dα/dt is the curing rate from the rheology measurements, *k* is the temperature dependent rate constant, and *m* and *n* are empirical reaction constants that reflect reaction orders and

define the initiation and propagation stages of curing, respectively. This model is a widely used model that includes the autocatalytic effects that result in the crosslinking network during the curing process.

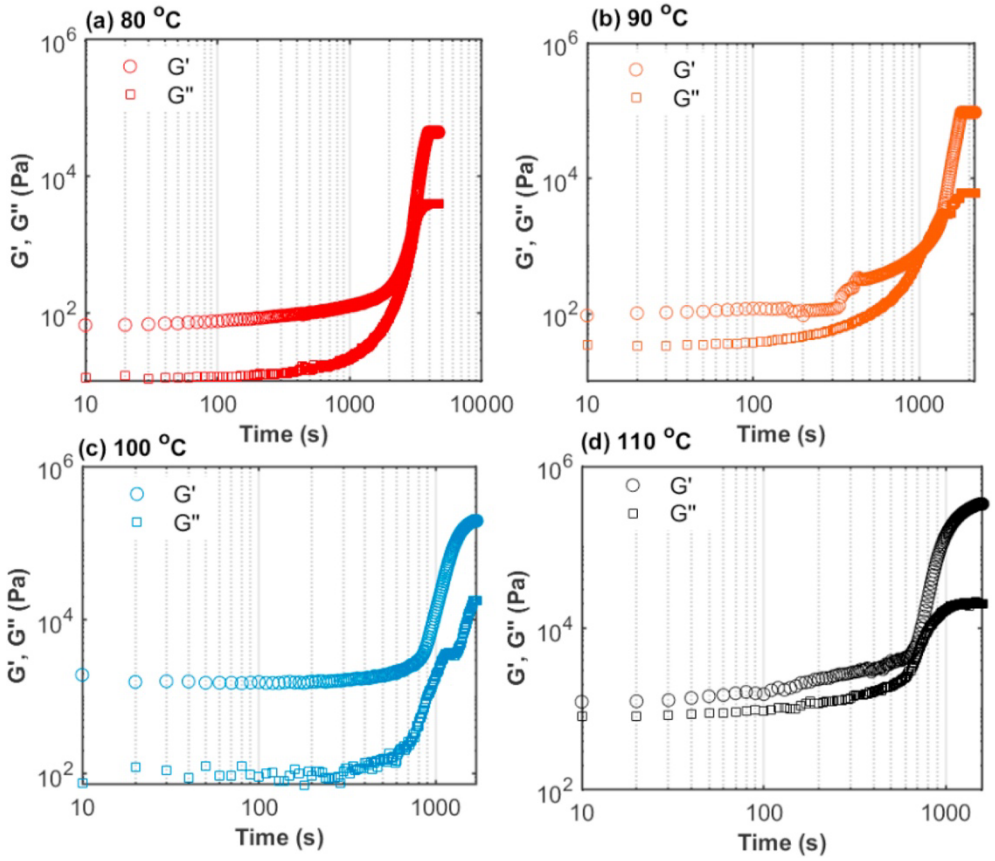

Figure 2.2: The variation of G′ and G″ moduli with curing time at different temperatures at (a) 80 °C, (b) 90 °C, (c) 100 °C, (d) 110 °C.

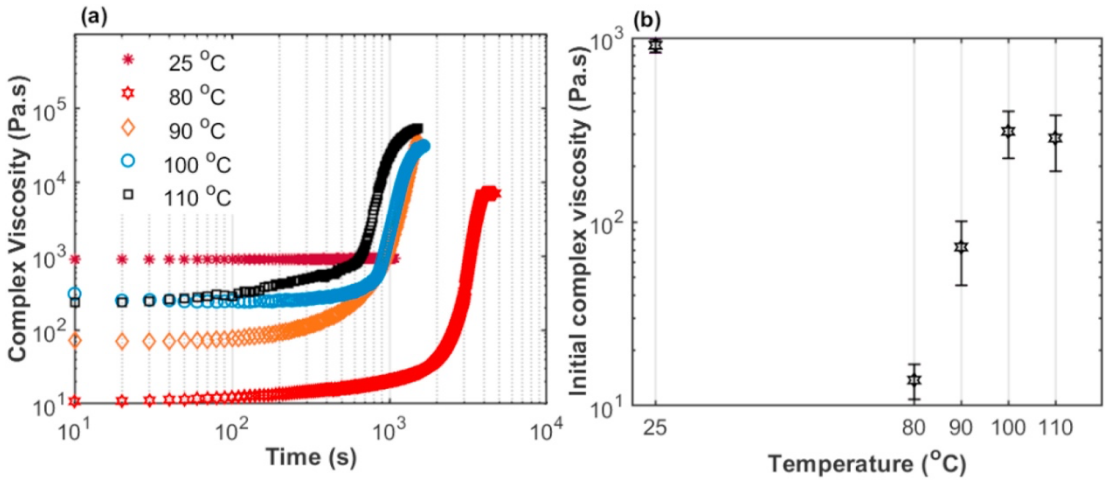

Figure 2.3: (a) The variation of complex viscosity with curing time at different temperatures and (b) Initial complex viscosity values at t = 10 s measured at different temperatures.

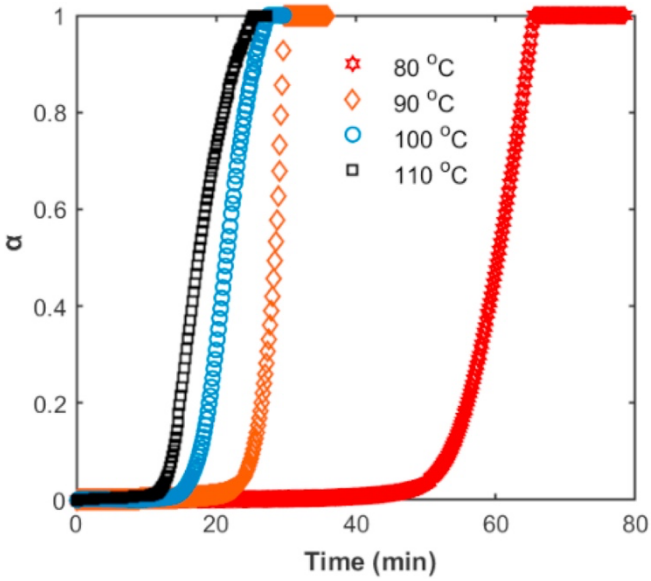

Figure 2.4: Variation of degree of cure, a with curing time at different curing temperatures. Computed from Figure 3.2 data using equation (2.2).

The rate of curing reaction is plotted in **Figure 2.5** as a function of degree of cure for 80, 90, 100, 110 °C. Here, the symbols show the data from rheological measurements and the solid curves show fitting results from the Kamal-Sourour model. For low values of alpha, there are many data points that correspond to the initial kinetic period (t < 40 min, t < 20 min, t< 18 min, and t < 15 min for 80, 90, 100, 110 °C respectively). The curing rate approaches a maximum at alpha values of approximately 0.7, 0.6, 0.5, and 0.4 for 80, 90, 100, 110 °C respectively, as shown in **Figure 2.5**. These results demonstrate that the curing rate increases with an increase in the curing temperature. Additionally, the maximum curing rate ($d\alpha/dt$) is achieved at lower alpha values as the curing temperature increases. As the alpha value increases, the curing rate gradually decreases due to increasing viscosity of the epoxy-CNT sample until it reaches a cured state. The increase in viscosity causes a decrease in mobility of the reactants, which decreases the rate of reaction ($d\alpha/dt$) until it ultimately approaches zero.

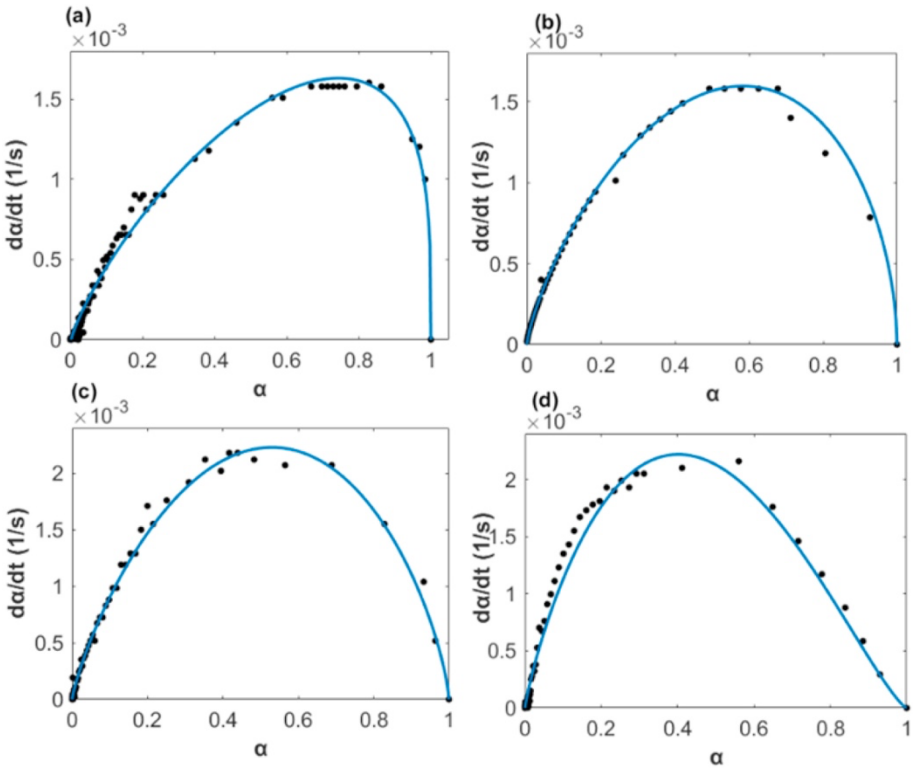

Figure 2.5: Curing rate, da/dt versus degree of cure, a, of Epoxy- CNT sample at different temperatures (a) 80 ˚C, (b) 90 ˚C, (c)100 ˚C, (d) 110 ˚C in rheometer. The solid curves are fitting results from model equation, and the symbols are experimental data.

For a specific isothermal temperature, Kamal-Sourour model parameters *k*, *m* and *n* calculated are listed in **Table 2.1**. A reasonable fit was achieved for all four temperatures with R^2 values of > 0.980. The reaction rate constant (*k*) values increase with increasing curing temperature due to an increase in reactivity. The *m* values represent the autocatalytic effect of the initiation step of curing and show little decrease with increasing curing temperatures. The *n* values signify the propagation step of curing; these values increase with increase in curing temperatures. After the

maximum curing rate is achieved, the crosslinked molecules participate in the curing reaction, forming a more viscous network. For lower *n* values, at the propagation step of curing, the propagation reaction progresses quicker, indicating that the curing rate, $d\alpha/dt$, decreases rapidly with an increase in alpha values as seen in **Figure 2.5 (a)** compared to **Figure 2.5 (b-d)**. Lastly, the overall reaction order, (*m + n*), also increases (1.3-1.6) with an increase in the curing temperature.

T(°C)	k (s^{-1})	m	n	R^2
80	0.00307	0.855	0.424	0.982
90	0.00404	0.838	0.568	0.998
100	0.00595	0.802	0.633	0.993
110	0.00783	0.801	0.823	0.986

Table 2.1: Kamal-Sourour model kinetic parameters at different isothermal curing temperatures.

The activation energy for the curing reaction of the epoxy-CNT system was calculated using the Arrhenius equation (**Equation 2.3**). Here, *k* is the reaction rate constant, E_a is the activation energy, *T* is the absolute temperature of the curing reaction, and *R* is the universal gas constant.

$$k = Ae^{-\frac{E_a}{RT}} \qquad (2.3)$$

The activation energy of the curing reaction was approximately 36 kJ/mol using the values of k(T) calculated in **Table 2.1**. The Arrhenius plot used for the calculation is shown in **Figure 2.6 (a)**.

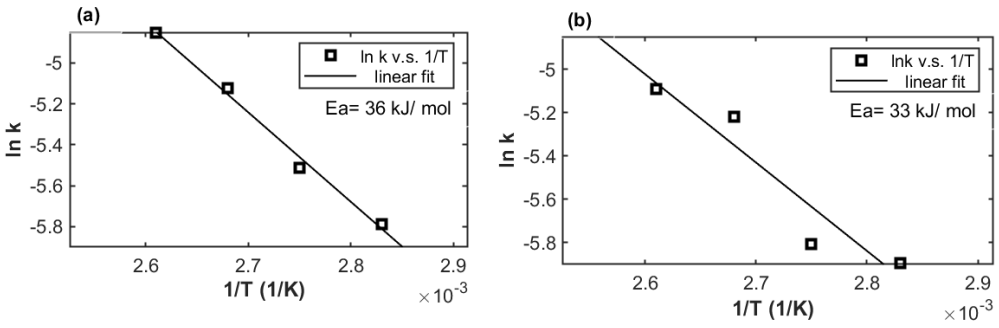

Figure 2.6: Arrhenius plot of epoxy-CNT system using (a) Rheometer and (b) DSC measurements. Reaction rate constants, (k values) listed in Tables 2.1 and 2.2 are plotted as functions of temperature.

In literature, the value of activation energy ranges from 20-60 kJ/mol for epoxy-amine reactions. Cai et al. [26] studied isothermal curing of DGEBA epoxy and T403 curing agent system at 70-90 °C and they found the activation energy to be 50 kJ/mol using DSC. McCoy et al. [27] also calculated an activation energy of 57.7 kJ/mol for isothermal curing at 50-110 °C for the same system using DSC. Previous studies have shown that the addition of CNT in epoxy mediums decreased the activation energy of the curing reaction in comparison to activation energies of neat resins [28-30]. A similar trend can be expected for our epoxy-CNT system as well. Theoretical calculations have found that the activation energy for epoxide and amines curing reactions to be within the range of 35.8-44.3 kcal/mol [31, 32]. Hence, our E_a value seems reasonable, and rheometer curing is a valuable method for investigating cure kinetics of epoxy-CNT systems.

2.2.2. Curing kinetics analysis using Differential Scanning Calorimetry

Differential scanning calorimetry was performed on the epoxy-CNT mixture to monitor the curing reaction and to provide supporting data for rheological analysis[24]. In these

experiments, the exothermic heat released by the curing reaction is used to observe the transition from a viscous state to a solid state through crosslinking. Here, the degree of cure, α, is directly related to the change of heat flow with curing time during the curing process, as shown by **Equations 2.4-2.5** below [33]:

$$\frac{dH}{dt} = \frac{d\alpha}{dt} \qquad (2.4)$$

$$\alpha = \frac{H_t}{H_{total}} = \frac{1}{H_{total}} \int_0^t \frac{dH}{dt} dt \qquad (2.5)$$

Here, α is the degree of cure, H_t is the total heat flow for time t, and H_{total} is the total heat released for the curing process assuming a complete reaction. Isothermal curing heat flow curves of the present system at 80, 90, 100 and 110 °C are depicted in **Figure 2.7** showing an exothermic peak for each temperature. The calculated area under the heat flow peak for each temperature is the H_{total} for the curing process. H_{total} values were calculated using integration of the curve function to be 1.53 W/g, 2.09 W/g, 2.39 W/g, and 2.60 W/g for temperatures 80, 90, 100, and 110 °C, respectively. The degree of cure, α, was calculated using DSC results shown in **Figure 2.7** and **Equation 2.5**. The change in degree of cure over time at each of the four temperatures is plotted in **Figure 2.8**. The behavior of alpha changing with time looks different compared to rheological degree of cure changing with curing time. In **Figure 2.8**, the degree of cure increases rapidly during the initial reaction stage and ultimately approaches a cured state as curing time increases, whereas an S-shaped curve can be observed in **Figure 2.4**. This difference exists because there is no initial curing period present in the DSC experiment compared to rheometer measurements. Additionally, the beginning of the formation of crosslinking networks occurs in a shorter time compared to the curing time observed in a rheometer. In DSC measurements, the curing time is defined by the total heat evolution during the experiment. Therefore, 80 and 90 °C

have approximately similar curing times due to having similar H_{total} values during the cure compared to those observed for 100 and 110 °C.

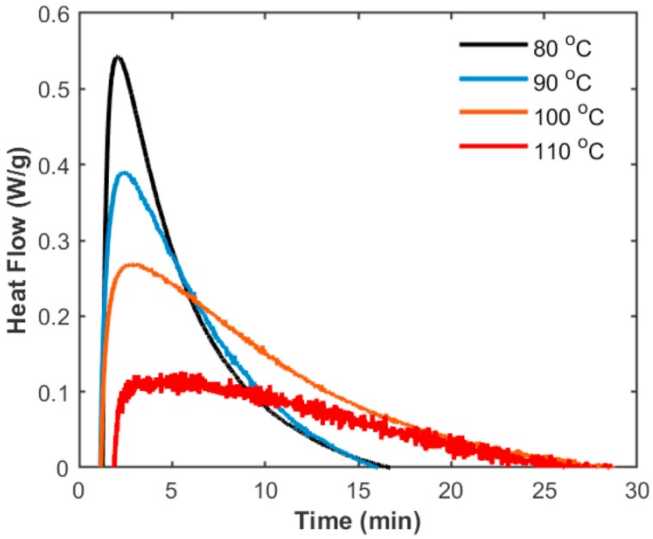

Figure 2.7: Differential scanning calorimetry heat flow curve of epoxy-5%CNT for isothermal curing at 80 °C, 90 °C, 100 °C, 110 °C.

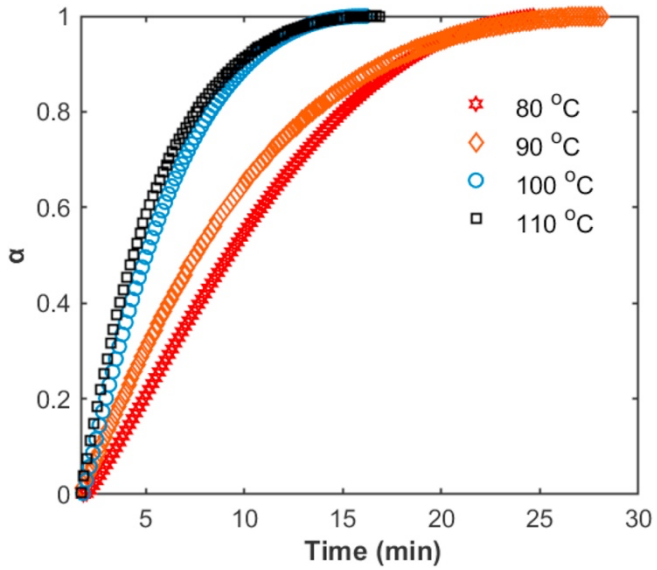

Figure 2.8: Variation of degree of cure, a with curing time at different curing temperatures using DSC. Computed from Figure 3.7 data using equation (2.5).

Plots of curing rates, $d\alpha/dt$, versus the degrees of cure (α) of the epoxy-CNT sample at different temperatures are shown in **Figure 2.9**. Here, the symbols represent the data obtained from DSC measurements and the solid curves represent the curve-fitting results from the Kamal-Sourour model. The maximum curing rate increases with the curing temperature, as expected. At the maximum curing rate, the degree of cure is 0.2 for all curing temperatures. This peak alpha value for DSC results is lower than peak alpha values observed for rheology results. This observed trend implies that the molecular mobility through the cross-linking network is low during the earlier stages of curing due to a higher viscous medium. At later stages, the rate of curing reaction, $d\alpha/dt$, decreases until the curing reaction terminates due to molecular immobilization of the crosslinked networks.

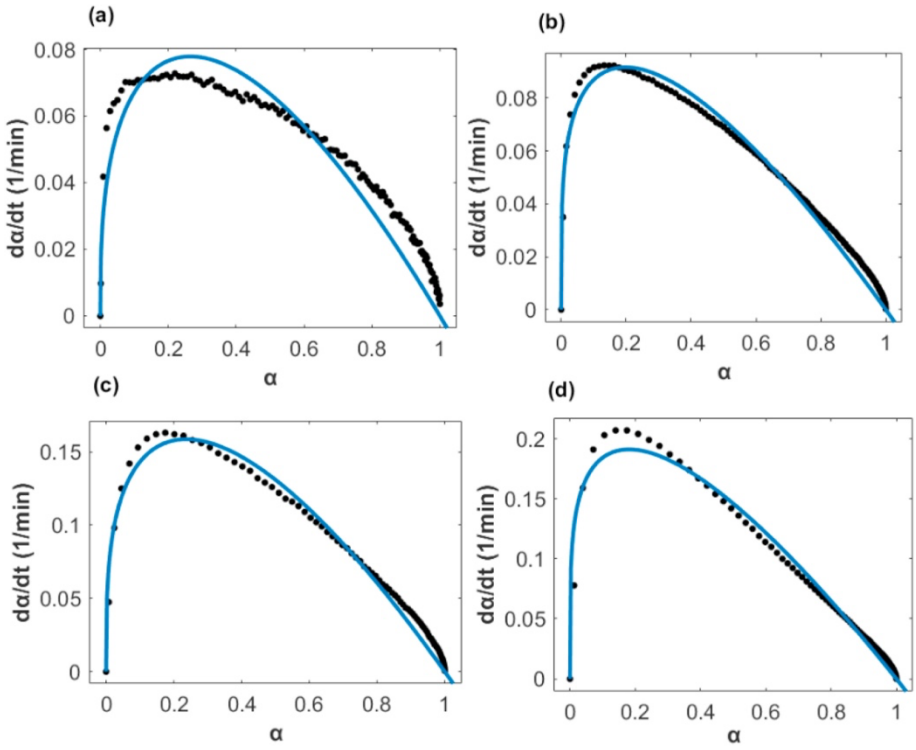

Figure 2.9: Curing rate, da/dt, versus degree of cure, a, of epoxy-CNT sample at different temperatures (a) 80 °C, (b) 90 °C, (c) 100 °C, (d) 110 °C in DSC. The solid curves are fitting results from model equation, and the symbols are experimental data.

For each temperature, Kamal-Sourour model parameters *k*, *m* and *n* calculated are listed in **Table 2.2**. A reasonable fit was achieved for all four temperatures with R^2 values of ≥ 0.9 for each temperature. The parameters for 80, 90, and 100 °C are similar to parameters calculated using rheological results. At 110 °C, the reaction rate constant value (*k*) differs significantly from the rheo-kinetics value. This discrepancy can be attributed to the interaction between chemical (curing reaction) and viscosity changes of the samples during the curing process in a rheometer, whereas the viscosity changes are not as prominent in DSC measurements; DSC measurements

are primarily governed by the heat released during the curing reaction. The activation energy of the curing reaction was calculated using the Arrhenius equation to be approximately 33 kJ/mol, which agrees with the rheo- kinetics analysis.

T(°C)	k (s^{-1})	m	n	R^2
80	0.00276	0.352	1.0	0.899
90	0.00301	0.383	1.0	0.987
100	0.00542	0.402	1.0	0.980
110	0.00615	0.389	1.0	0.984

Table 2.2: Model kinetic parameters from DSC at different isothermal curing temperatures.

The kinetic model fitting constants, *m* and *n*, are nearly constant for all curing temperatures, unlike the rheological results. The *m* value here signifies the autocatalytic curing order related to the maximum crosslinking between the networks during the curing reaction. At maximum curing rate, alpha values approach ~0.2 for all curing temperatures. The *n* values measure the order of isothermal heat evolution rate from the expected decrease in curing rate with increased curing time. The larger *n* values (in comparison to rheological results) for the curing reaction supports the decrease in curing rate while approaching the propagation steps of the curing. Here, the overall reaction order (*m + n*) is approximately 1.4, and doesn't vary with curing temperature, as expected.

In prior work, there is a general lack of agreement about the values of *m* and *n*, as well as about their temperature dependence in the Kamal-Sourour model. In the work by Cai *et al.* [26] for isothermal curing of DGEBA epoxy and T403 system at 70-90 °C, both *m* and *n* values were found to be constant with varying temperature (*m* = 0.6 and *n* = 2.3); however, Li *et al.* [34] reported that *m* varied slightly with temperature and the average value calculated was *m* = 1.12, whereas *n* decreased with temperature approximately linearly with an average value of *n* = 1.02 for isothermal curing DGEBA-T403 system in the temperature range of 60-140 °C.

In summary, although E_a values obtained from rheometry and DSC data are close, the curing profiles and kinetic parameters calculated vary. Rheometry and DSC examine different aspects of curing; rheometry measures the mechanical aspect, whereas DSC measured the thermal aspect. In the Kamal-Sourour model (**Equation 2.2**), *m* values correspond to the autocatalytic reaction, while *n* values represent the propagation reaction. In rheometry, the autocatalytic growth and branching of the crosslinking networks are measurable at a higher degree of curing, resulting in a more viscous reactive system as compared to a DSC measurement. This leads to a more pronounced autocatalytic curing effect, leading to a larger *m* value for rheological measurements compared to DSC measurements.

In contrast, the maximum curing rate is measurable earlier in the process in DSC measurements; the crosslinking process leads to high molecular weight of the system, which significantly increases the viscosity. This restricts motion of crosslinked molecules, resulting in high *n* values for DSC measurements compared to rheological measurements. Conversely, for rheological measurements, *n* values increase with temperature due to the increased restriction in crosslinked molecular motion. Furthermore, *n* values remain constant across different

temperatures in DSC measurements because the increase in viscosity has a lesser impact on the measurements in determining the overall reaction rate. Thus, even though *m* and *n* values vary for rheometry and DSC measurements, the overall order (*m + n*) matches closely because the autocatalytic and propagation reactions contribute differently to the two different measurements.

2.2.3. RF curing experiments

An RF electromagnetic field is used to heat the CNT filler and cure the thermosetting resin. RF heating provides rapid and uniform volumetric heating and curing of nano-filled resins. This curing method is useful as it eliminates thermal gradients during 3D printing of thermosets [19]. Here, we used rheology to probe the degree of cure after a given time-and-temperature in the RF curing setup.

The epoxy-CNT samples were heated using a fringing field RF applicator, and the desired temperature was maintained by manually modulating the power. The RF heated samples, at different time steps, were quickly transferred to a pre-heated rheometer to measure the G', G", and complex viscosity values until complete curing was observed. Note that there was a small lag (2 min) between the sample transfer and the beginning of the measurements. Thermal images of the CNT loaded epoxy heated using RF field at different target temperatures (90, 100, 110, and 120 °C) are shown in **Figure 2.10**. Volumetric curing behavior of RF heated epoxy-CNT samples was investigated by tracing changes in G', G" and complex viscosity values.

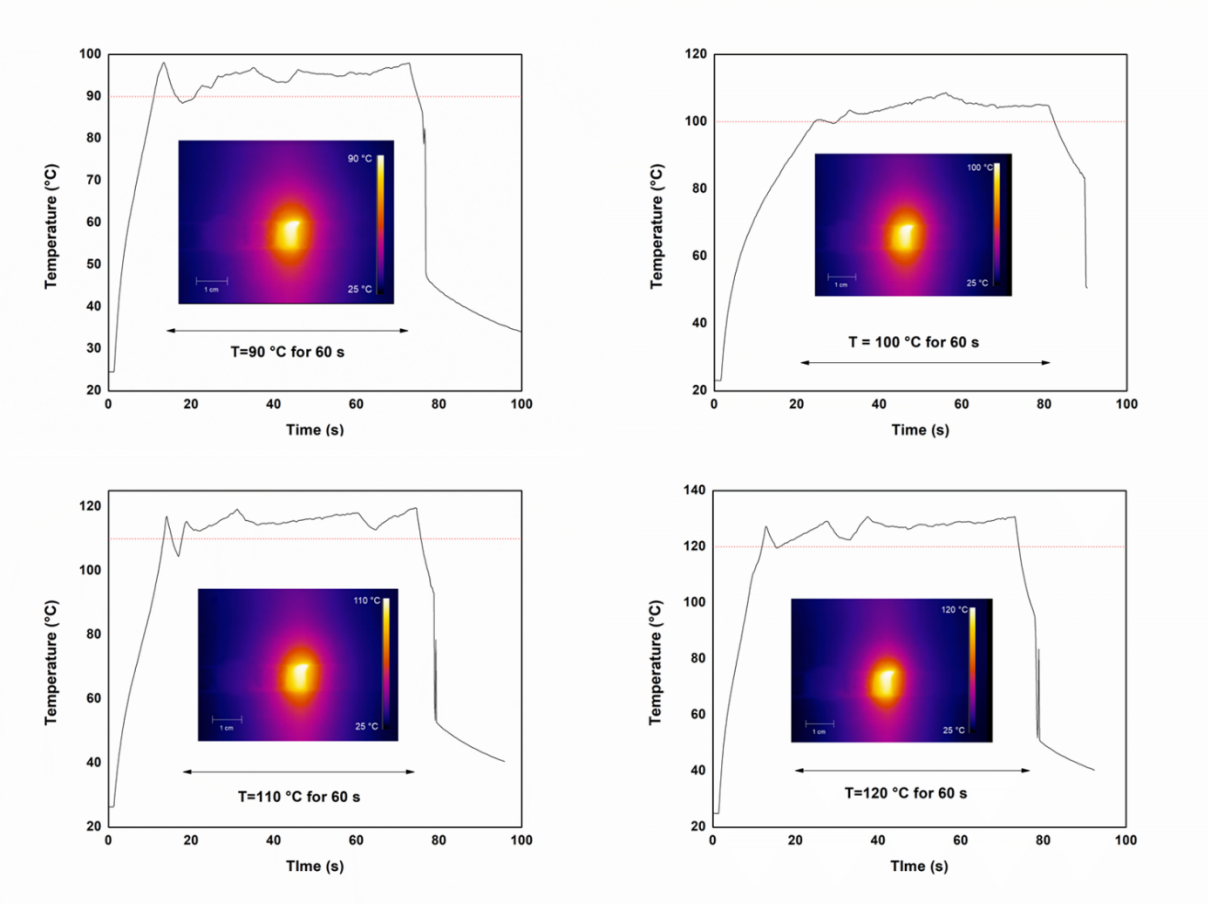

Figure 2.10: Temperature vs. time plot of CNT-loaded epoxy heated using Radio Frequency field and maintained at target temperatures (a) 90 ^{o}C (b)100 ^{o}C, (c)110 ^{o}C (d) 120 ^{o}C for 1 minute. Thermal images captured after reaching target temperatures using FLIR camera.

Here, G' and G" variations as a function of RF exposure time at 90, 100, 110, and 120 °C are shown in **Figure 2.11**. It can be observed through these results that as the samples starts heating from time t = 0 at 25 °C, the G', G" and complex viscosity values initially drop as seen in **Figure 2.11 (a-b) and Figure 2.12**. In the beginning of the curing stage, viscous forces dominate the sample, resulting in decreased viscosity; this trend is also observed in our previous rheometry

results without RF curing. After 1 minute, the resin starts curing up to t = 7 min (at 90 °C) and t = 5 min (at 100 °C). After 3 minutes at 100 °C, the G' value and the G" value are approximately equal due to the formation of crosslinking network (chemical gelling). This gelling occurs at time t = 15 minutes during rheometer curing without RF heating (**Figure 2.2 (c)**). This demonstrated that RF heating results in a significantly shorter time required for curing due to rapid volumetric heating compared to external heating and curing. We also observe that the changes in G' and G" values are much smaller in the baseline samples (without RF heating) compared to RF heated samples (**Table 2.3**). This shows that the 2-minute lag time on the rheometer measurements after RF heating do not disrupt the G' and G" measurements.

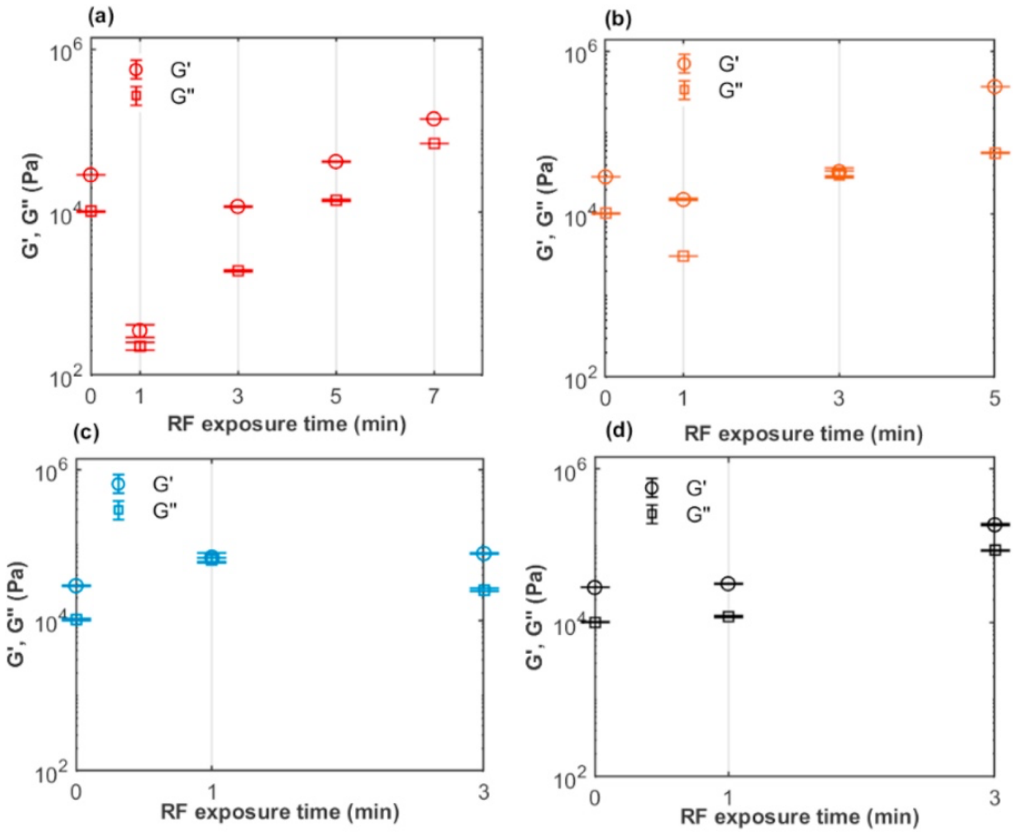

Figure 2.11: G′ and G″ variations with RF exposure times at different temperatures (a) 90 ˚C, (b) 100 ˚C, (c) 110 ˚C, (d) 120 ˚C. At t = 0, RF time (min) axis shows the value of G′, G″ of epoxy-CNT at 25 ˚C. RF heated sample is loaded rapidly in a pre-heated rheometer; G′, G″ values are reported from the starting point of rheological measurements.

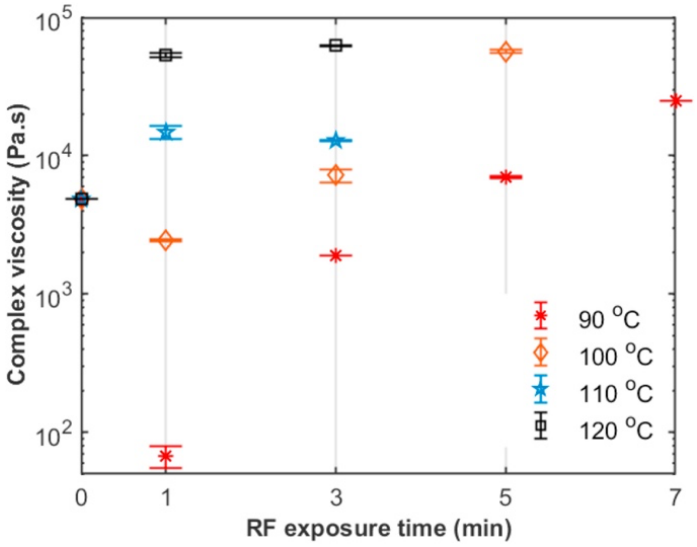

Figure 2.12: Complex viscosity variations with RF heating times at different temperatures. At t = 0 on RF time (min) axis shows the value of complex viscosity value of epoxy-CNT at 25 °C. RF heated sample is loaded rapidly in a pre-heated rheometer; complex viscosity values are reported from the starting measurement points of rheological measurements.

As the curing temperature increase, G' and G" change faster as shown in **Figure 2.11 (c-d)**. At 110 °C, G' and G" values approach a similar value after only 1 minute; this means that the sample undergoes a drastic viscoelastic structural change, thereby solidifying the sample. At 3 minutes, the sample reaches a completely cured state at 110 and 120 °C. During baseline rheology experiments at 110 °C (without RF heating), the crosslinking network formation (G' ~ G") occurs at approximately 10 minutes (**Figure 2.2 (d)**). For 120 °C, the sample is completely cured in 3 minutes with G' > G" values. The viscosity increases significantly with intermolecular crosslinking at high curing temperatures in **Figure 2.12**, and at 110 and 120 °C, the viscosity values

are approximately constant after 3 minutes as the sample is completely cured. Similar final viscosity values (~10^4) are observed with and without RF heating of the sample as shown in **Figure 2.3**.

T(°C)	RF heating time (min)	G' (Pa)	G"(Pa)	Without RF heating (min)	G' (Pa)	G"(Pa)
90	0	1.02e+2	3.47e+1	0	1.02e+2	3.47e+1
	1	3.07e+2	2.01e+2	1	1.11e+2	3.54e+1
	3	1.17e+4	1.97e+3	3	1.18e+2	4.54e+1
	5	4.14e+4	1.42e+4	5	1.20e+2	5.87e+1
	7	1.40e+5	7.02e+4	7	3.40e+2	7.80e+1
100	0	1.23e+3	9.41e+1	0	1.23e+3	9.41e+1
	1	1.49e+4	3.09e+3	1	1.53e+3	10.1e+1
	3	3.06e+4	2.87e+4	3	1.56e+3	10.4e+1
	5	3.66e+5	5.77e+4	5	1.64e+3	10.7e+1
110	0	1.91e+3	8.14e+2	0	1.91e+3	8.14e+2
	1	6.25e+4	5.92e+4	1	1.94e+3	8.94e+2
	3	7.61e+4	2.61e+4	3	2.18e+3	1.23e+3

Table 2.3: Comparison of G' and G'' values for RF heating and without RF heating.

2.3. Conclusion

In this study, isothermal curing of epoxy-CNT system was characterized using rheo-kinetics and DSC. The Kamal-Sourour model was used to describe the rheo-kinetic behavior of the system, and this model was verified through DSC measurements performed at the same isothermal temperatures. Similar values for curing reaction rate constants and activation energies were obtained from rheology and DSC; however, the curing profile and curing time of epoxy-CNT samples differed due to different basis of curing degree calculations. We also used rheology to analyze RF-heated epoxy-CNT samples by monitoring the changes of G', G'', and complex viscosity after specified RF exposure times. These measurements confirm that RF exposure allows for rapid, volumetric heating and curing that are significantly faster than conventional techniques. Rheological findings and kinetic modeling of these nano-filled epoxy systems will enable predictive design for 3D printing of thermosetting polymers using RF or other out-of-oven, volumetric heating methods.

Chapter 3: Rapid manufacturing via selective Radio Frequency heating and curing of thermosetting resins

In this study, we demonstrate a new technique to print multi-layered structures using localized RF heating and curing[35]. We printed multi-layered structures by moving the RF applicator relative to the resin reservoir, selectively curing the resin exposed to the field; this process was repeated for each layer. For comparison against conventional curing methods, we performed thermal and mechanical characterization of RF printed samples and conventional (oven-cured) samples; both samples show similar glass transition temperatures and storage moduli, and the RF-heated samples show a more uniform morphology with fewer voids. Thus, demonstrating that RF heating is a faster, and more energy efficient method for curing thermosetting resins which can be used to print structures with comparable thermal and mechanical properties to conventionally cured samples. We also model the spatiotemporal kinetics of a resin reservoir being exposed to a moving heat source to create 3D structures and to show the scope of this method in printing complex structures.

3.1. Experimental methods

3.1.1. Materials

The epoxide used in this study was Bisphenol A diglycidyl ether (DGEBA), purchased from Sigma Aldrich, which is a bi-functional thermosetting epoxide with numerous commercial applications. A low viscosity curing agent purchased from Huntsman Corp, Jeffamine T403 polyetheramine, was used as the hardener. 5 wt.% ratio of multiwalled carbon nanotubes (MWCNTs) from Cheaptubes were added to this matrix (5 wt.% was optimized to get desirable

RF heating response). To ensure uniform dispersion of MWCNTs, the sample was mixed in a planetary mixer for 10 minutes and degassed in a vacuum oven for 30 minutes.

3.1.2. Radio Frequency setup

A stationary, fringing field applicator fabricated by laser-etching copper traces on FR4 substrate was used for this experiment. The copper traces acting as capacitors had a spacing of 4 mm, resulting in a fringing field coming out-of-plane of the applicator. The RF waves were generated using a RIGOL DSG815 signal generator, which were then amplified using a PRANA GN 500 amplifier and supplied to the applicator via a coaxial cable. A linear stage, and an x-y stage were used for continuous linear and 2D experiments. The stages were programmed to move the RF applicator relative to the resin at a constant speed calculated using the residence time required to completely cure each spot of epoxy.

3.1.3. Selective heating and curing experiments

A stationary sample of CNT-filled resin was placed on an RF applicator and heated to determine the target temperature and exposure time required to cure the sample completely **(Figure 2.1 (a)**).

For printing one dimensional extended parts, a glass reservoir of dimensions 34 mm x 5 mm was filled with RF responsive resin. A linear stage was used to move the RF applicator relative to the resin reservoir at a constant speed of 0.067 mm/sec **(Figure 2.1 (b))**. The RF power was modulated to maintain the target temperature of the resin at ~250 °C. Two additional samples of similar composition were prepared and cured using the following methods for comparison against RF cured samples: (1) the second sample was RF cured, followed by a post-cure step in a

conventional oven at 250 °C for 2 minutes, and (2) the third sample was cured in a conventional oven 250 °C for 5 minutes.

For printing a two-dimensional ring, the RF applicator was moved relative to the resin reservoir in a circular motion using an x-y stage. The tangential speed of the circular motion was constant at 0.067 mm/sec. The selectively cured structure was extracted from the uncured resin and washed with acetone.

3.1.4. Characterization

Thermo-gravimetric Analysis. Thermo-gravimetric Analysis (TGA) measurements were performed using TA instruments TGA 5500 to determine the degradation temperature of the samples. For the measurements, each sample was loaded on a platinum pan and the temperature was ramped at the rate of 10 °C/min from 25 °C to 500 °C.

Differential Scanning Calorimetry measurements were performed using TA instruments Q-20 to determine the glass transition temperature of the samples. Heat flow was observed at a rate of 3 °C/min against change in temperature from 25 °C to 250 °C.

Dynamic Mechanical Analysis. Dynamic Mechanical Analysis (DMA) was performed using TA Instruments DMA 850 to examine the thermo-mechanical properties of samples. A 17.5 mm single cantilever test was performed with a temperature ramp from 35 °C to 120 °C, at a rate of 3 °C/min. The frequency and strain were set to 1 Hz and 0.04 % respectively for all tests. Here, the damping coefficient (tan δ) is defined as the ratio of loss and storage modulus (E’’/E’).

Scanning Electron Microscopy. Scanning Electron Microscopy was performed using a FEI Quanta 600 FE-SEM to observe the cross-sections of samples.

Mechanical Testing. Tensile testing was performed using an Instron load frame with a 30 kN load cell on samples of dimensions 36 mm x 10 mm x 1.5 mm. Here, the displacement rate was set to 2 mm/minute.

Ultraviolet-visible spectroscopy. UV-vis spectroscopy was performed using a Shimadzu UV-vis 2500 to observe the dispersion stability of the CNT-filled resin sample. The wavelength was varied from 300 to 800 nm. The absorbance readings were recorded immediately after preparing the sample, and 30 minutes after preparing the sample.

3.1.5. Simulation

The model described below was discretized using the finite difference method and solved using a built-in implicit solver (with a mass matrix) in MATLAB R2020b.

The spatiotemporal kinetics are described by two ordinary differential equations. The modified Kamal-Sourour equation[36] was used to model the reaction kinetics (**Equation 3.1**).

$$\frac{dX}{dt} = (kX^m)(1-X)^n \qquad (3.1)$$

Here, *dX/dt* is the curing rate, *X* is the degree of cure, *k* is the temperature-dependent reaction rate constant, and *m* and *n* are empirical reaction constants that reflect reaction orders and define the initiation and propagation stages of curing, respectively. The parameters in **Equation 3.1** (*k*, *m*, and *n*), were determined in our prior using DSC experiments in the temperature range of 80-110 °C [24]. The data collected from these experiments was fitted to the modified Kamal-Sourour equation, and the activation energy was calculated to be ~33 kJ/mol using the Arrhenius equation. The calculated activation energy was used in the model to compute *k* as a function of local temperature. Because the DSC experiments were conducted at higher temperatures, the

parameters tend to overestimate the curing rate at low temperatures; to correct for this factor, the reaction constant is set to zero for temperatures under 50 °C.

The energy balance for the model is as follows:

$$\frac{dT}{dt} = \alpha\nabla^2 T + Q_{ext} + \frac{\Delta H_{rxn}}{C_p} + Q_{RF}(x,y,z) \qquad (3.2)$$

Here, *dT/dt* is the rate of change in temperature, the $\nabla^2 T$ term indicates heat conduction within the resin reservoir. and the ΔH_{rxn} term accounts for the heat generated by the exothermic curing reaction. Note that the curing reaction is exothermic, which means that the reaction can begin to drive itself, even into undesired areas of the matrix. Material functions like the thermal diffusivity (α) and the heat capacity (C_p) are matched to the epoxy resin itself. The sides of the vessel are considered to be insulated.

If the model is applied to only a single printed line (x) or plane (xy) of resin, then the thermal transport in the z direction is described by the Q_{ext} term, which includes the heat losses to surroundings through convection to the air above the sample and conduction to the underlying substrate (glass). These are written as:

$$Q_{ext} = \left[\frac{h}{\rho\, C_p h_{resin}}\,(T - T_{air})\right] + \left[\frac{\alpha_{substrate}\,(T - T_{substrate})}{{w_{substrate}}^2}\right] \qquad (3.3)$$

Here, h is the convection coefficient for air (~30 W/(m^2 K)), ρ is the density of the resin (900 kg/m^3), C_p is the heat capacity of the resin (~2000 J/(kg · K)), h_{resin} is the height of the resin in the reservoir (1 mm), T is the temperature at a node, T_{air} is the temperature of air in the room, $\alpha_{substrate}$ is the thermal diffusivity of the substrate (~7.47*10^{-7} m^2/s), $w_{substrate}$ is the thickness of the underlying substrate (1 mm), and $T_{substrate}$ is the temperature of the substrate. The temperature of the atmosphere and the underlying substrate were assumed to be 298 K.

For simulations where the heat source also moves in z to yield a 3-D printed structure, these Q_{ext} contributions are implemented in the upper, side, and lower boundary conditions. To mimic the experimental setup described in **Figure 3.1** below, the heat source in the simulation moves up in z-direction as a fresh layer of epoxy is added to the reservoir. This moving interface defines the upper boundary condition while the lower and side boundary conditions remain constant.

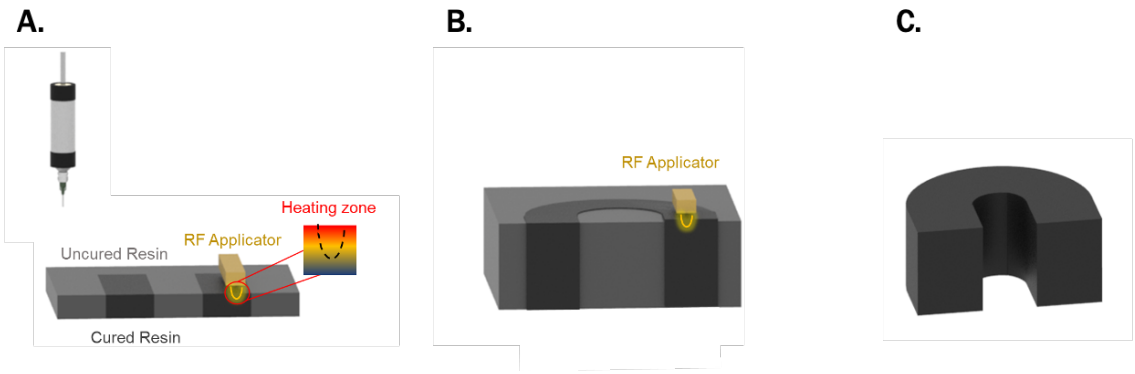

Figure 3.1: Schematic representing multi-layered additive manufacturing of thermosetting epoxy resin using radio-frequency assisted heating and curing. (A) Cross-sectional view of an RF applicator curing a structure in one layer of uncured resin; (B) Structure formed after repeated additions of uncured resin layers and selectively RF heating it to form a multi-layered structure; (C) Final cured structure extracted from a reservoir of uncured epoxy.

The Q_{RF} term indicates the volumetric heat source due to the RF field. We describe this field using a simple approximation: If a given location (x, y, z) is within range (2 mm) of the RF field source, then this term is turned on. Just as the RF power was modulated in the lab experiment to keep the maximum temperature of the resin in the range of 200-240 °C, the model similarly employs proportional control of Q_{RF} with a steady-state gain of 1 based on the maximum temperature of the resin reservoir.

3.2. Results and discussion

3.2.1. Printing Experiments

First, we measured the heating and curing behavior of the CNT-filled resin. Visual observation confirmed that at a relatively constant temperature of ~250 °C, the resin required 1 minute to cure completely in the RF field (**Figure 3.2**). The required exposure time of 1 minutes translates to the residence time of a sample being moved through an RF field. A target temperature of 250 °C was chosen because the curing kinetics model and experiments show that the resin cures completely within 1 minute at this temperature, thereby allowing us to maximize the print and cure speed[37].

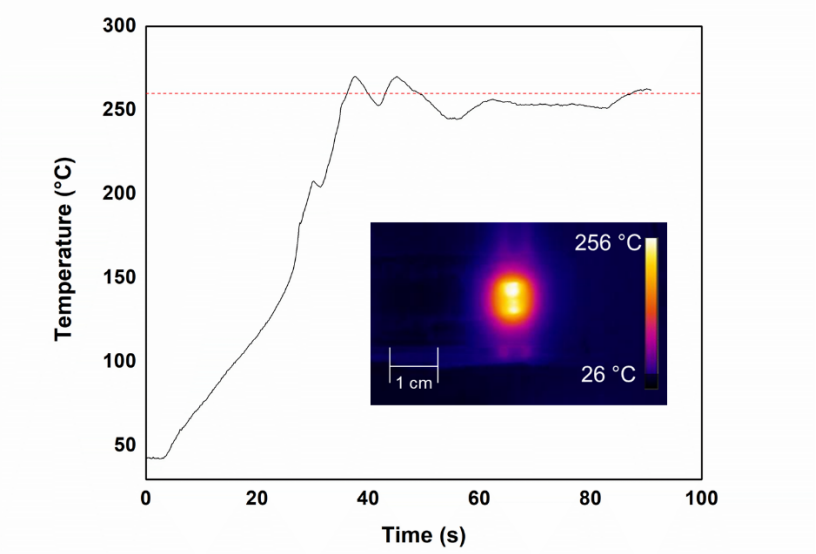

Figure 3.1: Maximum temperature vs. time plot for stationary RF heating of 5 wt.% CNT loaded epoxy resin. Power modulated to maintain T_{target} = 250 °C (marked in red). Inset: thermal image at steady state captured using FLIR camera.

Next, we cure an extended part using the movement of the applicator relative to the resin reservoir. The applicator speed was calculated by dividing the applicator length-scale of 4 mm (distance between the copper trace capacitors) by the residence time of 60 seconds. Thus, a scan speed of 0.067 mm/second was used. Note that this scan speed includes both printing and curing processes, and the described method does not require a post-curing step compared to traditional curing schedules which can be as long as 12-24 hours in an oven[38]. The resulting sample is a cured structure of dimensions 34 mm x 5 mm (**Figure 3.3 (a)**). We also demonstrate that this

technique can be used to cure two-dimensional shapes. Using an x-y stage, the applicator was moved relative to the resin in a circular trajectory, resulting in a cured ring shape (**Figure 3.3 (b)**).

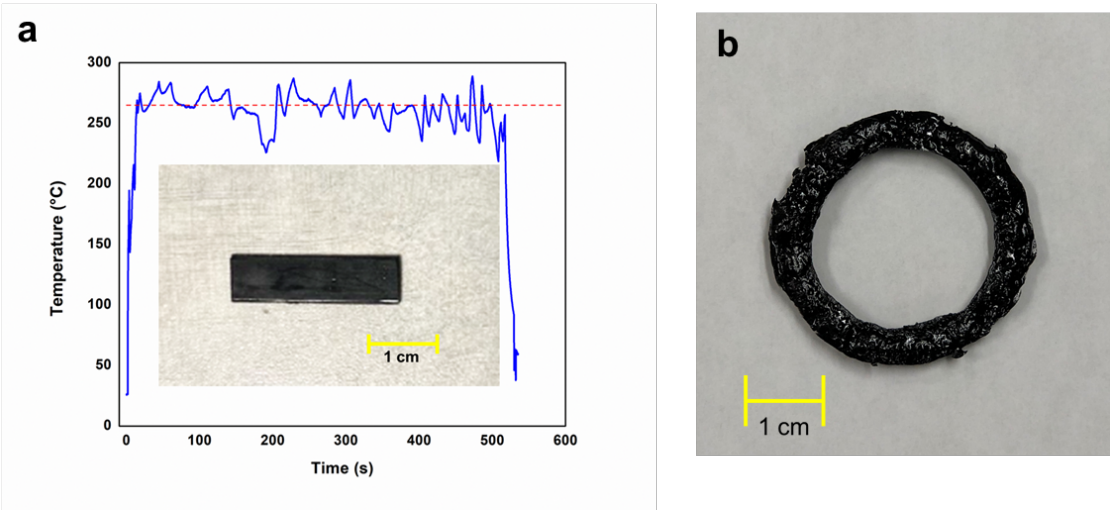

Figure 3.3: (a) Maximum temperature vs. time plot of 1D scan (0.067 mm/s) and print of 5 wt.% CNT loaded epoxy resin using RF heating. Inset: the printed 1D sample with dimensions of 34 mm x 5 mm, (b) 2D ring printed from a reservoir of epoxy using RF heating and curing. The RF applicator was moved relative to a resin reservoir using an x-y stage to induce localized heating and curing. Dimensions of printed structure: 15 mm inner radius, 20 mm outer radius.

The process used to print an extended part can be used repeatedly to build a multi-layered structure. After layer 1 was printed and cured, a layer of fresh epoxy was added to the reservoir up to the same thickness as the first layer and a second scan was done to selectively cure a section of the second layer, resulting in a multi-layer structure (**Figure 3.4 (a)**). This method addresses a problem for thermoset 3D printing – each layer is cured with sufficient inter-layer adhesion to allow the structure to support additional layers on top. Printing complex shapes requires the removal of the uncured material from the final printed part in addition to selective curing. The structure shown in (**Figure 3.4 (b)**) demonstrates that selective curing can be achieved by controlling the resin exposed to the electric field as only the resin exposed to the RF field will heat up and cure, leaving the rest uncured. The cured structure can be extracted easily from the reservoir, and the uncured material can be washed away with acetone. This demonstrates that free-form additive manufacturing of thermosetting epoxies is possible using RF-induced localized heating. The uncured resin left over in the reservoir after the printing process can be stored at lower temperatures to cease the cross-linking process, and to allow reusing the material whenever required.

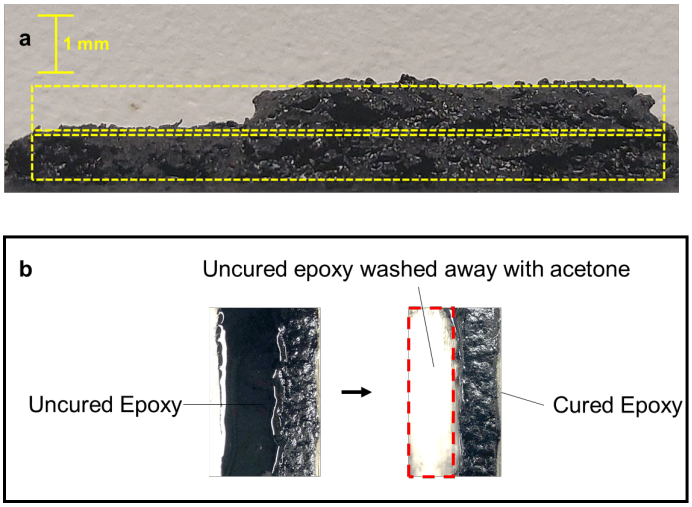

Figure 3.4: (a) The cross-sectional view of a multi-layer 1D print with a thickness of 0.8 mm for each layer, (b) Epoxy curing in a reservoir with selective, localized heating. The RF applicator was moved relative to a resin reservoir using a linear stage to induce localized heating and curing. Uncured resin in the reservoir washed away using acetone.

The print resolution is dictated by the applicator length scale and is expanded by the heat diffusion from the target heating zone to the surrounding resin. Mathematically, the diffusion length, the expansion in the print resolution due to heat diffusion, can be calculated using the following equation:

$$L = \sqrt{\alpha * t_{residence}} \qquad (3.4)$$

Here, α (~1e-7 m2/s) is the thermal diffusivity of the system and $t_{residence}$ is the residence time of 1 minute. Using these parameters, the diffusion length is calculated to be ~2.4 mm, which is similar to the observed experimental results. Experimental results show that using an applicator

with a length scale (or heating zone) of 4.25 mm, the maximum width measured on the printed part is 5.76 mm. This is 1.51 mm wider than the target zone (**Figure 3.5**).

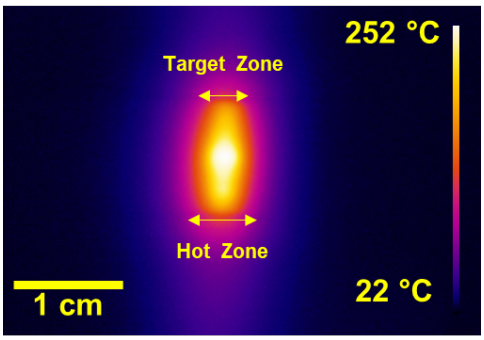

Figure 3.5: Target Zone and Hot Zone (due to diffusion) of the resin during RF Heating.

3.2.2. Characterization results

TGA measurements were performed to determine the degradation temperature of three samples cured using different methods: using (i) RF heating, (ii) RF heating followed by oven post-cure (kept in a pre-heated oven at 250 °C for 2 minutes after RF curing), and (iii) conventional curing in an oven (cured in an oven at 250 °C for 5 minutes). The results in (**Figure 3.6**) show that the degradation temperature for all three curing methods is approximately constant at 378 °C, thus, proving that thermal properties of the RF-cured sample are comparable to the conventionally cured sample.

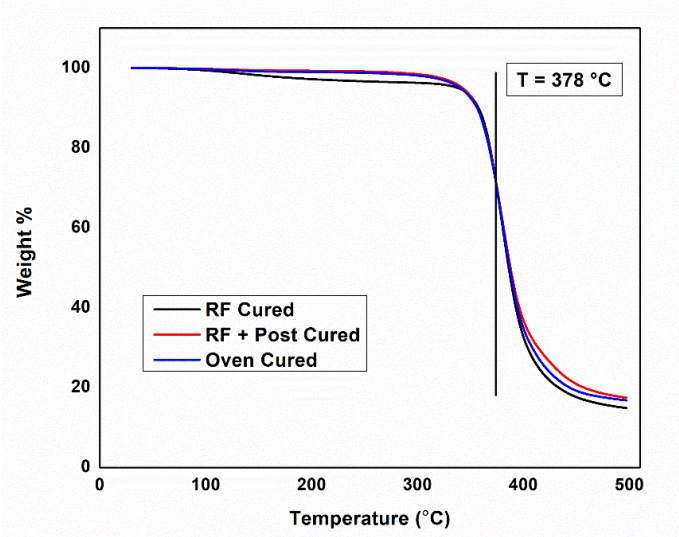

Figure 3.6: Thermo-Gravimetric Analysis (TGA) plots for samples cured using RF heating, RF heating followed by oven post-cure, and conventional oven curing.

We also examined the cured state of the printed samples to determine the glass transition temperatures of samples cured using the three methods described above: RF heating, RF heating followed by oven post-cure, and conventional curing in an oven. The DSC plots are shown in **Figure 3.7** (these samples correspond to linearly printed samples such as those in **Figure 3.3 (a)**). The glass transition temperatures of the three samples are shown in **Table 3.1**. The results show that RF cured sample has a glass transition temperature comparable to the conventionally cured sample; furthermore, post-curing does not make a significant impact on the thermal properties of the sample. This shows, again, that RF curing is self-sufficient to selective cure a structure with comparable thermal properties to a conventionally cured sample.

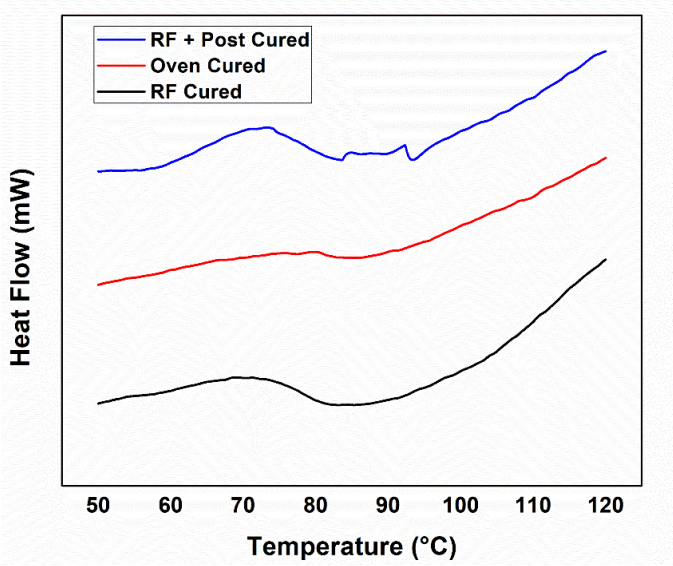

Figure 3.7: Differential Scanning Calorimetry (DSC) plots for samples cured using RF heating, RF heating followed by oven post-cure, and conventional oven curing.

Curing method	Glass Transition Temperature
RF heating	86.2 °C
RF heating + Post Cure	87.3 °C
Conventional Oven Cure	86.7 °C

Table 3.1: Glass Transition Temperatures measured using Differential Scanning Calorimetry for samples cured using RF heating, RF heating followed by post curing in an oven, and conventional oven curing.

Dynamic Mechanical Analysis (DMA) was performed to observe the thermo-mechanical properties of the samples cured using three methods: RF heating, RF heating followed by post-curing in an oven, and conventional oven curing. The tan δ peaks in **Figure 3.8 (a, b, c)** indicate that all three samples have comparable glass transition temperatures (~ 90 °C), which are also within ± 4 °C of the T_g values observed using DSC (~87 °C). Additionally, the RF cured sample has comparable E' values to the conventionally cured sample and the post-cured sample. This further demonstrates that the samples printed using RF curing method have similar thermal and mechanical properties compared to the conventional oven-cured or post-cured samples.

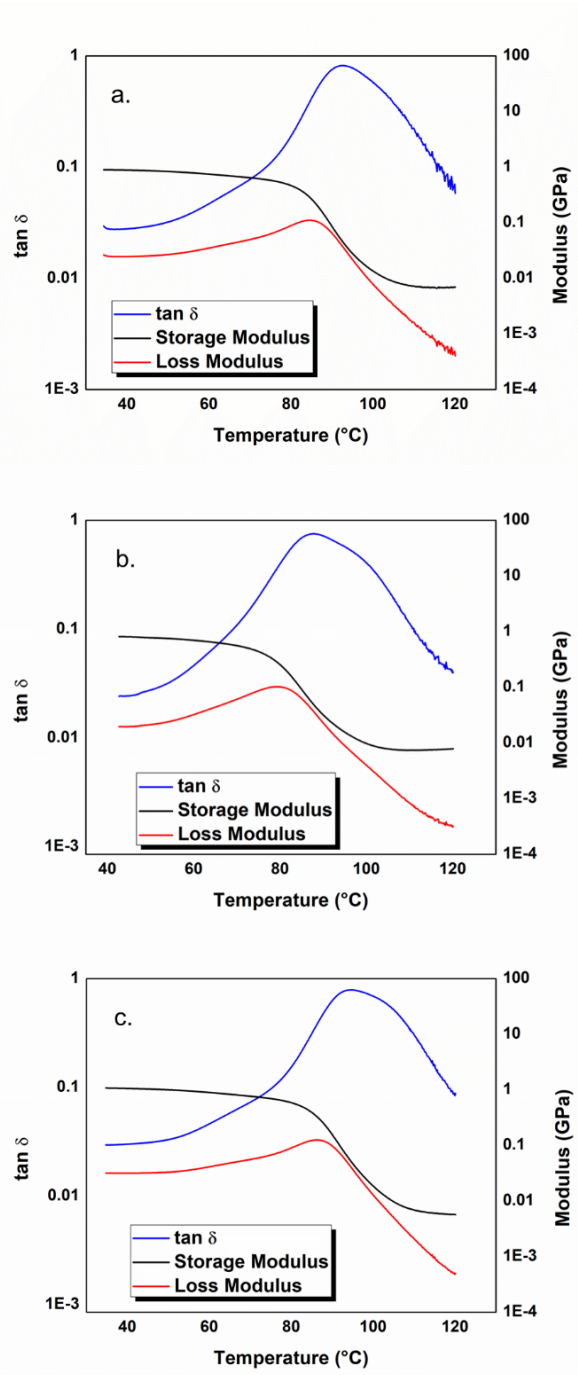

Figure 3.8: Dynamic Mechanical Analysis (DMA) plots for samples cured using (a) RF heating, (b) RF heating followed by oven post-cure, and (c) conventional oven curing. A 17.5 mm single cantilever beam procedure was followed at frequency of 1 Hz.

Scanning Electron Microscopy images of the cross-sections of samples cured using RF heating and conventional oven curing were captured. The images (**Figure 3.9**) portray that in case of RF heating, the volumetric heating results in fewer trapped voids inside the sample and a more uniform cross-section is observed compared to conventional curing in an oven. In the case of conventional oven curing, the convective nature of heating causes the outer layer of the sample to heat and cure before the heat flows to the interior layers. This results in the gases or air bubbles in the interior of the samples to remain trapped, thus, creating voids in the sample.

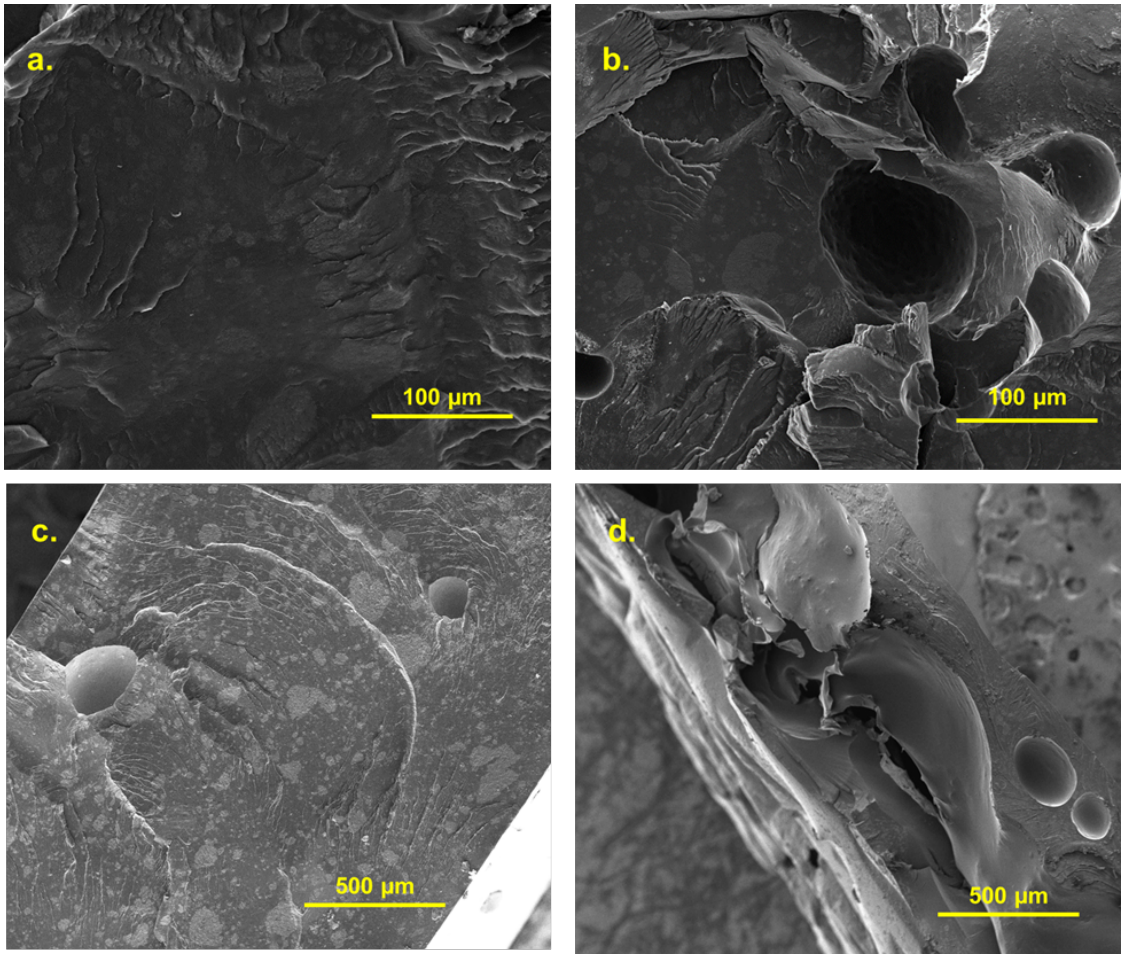

Figure 3.9: Scanning Electron Microscopy (SEM) images of cross-section of nano-filled epoxy sample cured using (a, c) RF heating, and (b, d) conventional oven curing.

Tensile testing was performed on RF cured and conventional over cured sample was performed. The results show that the ultimate tensile strength (UTS) of the RF cured sample (~ 2.9 MPa) was higher than that of the oven cured sample (~2.6 MPa) (**Figure 3.10**). The modulus value of the RF cured sample is also higher that the modulus for the oven cured sample. the better mechanical properties observed in RF cured samples can be attributed to fewer void formations in the sample due to the nature of volumetric heating. The internal-to-external heating and curing eliminates and pushed out most of the trapped gas, thereby, resucing the number of voids in the sample compared to conventional oven curing.

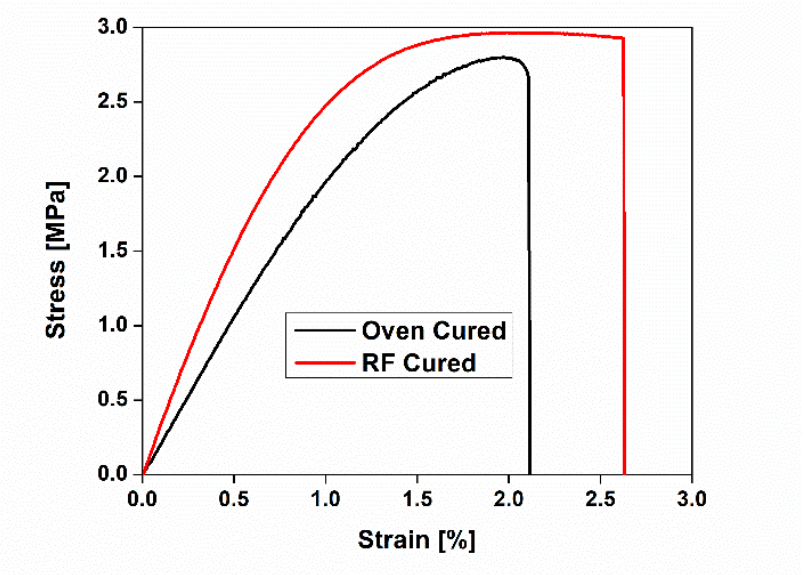

Figure 3.10: Mechanial Testing of samples cured using RF Heating and Oven Heating.

UV-vis spectroscopy was performed to quantify the stability of the CNT-filled epoxy system over time. The absorbance of the uncured resin was measured immediately after the sample was made, and 30 minutes after the sample was made. The absorbance values of the two runs are nearly overlapping (**Figure 3.11**), showing that the CNT-epoxy dispersion is stable over the 30-minute period after staple preparation, which is usually a sufficient amount of time for the printing process described in this work.

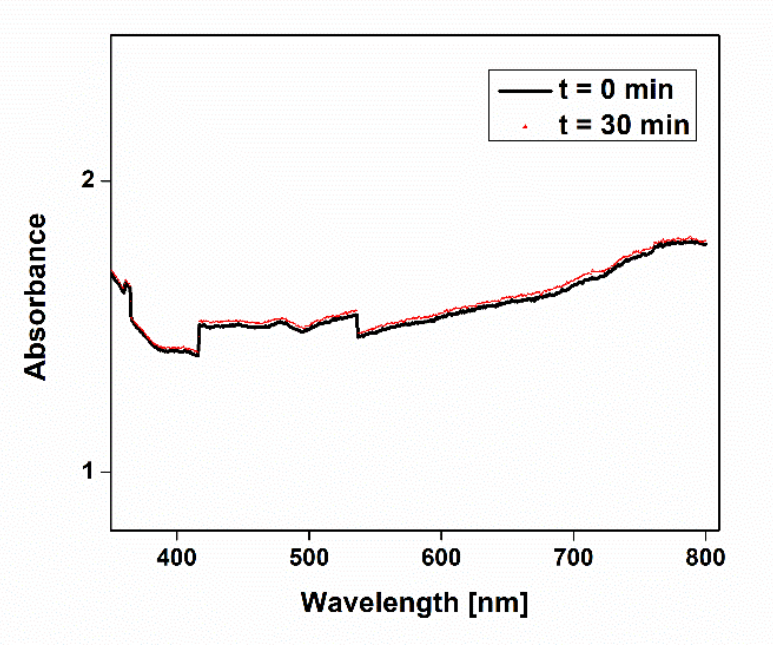

Figure 3.11: Absorbance vs wavelength of uncured resin immediately after making sample and 30 minutes after making the sample.

3.2.3. Simulation results

The spatiotemporal kinetics of a resin reservoir exposed to a moving heat source to print complex structures was modeled. The simulation computes the temperature and the percent of epoxy cured (referred to as conversion, or X) changing with time at each point in space. The experimental selective RF heating was mimicked in the simulation used a localized heat source with a specified path in space and time. The following simulations demonstrate the potential of this method for curing thermosetting epoxies using RF heating.

First, the model demonstrates the heating and curing of a stationary sample exposed to a localized heating source. This simulation allows for a reaction timescale comparison between the experiment and the model. The heat source does not move for this simulation, i.e., it remains in the same point in space, thereby curing a spot of epoxy. The temperature and conversion are computed as a function of time. The total time for the simulation was set to be 100 seconds, where the localized heat source was 'on' for the first 60 seconds only. The temperature of the heat source in the simulation mas modulated to be ~215 °C (**Figure 3.12 (a)**). The results **(Figure 3.12)** indicate that the spot exposed to the localized heat source required ~60 seconds to cure completely; this result corresponds to experimental results in **Figure 3.2**.

The exposure time of ~60 seconds was used as the residence time for later simulations, similar to the experiments. Here, the epoxy is sufficiently cured (~95%) to allow shape retention. The range of the heat source is a user defined input of 2 mm. The resolution of the printed structure in **Figure 3.12 (b)** is ~2.2 mm, which is approximately 10% greater than the input heat source range. The loss of resolution is due to conductive heat transfer within the resin reservoir which causes the curing to slightly expand beyond the input heat source path and range.

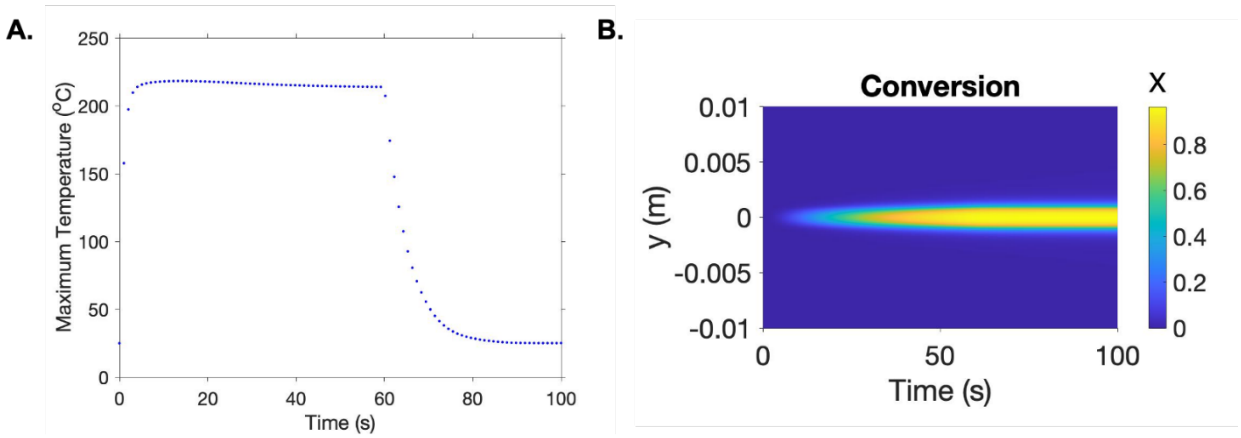

Figure 3.12: (a) Maximum temperature vs. time plot of localized heating and curing of a stationary resin sample (the power is on for 600 seconds). (b) Surface plot of conversion changing with time at fixed point in space (y-direction).

Next, we show how the movement of the heating source relative to the resin reservoir can be used to cure and extended part and a two-dimensional ring structure. For the extended part, the heat source was moved in the x-direction in a resin reservoir of dimensions 40 mm x 20 mm, forming an 18 mm line. The scan speed was calculated by dividing the range of the heat source (2 mm) by the residence time needed for curing (60 s). The heat source power in the simulation was modulated to maintain the temperature between ~210-250 °C (**Figure 3.13**). The resulting temperature and conversion are depicted as a function of space in **Figure 3.14** at 3 different times (this corresponds to experimental results in **Figure 3.3 (a)**). For the 2D ring structure, the heat source was moved in the x and y direction in a resin reservoir of dimensions 40 mm x 40 mm to print a circle with a radius of 10 mm. The heat source power in the simulation was modulated to maintain the temperature between ~210-250 °C **(Figure 3.15).** The

temperature and conversion are depicted as a function of space in **Figure 3.16** at 3 different times (this corresponds to experimental results in **Figure 3.3 (c)**). The results in **Figures 3.14 and 3.16** portray that the printed structures achieve a degree of cure greater than 90%. More importantly, the resin surrounding the printed structures remains uncured, which is critical for printing resolution and removal of the final printed structure from the resin reservoir.

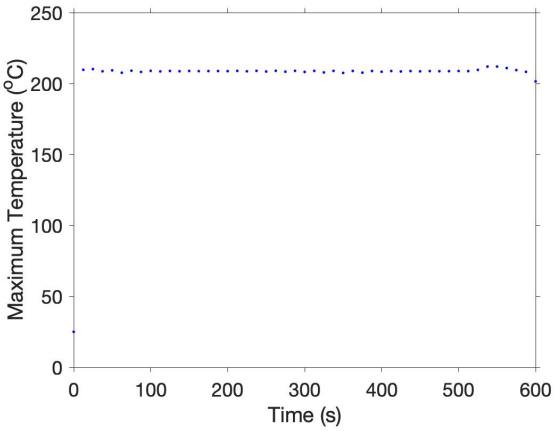

Figure 3.13: Maximum temperature vs. time plot of localized heating and curing of a 1D line with a length of 18 mm. This graph corresponds to Figure 3.14.

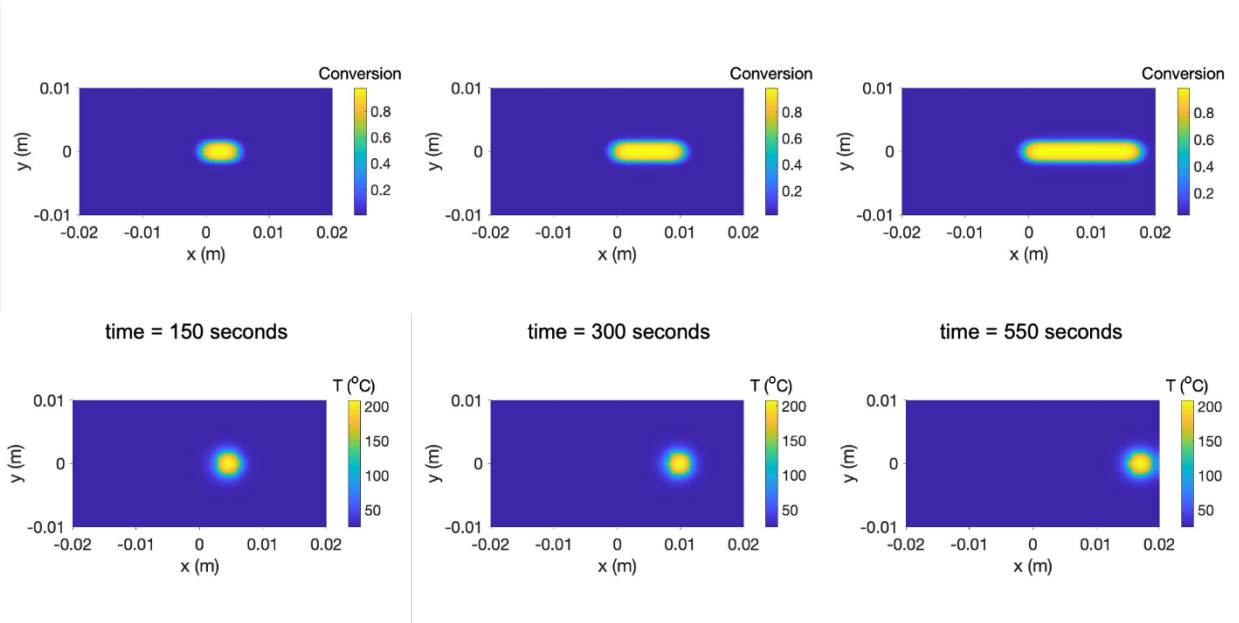

Figure 3.14: Surface plot of temperature and conversion changing with time (t = 150s, 300 s, 550 s) and space to print a 1D line with a length of 18 mm. The heat source was moved relative to the resin at a speed of 0.033 mm/s.

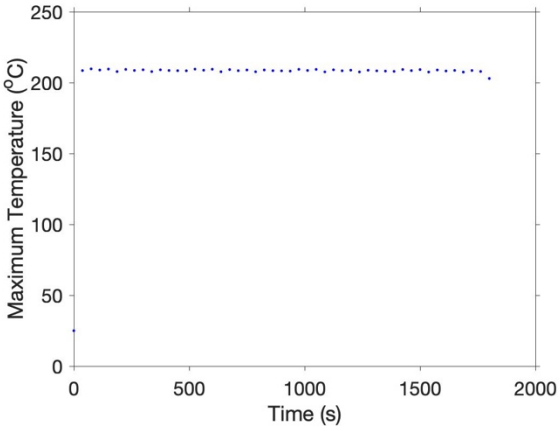

Figure 3.15: Maximum temperature vs. time plot of localized heating and curing of a 2D circle with a radius of 10 mm. This graph corresponds to Figure 3.16.

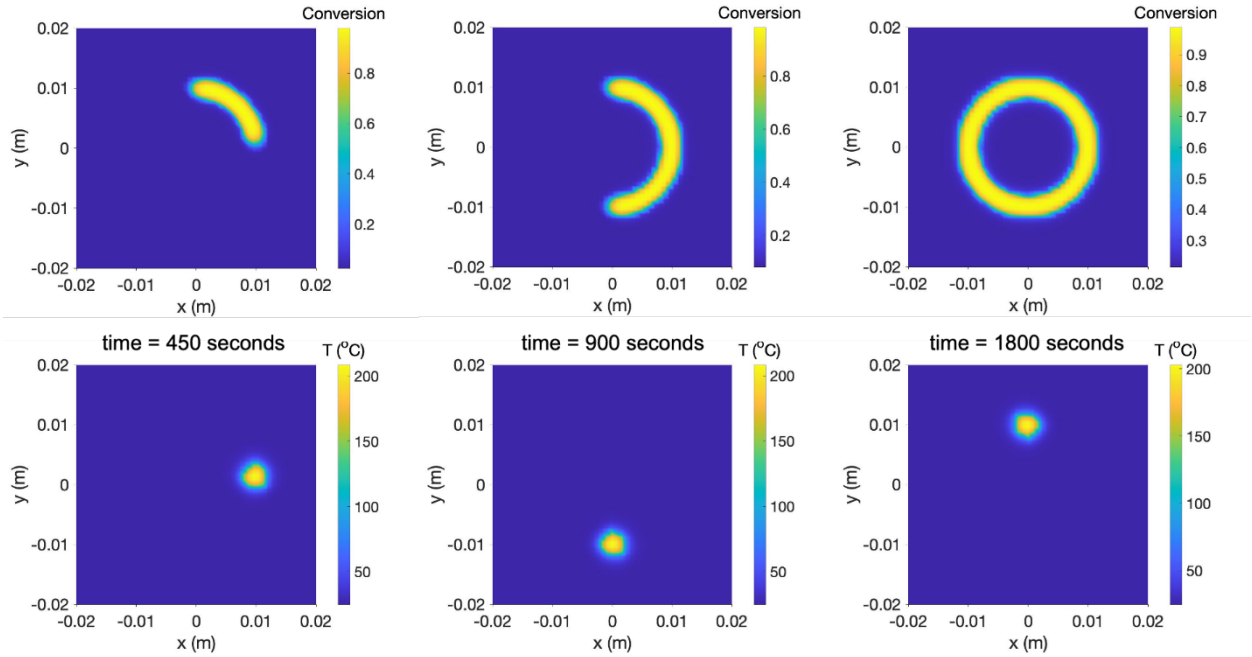

Figure 3.16: Surface plot of temperature and conversion changing with time (t = 450 s, 900 s, 1800 s) and space to print a 2D circle with a radius of 10 mm. The heat source was moved relative to the resin at a speed of 0.033 mm/s.

Here, we illustrate how complex shapes can be printed. In this simulation, the heat source moves in the x and y directions in a resin reservoir to print a Texas A&M logo. The conversion at the final time is depicted as a function of space in **Figure 3.17 (a)**. The surrounding resin remains uncured, which allows for the extraction of the printed structure from the resin reservoir while maintaining the resolution of the printed structure. The final printed structure post-curing and post-extraction is depicted in **Figure 3.17 (b)**. This figure is the surface plot of the spatial locations that have cured sufficiently to allow for the extraction of the printed structure from the resin

reservoir. Note that the resolution of the results is limited by the simulation mesh size rather than the heat source range. The final cured structure is remarkably similar to the input heat source path (**Figure 3.18**), allowing engineers to produce structures that are similar to the original CAD design.

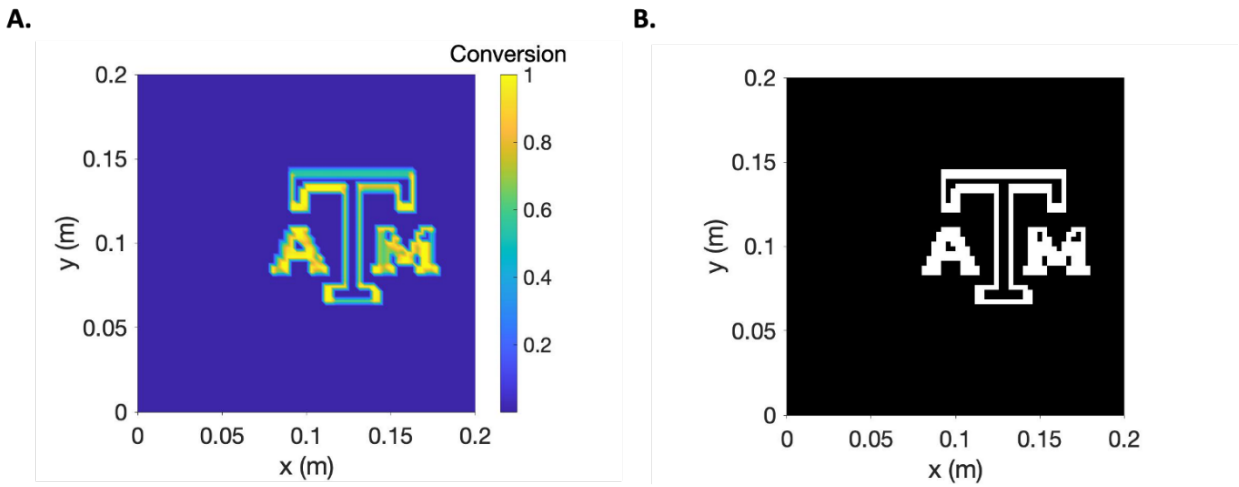

Figure 3.17: (a) Surface plot of conversion in space for the Texas A&M logo printed using localized heating and curing. Each letter of the logo was printed separately; (b) The post-cure and post-extraction surface plot of the final printed structure.

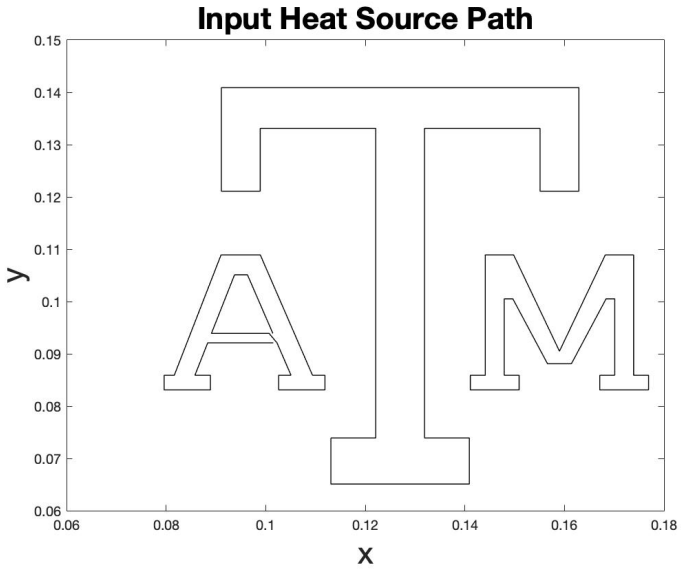

Figure 3.18: Plot of the x and y locations of the input heat source path.

This graph corresponds to Figure 3.17.

Lastly, we show that this method can also be used to create complex 3D structures. The heat source moves in the x and y directions in a resin reservoir as in the previous simulations; however, an additional movement upwards in the z-direction is added to achieve a 3D helical spring structure. **Figure 3.19** shows the wand path and the conversion map for the final printed structure.

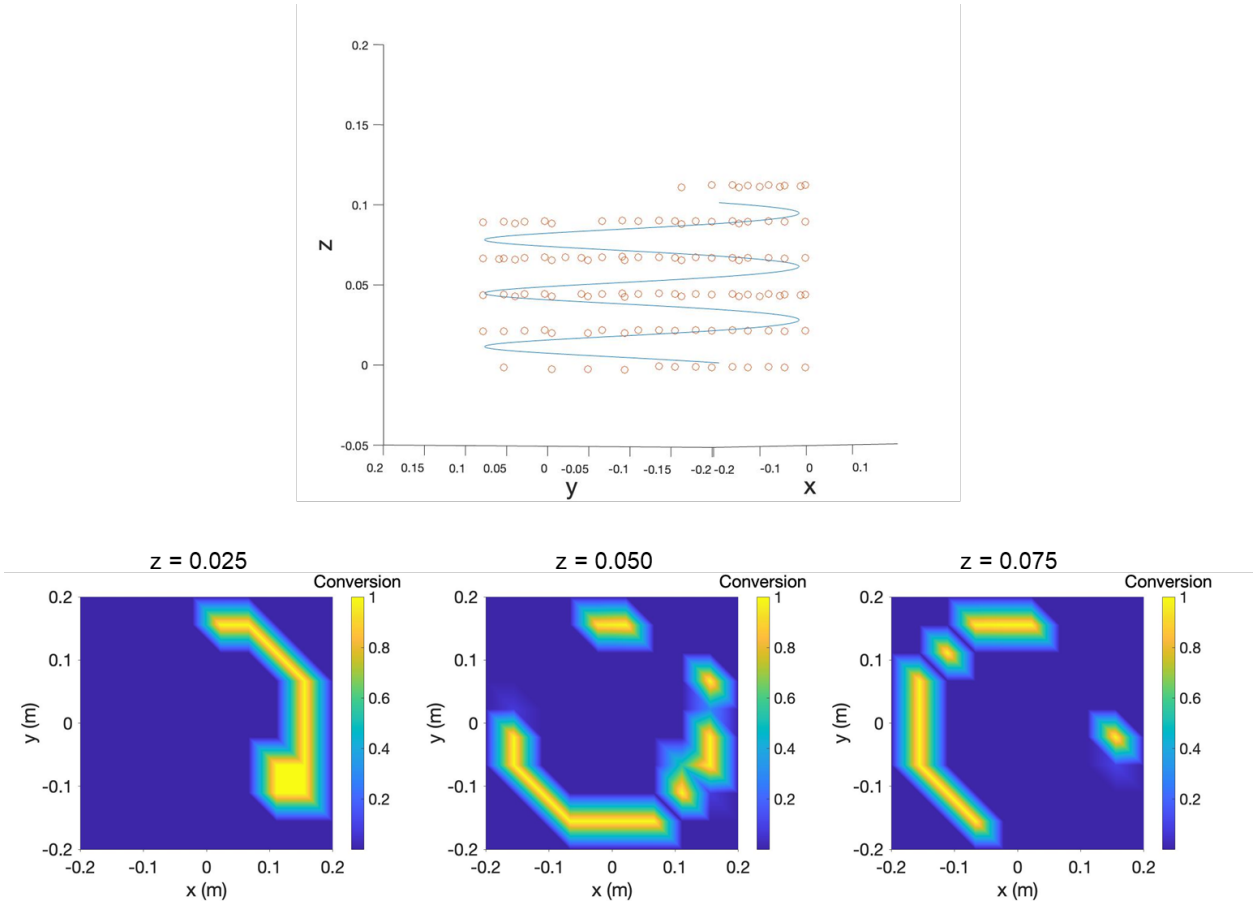

Figure 3.19: Simulation of 3D-printed helical spring: (Top) Plot of the (x,y,z) locations of the input heat source path for the 3D spring. Red dots indicate cured locations. (Bottom) X(x,y) at different z-slices for the final cured part.

3.3. Conclusion

Our results show that localized, radio-frequency heating can rapidly heat and cure thermosetting epoxies. In contrast to previous studies where free-form printing in a resin reservoir has been investigated, we demonstrated multi-layered printing of thermosetting epoxies based on localized heating rather than localized photopolymerization. Our RF-printed samples show superior mechanical properties compared to a conventional oven cured sample. The thermo-mechanical properties of an RF-printed sample are comparable to a conventionally cured sample of the same composition. Cross-sectional SEM images indicate a more uniform morphology in the sample volumetrically cured using RF heating. Furthermore, simulation results show that this additive manufacturing technique can be used for printing complex structures, eliminating the limitation of oven-curing in a mold. These findings show that localized heating and curing of thermosetting resins is possible using RF heating, addressing one of the longstanding problems in thermoset additive manufacturing.

Chapter 4: Additive manufacturing of thermosetting resins using Direct Ink Write printing and RF heating [In Progress]

Direct Ink Writing (DIW) is a widely used extrusion-based method for additive manufacturing where the liquid 'ink' is deposited along digitally defined paths. Conventional methods for DIW of thermosetting resins depend on the use of novel resin chemistries, viscosifiers, or long oven-curing schedules. Direct ink writing coupled with ultra-violet assisted curing can be used to 3D print light-sensitive resins; however, this alters the resin chemistry and has limited industrial applications [39, 40]. Other previous studies rely on the addition of viscosity modifying agents to make the resin shear-thinning, thereby allowing it to retain its shape while printing before transferring the printed structure to an oven for curing [41-44]. The increased viscosity can make these resins difficult to print; additionally, the 24-hour or longer oven curing schedules can introduce voids and possible distortions in the printed structure.

In this study, we demonstrate that the use of a co-planar RF applicator, which generates an electric field, to rapidly heat and cure DIW-printed, nano-filled epoxy composites. This novel method avoids the need for post-curing or ovens for manufacturing of thermoset parts. Our proposed method involves a layer-by-layer, print and cure cycle which allows for printing of high resolution, multi-layered structures. Each layer is partially cured using RF heating before a new layer is deposited; this allows the printed structure to maintain its integrity and hold its own weight as more layers are printed on top. Commercial epoxy resin with varied nano-filler loadings were examined as DIW candidates. Rheological characterization was used to assess curing kinetics and printing behavior. After printing, the thermo-mechanical properties, surface finish, and shape retention of RF-cured samples were evaluated and found to be comparable against

samples conventionally cured in an oven. This method of manufacturing establishes RF heating as a suitable alternative to conventional methods, thereby facilitating rapid, free-form processing of thermosetting resins.

4.1. Experimental methods

4.1.1. Materials

Bisphenol A diglycidyl ether (DGEBA) epoxide was heated at 60 °C in an oven to ensure uniform consistency, and cooled to room temperature before mixing. Jeffamine T403 polyetheramine was used as a low viscosity hardener. The epoxide and curing agent were mixed in a weight ratio of 100:49. Varied wt. % (between 3-7%) of multi-walled carbon nanotubes (MWCNTs) from Cheaptubes were added to the resin. To ensure uniform dispersion, the epoxide, curing agent and MWCNTs were mixed using a planetary mixer for 10 minutes, and degassed in a vacuum oven for 20 minutes.

4.1.2. Rheology

Rheological measurements were performed using a stress-controlled rheometer (Anton Paar, MCR 301) at room temperature (at ~24-25 °C) with a 25 mm diameter stainless steel top fixture and a 50 mm disposable aluminum plate bottom fixture with a gap of 0.1 mm. Rheological properties of uncured candidate resins were evaluated prior to printing.

An oscillatory amplitude sweep at constant temperature (25 ˚C) and frequency (1 Hz) was used to determine the yield stress of the uncured resin at varied CNT loadings.

A three-step steady-shear thixotropy test was conducted to mimic extrusion from the print-head and to determine time-dependent recovery behavior of the resins. There are three

regions in this test: an initial rest period (0.01 s^{-1}), a high shear-rate step (1000 s^{-1}), and the recovery period (0.01 s^{-1}).

4.1.3. RF setup and frequency sweeps

A stationary, co-planar radio frequency (RF) applicator fabricated by laser-etching copper traces on FR4 substrate was used for this experiment. RF waves were generated using a RIGOL DSG15 signal generator and amplified using a PRANA GN 500 amplifier and supplied to the applicator using a coaxial cable, resulting in a fringing field coming out-of-plane of the applicator.

RF frequency sweeps were used to determine the maximum heating rate for each candidate resin. In this experiment, a constant RF power of 1 Watt was supplied to the samples with a thickness of ~2 mm. The maximum temperature was recorded using a thermal camera (FLIR Systems, Inc., A655sc). Each sample was exposed to a heating cycle for 1 second followed by a rest period of 13 seconds at each integer frequency value between 0-200 MHz. The heating rate for each heating cycle was calculated using the data collected before heating and once the temperature of the resin reached a maximum.

4.1.4. Printing process

The HyRel Engine Standard Resolution direct ink writing printer was used for printing experiments. The prepared sample was loaded into a 15-cc dual-gasket stainless cartridge for a HyRel EMO-XT print head (Hyrel 3D; Norcross, GA) with nozzles of sizes 0.6-0.86 mm (from Structur3D) attached to the print head. For each printed structure, the CAD files were created using Solidworks, and converted into g-codes using Hyrel's Repetrel software in conjunction with Slic3r.

After each layer was printed, the sample was transferred to the RF applicator and partially cured at ~150 °C for 45-60 seconds. The target temperature of ~150 °C was maintained by manually modulating the RF power. This print-and-cure cycle was repeated for each layer (**Figure 4.1**). The final structure was cured completely at ~150 °C for 10 minutes after the last layer was printed.

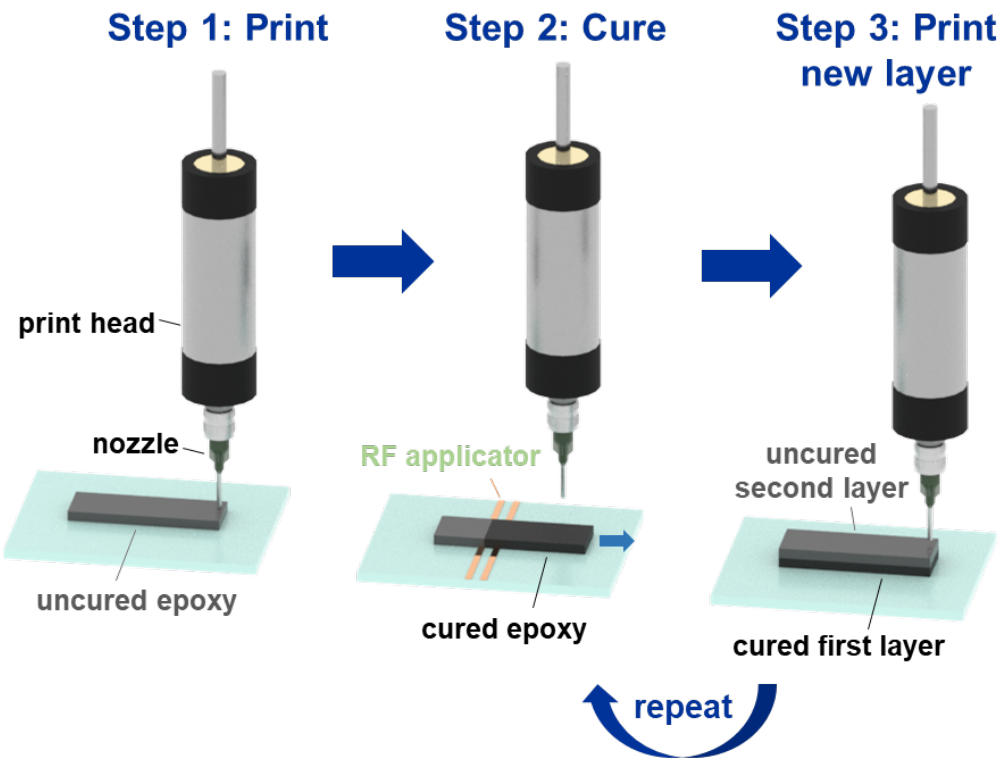

Figure 4.1: Schematic representing the direct-ink write printing process using radio-frequency assisted heating and curing. Step 1 represents the DIW printing process; step 2 demonstrates the RF heating and partial curing process; and step 3: shows the deposition of a new printed layer, after which the print-and-cure cycle is repeated.

4.1.5. Characterization

Dynamic Mechanical Analysis. Dynamic Mechanical Analysis (DMA) was performed using a TA Instruments DMA 850 to measure and compare the thermo-mechanical properties of RF cured and conventionally cured samples. Moduli change as a function of temperature was observed using a 35 mm dual cantilever test for both samples with a temperature ramp from 35 °C to 120 °C, at a rate of 3 °C/min. A strain of 0.04 % and frequency of 1 Hz was set for all the tests.

Mechanical Testing. Longitudinal tensile testing was conducted on ASTM D638 type IV tensile bars cured using RF heating and conventional ovens using an Instron load frame with a 30 kN load cell. The displacement rate was set to be 2 mm/min. The raw data of Load, F [N] vs Displacement, d [mm] was converted to Stress σ [N/m^2] vs Strain ε [%], and ultimate tensile strength was compared for tensile bars made using either curing method.

Scanning Electron Microscopy. Cross-sectional morphology of samples cured using RF heating and conventional oven heating were observed using a FEI Quanta 600 FE-SEM.

4.1.6. Simulation

The model described below was discretized using the finite difference method and solved using a built-in implicit solver (with a mass matrix) in MATLAB R2021b.

The simulations are two dimensional (x-z) and the thickness of the printed structure is assumed to be negligible in the y-direction. The spatiotemporal kinetics are described by two ordinary differential equations. The modified Kamal-Sourour equation was used to model the reaction kinetics (**Equation 4.1**) [24].

$$\frac{dX}{dt} = (kX^m)(1-X)^n \qquad (4.1)$$

Here, *dX/dt* is the curing rate, *X* is the degree of cure, *k* is the temperature-dependent reaction rate constant, and *m* and *n* are empirical reaction constants that reflect reaction orders and define the initiation and propagation stages of curing, respectively. The parameters in **Equation 4.1** (*k*, *m*, and *n*), were determined using DSC experiments in the temperature range of 80-110 °C. The data collected from these experiments was fitted to the modified Kamal-Sourour equation, and the activation energy was calculated to be ~33 kJ/mol using the Arrhenius equation. The calculated activation energy was used in the model to compute *k* as a function of local temperature.

The energy balance for the model is as follows:

$$\frac{dT}{dt} = \alpha \nabla^2 T + Q_{ext} + \frac{\Delta H_{rxn}}{C_p} + Q_{RF}(x, z) \qquad (4.2)$$

Here, *dT/dt* is the rate of change in temperature, the $\nabla^2 T$ term indicates heat conduction within the resin, and the ΔH_{rxn} term accounts for the heat generated by the exothermic curing reaction. Material functions like the thermal diffusivity (α) and the heat capacity (C_p) are matched to the epoxy resin itself.

The thermal transport in the y direction is described by the Q_{ext} term, which includes the heat losses to surroundings via convection to the air through the front and back of the sample (**Figure 4.2**). These are written as

$$Q_{ext} = 2 \times \left[\frac{h}{\rho \, C_p h_{resin}} \, (T - T_{air}) \right] \qquad (4.3)$$

Here, *h* is the convection coefficient for air (~30 W/(m^2 K)), ρ is the density of the resin (900 kg/m^3), C_p is the heat capacity of the resin (~2000 J/(kg · K)), h_{resin} is the height of the resin in the

reservoir (1 mm), T is the temperature at a node, and T_{air} is the temperature of air in the room. The temperature of the atmosphere and the underlying substrate were assumed to be 298 K.

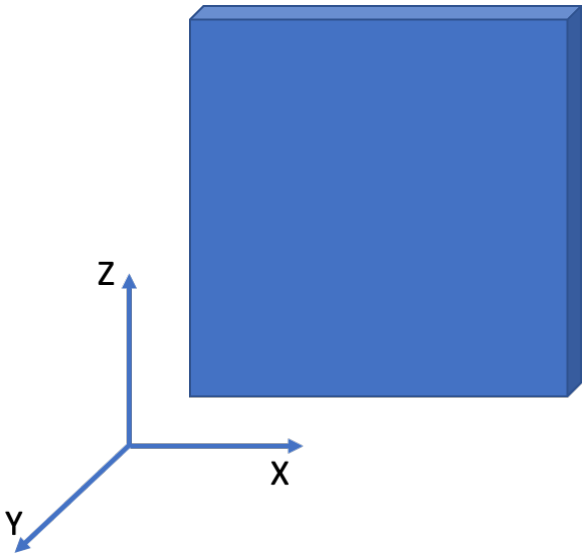

Figure 4.2: Schematic of simulation system. A two-dimensional (x-z) system with thermal transport (Q_{ext}) in the y-direction.

The Q_{RF} term indicates the volumetric heat source due to the RF field. We describe this field using a simple approximation: If a given location (x, z) is within a user specified range of the RF field source, then this term is turned on. Just as the RF power was modulated in the lab experiment to keep the maximum temperature of the resin in the range of 130-150 °C, the model

similarly employs proportional control of the Q_{RF} term with a steady-state gain of 1 based on the maximum temperature of the resin reservoir.

The boundary conditions of the system are as follows: the system experiences heat loss via convection through the sides and the top (in the positive and negative x-direction, and in the positive z-direction), and conduction to a glass substrate through the bottom (in the negative z-direction).

The boundary conditions of the system are as follows: the system experiences heat loss via convection through the sides and the top (in the x-direction, and in the positive z-direction), and conduction to a glass substrate through the bottom (in the negative z-direction). These conditions are valid for a structure like a rectangular wall that encompasses the defined system, but in order to print complex shapes like a pyramid or turret, the simulation needs to identify when and where the resin is deposited. At time = 0 seconds, the system is composed of air, and the simulation uses an external function to calculate the time when resin is deposited, and at which (x,z) location. This computed time is used to distinguish the locations where the system is composed of air and epoxy by applying **equations 4.1-4.3** only in the spots where the resin is deposited to model the printing and curing processes.

For printing cylindrical structures, the boundary conditions mentioned above were changed to periodic boundary conditions. The printed structure can be curved to model a three-dimensional open cylindrical structure.

For printing structures that utilize a sacrificial material, the simulation uses the aforementioned (x,z) location and an additional vector input that identifies which material, resin or sacrificial, is being printed. This would be similar to having two separate print heads which

switch based on the input g-code. The sacrificial material is assumed to be a thermoplastic that has similar thermal properties as our base resin; it can be dissolved using a solvent from the final structure, and it does not cure.

4.2. Results and Discussion

4.2.1. Ink properties (Rheology results)

The DIW printing process can be divided into four major sections: (1) static (rest) state inside the print head; (2) shear flow inside the nozzle; (3) high shear extrusion inside the nozzle and (4) static (rest) state on the print bed. An ideal DIW ink should be a stable viscoelastic solid at rest, should flow when subjected to shear stress and recover its properties once high shear stress is removed.

The rheological properties of the resin with different CNT loadings were investigated to determine a suitable ink for our DIW system. **Figure 4.3** shows that there is an increase in yield stress of CNT-filled resin with increase in CNT loading. A very low yield stress will mean that the uncured resin will collapse without any resistance to deformation; however, a very high yield stress is also not preferable as it will be difficult to extrude from the printer nozzle.

Next, a three-interval thixotropy test (3ITT) was performed to determine the recovery in viscosity of the resin after exposing it to high shear. The results in **Figure 4.4** show that the percentage in recovery of viscosity increases with increase in CNT loading. A high viscosity post shear is preferred because it enables the printed part to hold its shape and maintain resolution.

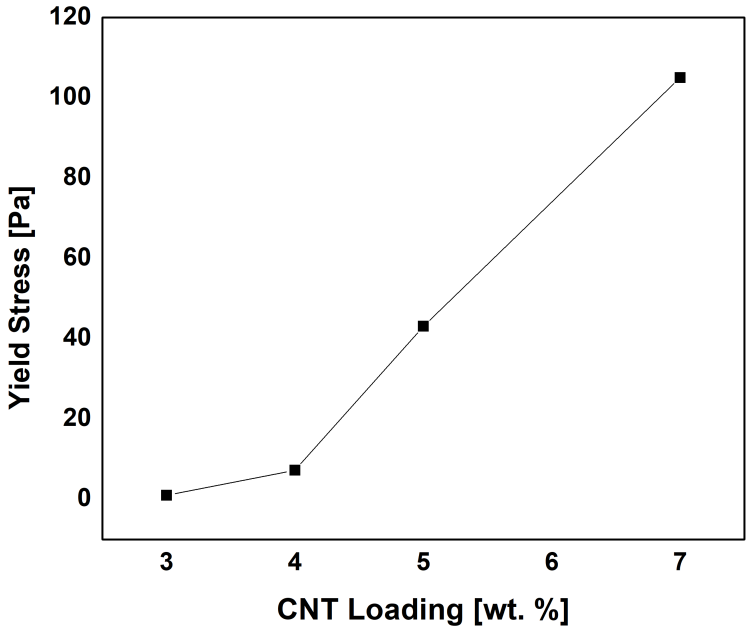

Figure 4.3: Yield stress obtained from oscillatory stress sweeps for varied CNT loadings (3 wt.%, 4 wt.%, 5 wt.%, and 7 wt.%).

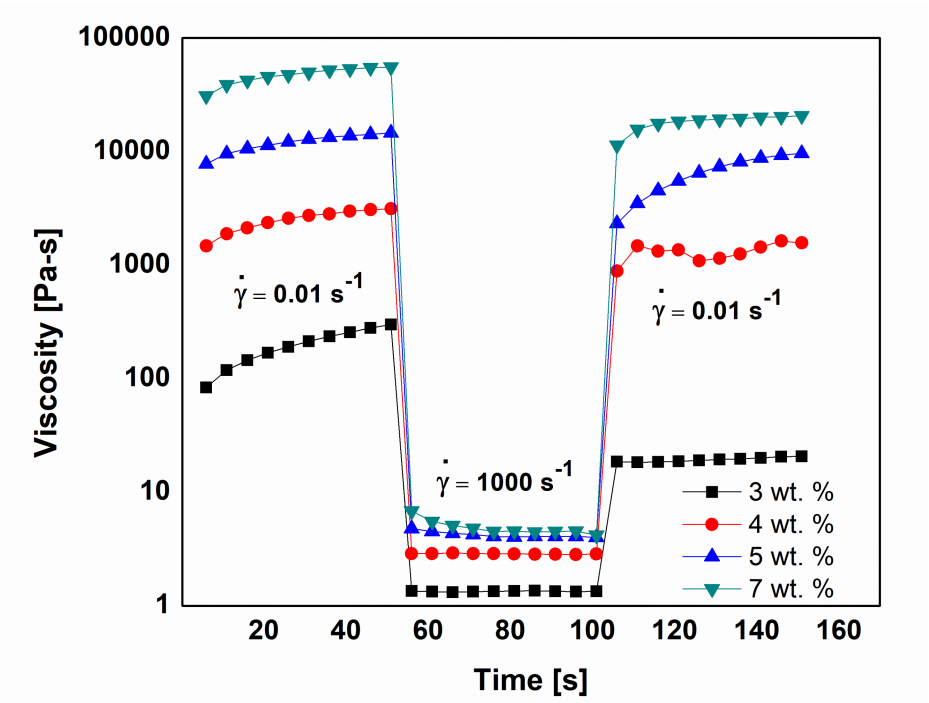

Figure 4.4: Three interval steady-shear thixotropy results for varied CNT loadings (3 wt.%, 4 wt.%, 5 wt.%, and 7 wt.%). The three regions in this test are as follows: an initial rest period (0.01 s^{-1}), a high shear-rate step (1000 s^{-1}), and the recovery period (0.01 s^{-1}).

The sample with 3 wt.% CNT loading showed low yield stress and poor recovery of storage modulus and viscosity modulus post high shear, making it unsuitable for printing. Samples with 5 wt.% and 7 wt.% CNT loading have a high yield stress and good recovery of storage modulus and viscosity values; however, with very high viscosity and yield stress values, these inks can be difficult to extrude and print from the DIW nozzle. Thus, a loading of 4 wt. % CNT was chosen for all printing experiments because it had a reasonable yield stress and showed good recovery of G' and viscosity values post high shear.

4.2.2. Ink heating properties

Frequency sweeps on epoxy-CNT sample at different CNT loadings showed that there is a rise in RF response with increase in CNT loading. This can be observed by the instantaneous heating rate observed for each sample when exposed to RF. The plot of heating rate as a function of CNT loadings is shown in **Figure 4.5**. While 3% shows very low RF response, the other loadings (4, 5 and 7%) show acceptable heating rates required for our layer-by-layer RF heating process. Due to rheological constraints, 5 and 7% CNT loaded resins cannot be used for printing; thus, 4% CNT-loaded resin was chosen for printing.

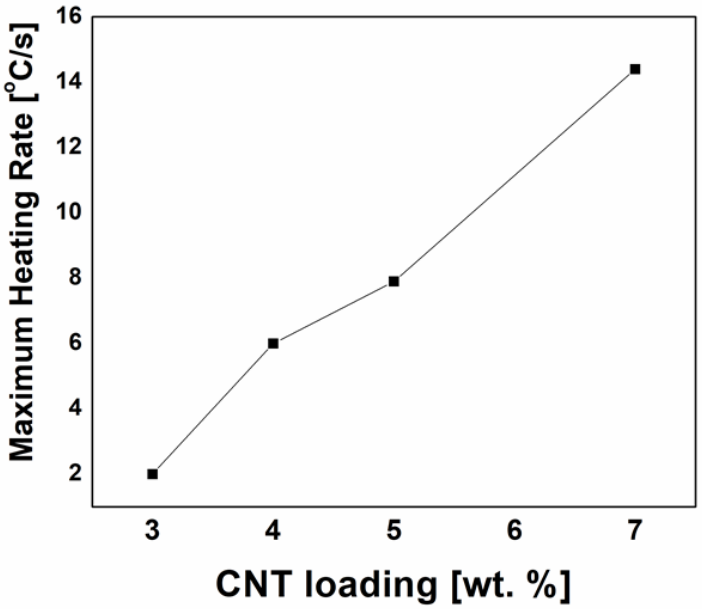

Figure 4.5: Maximum heating rate calculated for for varied CNT loadings (3 wt.%, 4 wt.%, 5 wt.%, and 7 wt.%). Radio-frequency sweeps were performed with a constant power of 1 watt and frequencies ranging from 0-200 MHz.

4.2.3. Printing and Characterization results on printed dog bones

Dynamic Mechanical Analysis (DMA) results show that the elastic moduli of samples cured conventionally in a mold is similar to the elastic moduli of the sample that was DIW printed, and RF cured (**Figure 4.6**). Furthermore, we see a higher glass transition temperature for the RF cured sample (87.5 °C) compared to the conventionally cured sample (79.3 °C). The higher glass transition temperature observed for RF cured sample could be because a higher degree of cure can be achieved using volumetric RF heating for the same target temperature and residence time.

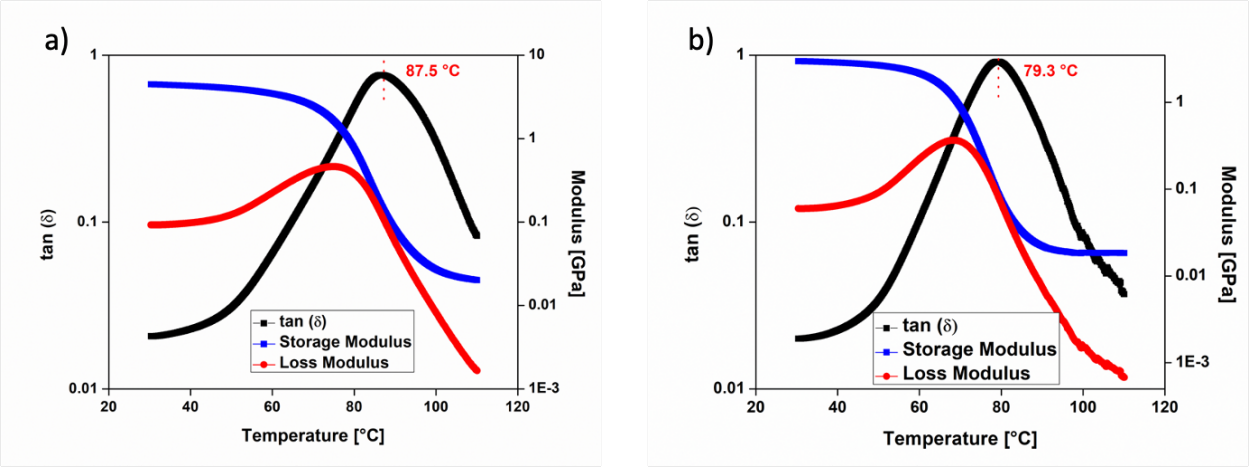

Figure 4.6: Dynamic Mechanical Analysis (DMA) plots for samples manufactured using (a) DIW printing and RF heating and curing, and (b) conventional oven curing in a mold. A 35 mm dual cantilever beam procedure was followed at frequency of 1 Hz.

The cross-section of samples manufactured using RF heating and conventional curing were observed using SEM. RF heating is a volumetric heating method, therefore, the sample heats from inside-to-outside, which eliminates trapped air bubbles and results in a smooth morphology (**Figure 4.7 (c, d)**). The results also highlight that distinct printed layers are not visible in the cross-sectional morphology. This indicates that the print-and-cure cycle using RF heating to partially cure each layer allows for sufficient inter-layer adhesion. On the other hand, conventional curing employs convective heating to cure the sample, thus, the outer layer of the sample cures first; this traps air bubbles inside the final part, and results in voids in the sample (**Figure 4.7 (a, b)**).

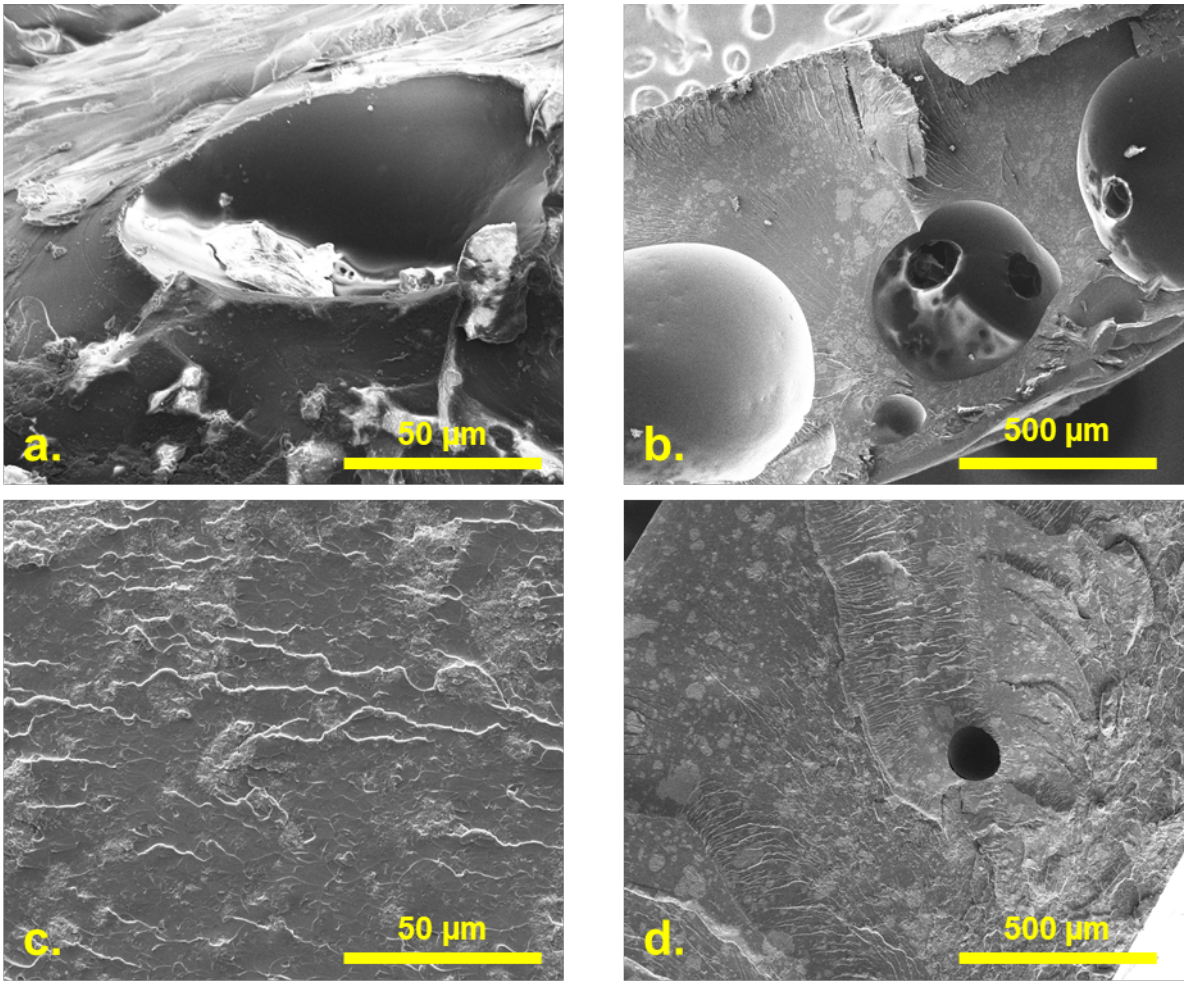

Figure 4.7: Scanning Electron Microscopy (SEM) images of cross-section of nano-filled epoxy sample manufactured using conventional oven curing in a mold (a-b), and DIW printing and RF heating (c-d).

Mechanical properties of ASTM D638 Type IV tensile bars manufactured via (i) Direct Ink Writing with RF heating, and (ii) conventional oven curing in a mold were measured and compared. The DIW printed samples that were cured using RF heating had a tensile strength of ~23.1 MPa, while conventionally made samples yielded a tensile strength of ~18.6 MPa (**Figure 4.8**). The slightly higher tensile strength of RF cured samples could be attributed to a lower void fraction in volumetrically cured samples compared to conventionally cured samples.

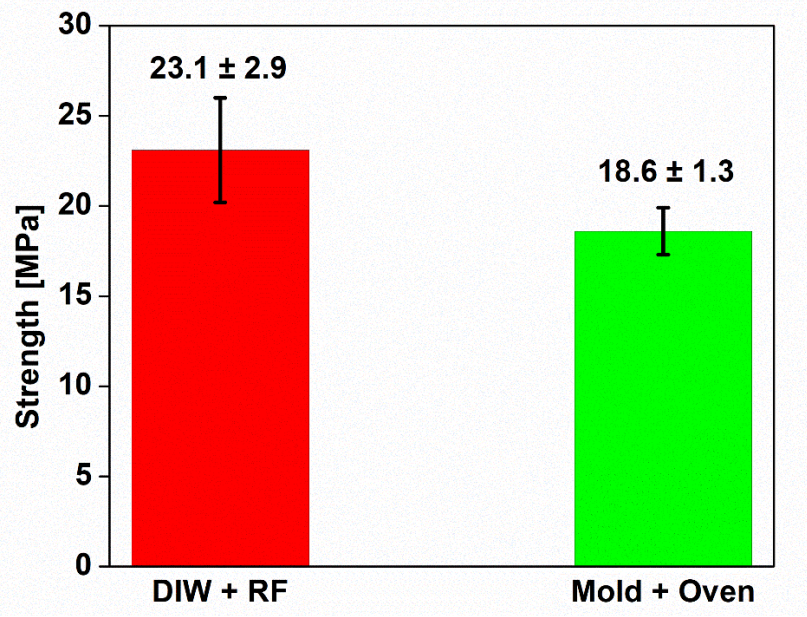

Figure 4.8: Tensile testing results for ASTM D638 type IV tensile bars manufactured using DIW printing and RF heating, and conventional oven curing in a mold using an Instron load frame with a 30 kN load cell at 25 °C.

4.2.4. Printing results

Here, we demonstrate our new method for DIW printing and RF curing of thermosetting epoxies using a print-and-cure cycle. We first compared the print quality, shape retention and the ability of the structure to yield the weight of subsequent printed layers with and without partial RF curing after each layer was printed. The results in **Figure 4.9 (a and b)** show a printed wall without RF heating after each layer and with RF heating after each layer respectively. We observed that the structure collapsed after 6 printed layers when it was not partially cured using RF heating. On the other hand, the printed structure that was RF heated after each layer was able to maintain height without collapsing for 10 layers. These results demonstrate that partial cure using RF heating allows the shape to support the weight of subsequent layers.

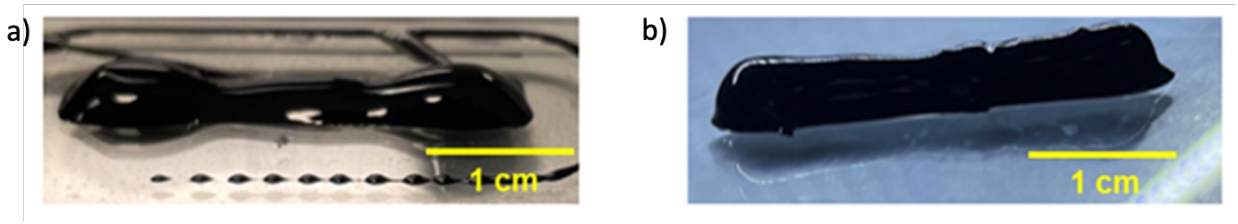

Figure 4.9: Wall printed (a) without RF partial cure after each printed layer (collapsed after 6 layers), and (b) with RF partial cure after each printed layer (structure did not collapse after 10 printed layers).

We printed various complex shapes to demonstrate different aspects of print quality. The first shape (**Figure 4.10 (a)**) is a single-trace hexagon with 3 printed layers of height 0.1 mm per layer. The corners in the hexagon are distinguishable, but some rounding of the corners is noticeable. Currently, we are optimizing the printing parameters for sharper corners. Next, we printed a cylinder (**Figure 4.10 (b)**). The cylinder printed has a height of ~3.8 mm with 14 printed layers of height 0.3 mm per layer. This print demonstrates the ability of our 3D printing method to print multi-layered structures that can support their own weight without collapsing. As observed in **Figure 4.10 (b)**, there is some rounding of the structure on the top surface, suggesting that our partial cure process has room for optimization and is a work in progress. Lastly, we also printed a gear with a height of ~0.3 mm with 3 printed layers of height 0.1 mm per layer (**Figure 4.10 (c)**). This exhibits the potential of this method in printing complex structures; we can improve upon the resolution of the printed structure and achieve sharper corners by optimizing the printing parameters.

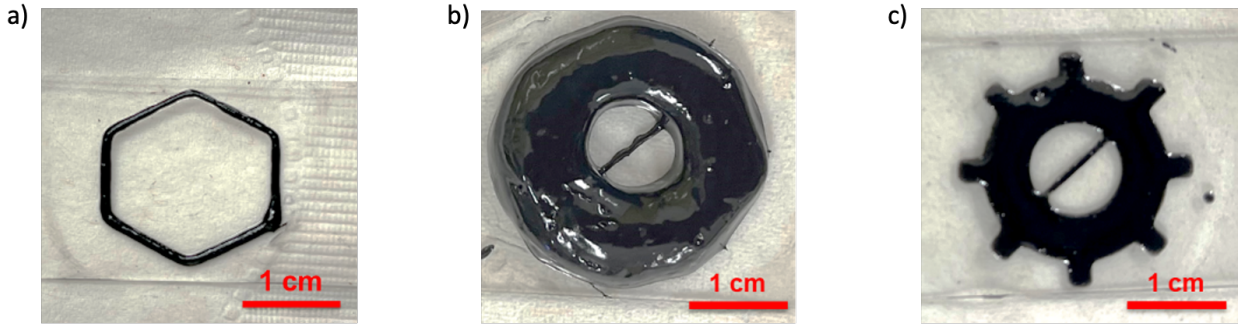

Figure 4.10: Structures manufactured using direct-ink write printing and RF heating and curing. (a) Single-trace hexagon with 3 printed layers of height 0.1 mm per layer. (b) Cylinder with 12 layers of height 0.2 mm per layer. (c) A complex gear print with 3 layers of height 0.1 mm per layer.

4.2.5. Simulation Results

The spatiotemporal kinetics of a resin reservoir exposed to a moving heat source to print complex structures was modeled. The simulation computes the temperature and the percent of epoxy cured (referred to as conversion, or X) changing with time at each point in space. The localized RF heating was mimicked using a localized heat source with a specified path in space and time. The purpose of the following simulations is to demonstrate the potential of this method for curing thermosetting epoxies using DIW printing and RF heating.

The model first demonstrates the DIW printing, and RF heating and curing of thermosetting epoxy sample with 4 wt.% CNT. For this simulation, the movement of print-head and heat source form a wall structure with a layer height of 0.001 m. The temperature and conversion are computed as a function of time. The total time of the simulation was set to 7000 seconds, where the heat source was ‘on’ for 5350 seconds and was turned off for the remaining

time. The temperature of the heat source in the simulation mas modulated to be ~140-150 °C. The scan speed was calculated to allow each spot to cure ~60-70% at 150 °C. The resulting temperature and conversion are depicted as a function of space in **Figure 4.11** at 3 different times.

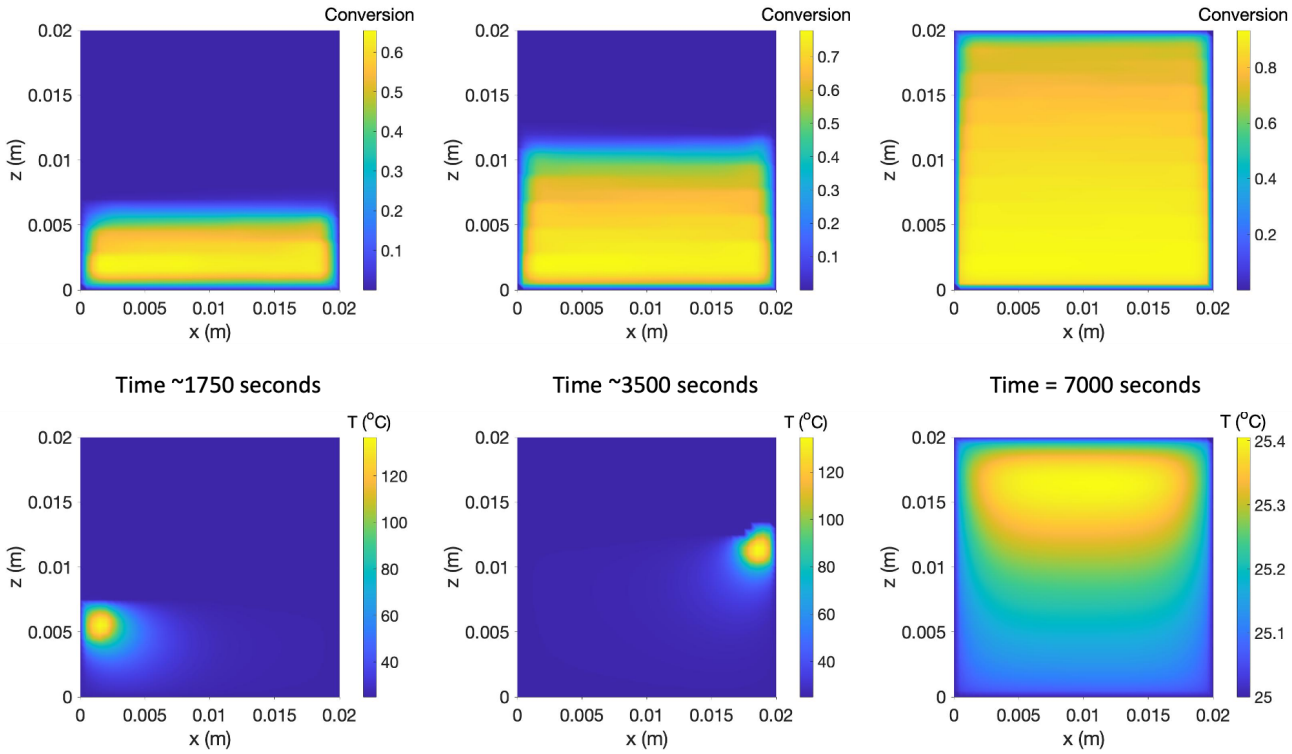

Figure 4.11: Surface plot of temperature and conversion of a wall changing with time (t = 1750 seconds, 3500 seconds, 7000 seconds) and space.

Similarly, another wall structure was simulated with a layer height of 0.002 m (**Figure 4.12 (b)**). The total time of the simulation was set to 3500 seconds, where the heat source was 'on' for 2800 seconds and was turned off for the remaining time. All other input parameters remain the same as previous simulation. **Figure 4.12** shows a comparison of conversion at final time of the two wall structures. Collectively, the results in **Figures 4.12 (a) and 4.12 (b)** demonstrate that printing parameters like layer height can have a significant impact on how well the structure cures, as well as how presence of gaps in conversion within the structure can reduce the maximum achievable structure height. Thus, in addition to resin properties, the printing parameters can affect the printing resolution as well as the quality of the final printed structure.

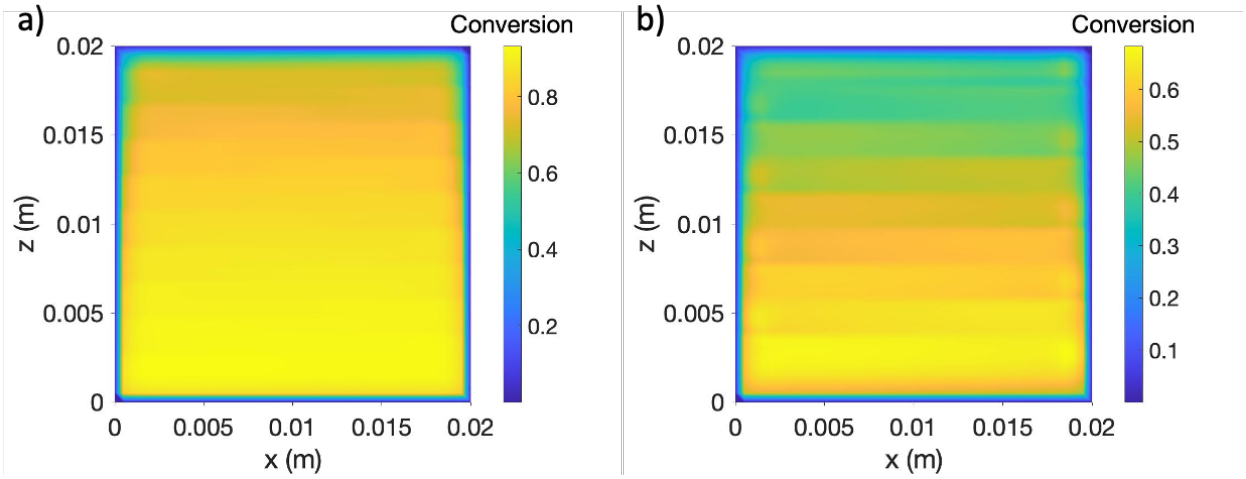

Figure 4.12: Surface plot of conversion of a wall as a function of space at final time. The structures have a layer height of (a) 0.001 m, and (b) 0.002 m. Other parameters like residence time, target temperature, and system parameters remain unchanged.

Next, we show the potential of this method in printing three dimensional shapes like a cylinder with a small thickness. This simulation follows the same parameters as the wall in **Figure 4.11**; however, the boundaries in this simulation are periodic, thereby simulating a 3D cylinder via a 2D simulation neglecting curvature effects. The results in **Figure 4.13** show conversion at final time (**Figure 4.13 (a)**), as well as temperature at the half-way time (**Figure 4.13 (b)**). The temperature plot demonstrates the periodic boundary conditions by showing the heat transfer from one side to the other when the heat source is at a side boundary.

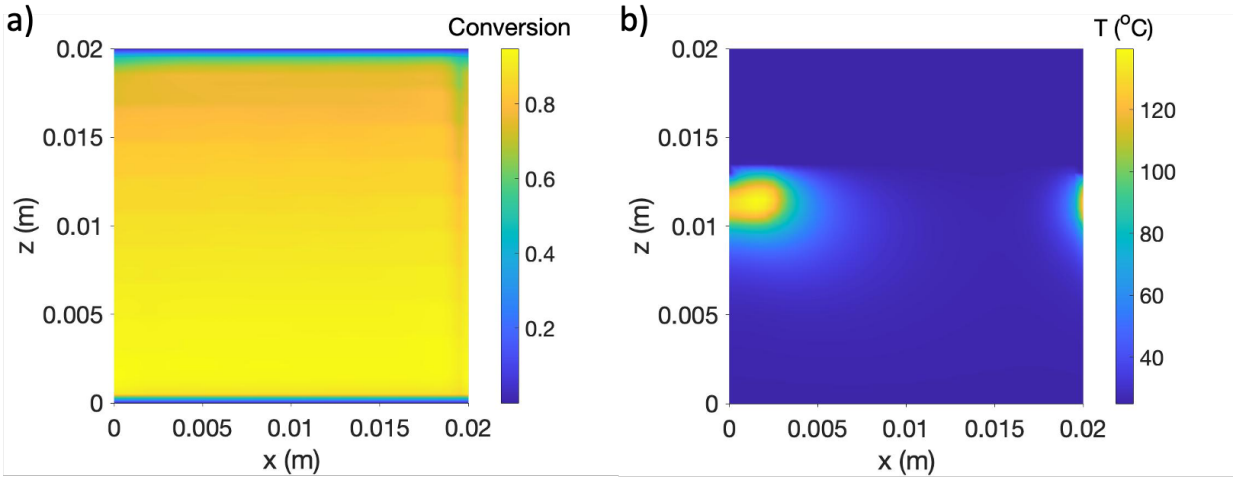

Figure 4.13: (a) Surface plot of conversion of a cylinder as a function of space at final time, and (b) surface plot of temperature of a cylinder as a function of space at halfway time.

We also illustrate how complex shapes like a turret can be printed using our technology**.** The results in **Figure 4.14 (a)** indicate that complex structures with high resolution are achievable with this technology. Note that the resolution these results is limited by the simulation mesh size rather than the nozzle size or heat source range. The final cured structure is remarkably similar to the input print path **(Figure 4.14 (b)**), allowing engineers to produce structures that are similar to the original CAD design. I am working on refining simulation parameters, as well as increasing the mesh size of this simulation to achieve a higher resolution image.

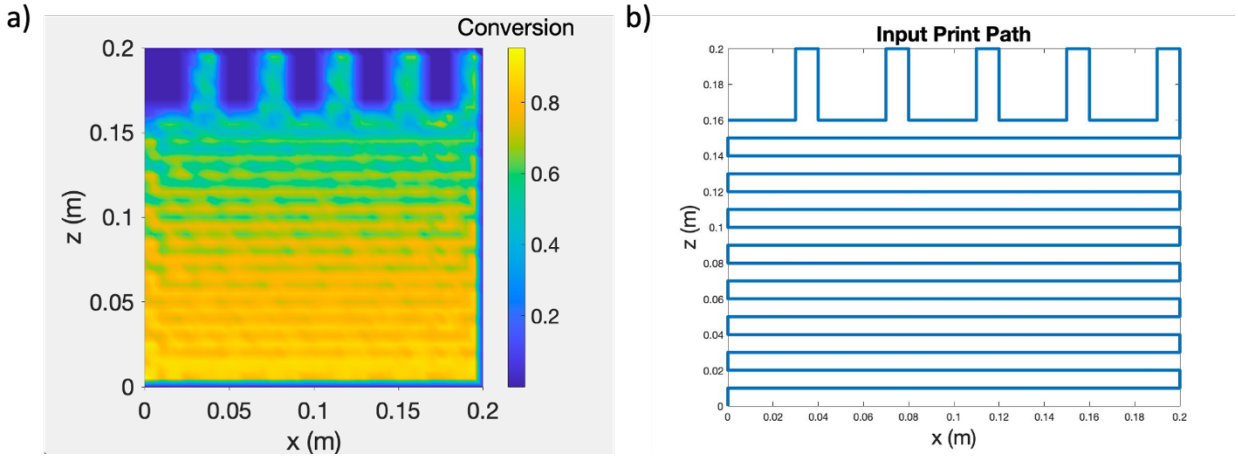

Figure 4.14: (a) Surface plot of conversion of a turret as a function of space at final time, and (b) Plot of the x and y locations of the input print path and heat source path.

4.3. Conclusion

In this study, we demonstrate that the use of a co-planar RF applicator, which generates an electric field, to rapidly heat and cure DIW-printed, nano-filled epoxy composites. This novel method avoids the need for post-curing or ovens for manufacturing of thermoset parts, thereby providing an energy efficient alternative for manufacturing thermoset parts that does not rely on altering resin chemistry or adding viscosifying agents. Our proposed method involves a layer-by-layer, print and cure cycle which allows for printing of high resolution, multi-layered structures. Each layer is partially cured using RF heating before a new layer is deposited; this allows the printed structure to maintain its integrity and hold its own weight as more layers are printed on top. Commercial epoxy resin with varied nano-filler loadings were examined as DIW candidates. Rheological characterization was used to assess curing kinetics and printing behavior. Our RF-printed samples show superior mechanical properties compared to a conventional oven cured sample. The thermo-mechanical properties, surface finish, and shape retention of RF-cured samples were evaluated and found to be comparable against samples conventionally cured in an oven. Cross-sectional SEM images indicate a more uniform morphology in the sample volumetrically cured using RF heating. Furthermore, simulation results show that this additive manufacturing technique can be used for printing complex structures, eliminating the limitation of oven-curing for 24+ hours; and altering resin chemistries or adding viscosity modifying agents to make the resin ‘printable’. We are utilizing findings from simulations to optimize the printing process and achieve better quality prints with sharper corners, higher resolution, and better structural integrity. These findings show that localized heating and curing of thermosetting resins

is possible using RF heating, addressing one of the longstanding problems in thermoset additive manufacturing.

Chapter 5: Thesis Conclusion

In this report, we studied the reaction kinetics of bisphenol A diglycidyl ether (DGEBA) and curing agent (Jeffamine T403), and demonstrated new techniques to print multi-layered structures using localized RF heating and curing.

The isothermal curing of epoxy-CNT system was characterized using rheo-kinetics and DSC. The Kamal-Sourour model was used to describe the rheo-kinetic behavior of the system, and this model was verified through DSC measurements performed at the same isothermal temperatures. Similar values for curing reaction rate constants and activation energies were obtained from rheology and DSC; however, the curing profile and curing time of epoxy-CNT samples differed due to different basis of curing degree calculations. We also used rheology to analyze RF-heated epoxy-CNT samples by monitoring the changes of G', G'', and complex viscosity after specified RF exposure times. These measurements confirm that RF exposure allows for rapid, volumetric heating and curing that are significantly faster than conventional techniques. Rheological findings and kinetic modeling of these nano-filled epoxy systems will enable predictive design for 3D printing of thermosetting polymers using RF or other out-of-oven, volumetric heating methods.

Our study of selective RF heating and curing of thermosetting resins demonstrates that localized, radio-frequency heating can rapidly heat and cure thermosetting epoxies. In contrast to previous studies where free-form printing in a resin reservoir has been investigated, we demonstrated multi-layered printing of thermosetting epoxies based on localized heating rather than localized photopolymerization. Our RF-printed samples show superior mechanical properties compared to a conventional oven cured sample. The thermo-mechanical properties

of an RF-printed sample are comparable to a conventionally cured sample of the same composition. Cross-sectional SEM images indicate a more uniform morphology in the sample volumetrically cured using RF heating. Furthermore, simulation results show that this additive manufacturing technique can be used for printing complex structures, eliminating the limitation of oven-curing in a mold. These findings show that localized heating and curing of thermosetting resins is possible using RF heating, addressing one of the longstanding problems in thermoset additive manufacturing.

In the currently ongoing study, we demonstrate that the use of a co-planar RF applicator, which generates an electric field, to rapidly heat and cure DIW-printed, nano-filled epoxy composites. This novel method avoids the need for post-curing or ovens for manufacturing of thermoset parts, thereby providing an energy efficient alternative for manufacturing thermoset parts that does not rely on altering resin chemistry or adding viscosifying agents. Our proposed method involves a layer-by-layer, print and cure cycle which allows for printing of high resolution, multi-layered structures. Each layer is partially cured using RF heating before a new layer is deposited; this allows the printed structure to maintain its integrity and hold its own weight as more layers are printed on top. Commercial epoxy resin with varied nano-filler loadings were examined as DIW candidates. Rheological characterization was used to assess curing kinetics and printing behavior. Our RF-printed samples show superior mechanical properties compared to a conventional oven cured sample. The thermo-mechanical properties, surface finish, and shape retention of RF-cured samples were evaluated and found to be comparable against samples conventionally cured in an oven. Cross-sectional SEM images indicate a more uniform morphology in the sample volumetrically cured using RF heating. Furthermore, simulation results

show that this additive manufacturing technique can be used for printing complex structures, eliminating the limitation of oven-curing for 24+ hours; and altering resin chemistries or adding viscosity modifying agents to make the resin 'printable'. We are optimizing the printing process to achieve sharper corners, higher resolution, and better structural integrity in our prints by using findings from simulations to guide us. Overall, our findings in this study show that DIW printing and RF heating and curing of thermosetting resins is possible, thereby addressing one of the longstanding problems in thermoset additive manufacturing.

Appendix: MATLAB codes

A.1. Chapter 3: Texas A&M logo MATLAB code

```
function [] = epoxy_heat_time2Dsc_TAMU
close all;
clear;
clc;
%parameters
par.Ny = 61;
par.Nx = 61;
par.Nt = 51;
par.N = par.Nx*par.Ny;

%wand location table of [t,x,y] changing w time

finaltime = 15600; %sec, total time to simulate
par.wandtime = 15600; %sec, how long is wand on
par.wandrange = 0.002; %m, how far does wand volumetric heating extend
par.systemrange = 0.2; %m, how far does system extend
par.systemlength = 0.2; %m
par.Ttarget = 523;
par.wandpowerstrength = 1; %this is wandpower/rho/Cp [degC/s]
%how much heat does wand generate (temp/time)

par.x = linspace(0,par.systemrange,par.Nx);
par.y = linspace(0,par.systemlength,par.Ny);
t = linspace(0,finaltime,par.Nt);
par.table = wandlocation_TAMU(t,par); %% SHAPE Function Call

M = speye(par.N*2); %
%create mass matrix; BCs for temperature: dTdy or dTdz = 0 on all
sides
for i = 1:par.Nx
    for j = 1:par.Ny
        n = par.Nx*(j-1) + i;
       % M = 0 at all sides faces
         if i==1 || i==par.Nx || j==1 || j==par.Ny
          M(n,n) = 0;
       % M = 1 inside
         else
             M(n,n) = 1;
         end
    end
end

Tinitial = zeros(1,par.N)+298; %initial T = 25C = 298K
Xinitial = Tinitial*0+1e-10; %initial X = 0 everywhere
opt = odeset('Mass', M);

tic;
```

```
Zinitial = [Tinitial Xinitial]; %T,X initial values
[t,Z] = ode15s(@subf,t,Zinitial,opt,par);
T = Z(:,1:par.N); % 49x2601
X = Z(:,(par.N+1):end); % 49x2601
% SIZE Z: 49x5202
T=real(T);
X=real(X);
toc;


save('results_tamu_t.mat','t')
save('results_tamu_T.mat','T')
save('results_tamu_X.mat','X')

end

%%% Subfunction %%%

function f = subf(t,Z,par)
%Z is the vector of variables at that moment in time
f=Z*0;%initialize
%unpack T, X
T = Z(1:par.N);
X = Z((par.N+1):end);
X=real(X);T=real(T);

%density of uncured polymer
rho = 900; %kg/m^3
%heat capacity of polymer
Cp = 2000; %J/kg/K
%thermal conductivity
k = 0.2; %W/m/K
%alpha
alpha = k/rho/Cp; %thermal diffusivity, m^2/s. This was 0.01 in
earlier version
dx = par.x(2)-par.x(1); %m
dy = par.y(2)-par.y(1); %m

%kinetics inputs (DSC PARAMETERS)
k1base = 0; %DSC value
k2base = 0.00276; %DSC value
mx = 0.352; % 80C
nx = 1; % 80C
E1 = 17520.0922; %DSC data
E2 = 33043.1616; %DSC data
R = 8.314; %J/mol*K
Tbase = 80+273; %K, Tbase is 80C
dHrxnbase = 396.5*1000; %J/kg*K (at 42.6C = 315.6K)


% convection + heat into glass conduction
thickness = 0.002; %thickness = 2 mm
h = 30; %W/m^2/K ____ calculate using laminar flow correlations
```

```
kglass = 1.4; %W/m*K
rhoGlass = 2500; %kg/m^3
cpGlass = 750; %J/kg*K
alpha_glass = kglass/(rhoGlass*cpGlass); %m^2/s

k1 = zeros(length(par.Nx));
k2 = zeros(length(par.Nx));
dHrxn = zeros(length(par.Nx));

%k
for i = 1:par.Nx
    for j = 1:par.Ny
        n = par.Nx*(j-1) + i;

     k1(n) = k1base*exp((E1/R)*(1/Tbase - 1/T(n)));
     k2(n) = k2base*exp((E2/R)*(1/Tbase - 1/T(n)));
     dHrxn(n) = dHrxnbase + 0*((T(n) - 315.6));
     %k1 and E1 are close to experiment in the 80-100 C range

    end
end

%T ODEs
dTdt = T*0;
%BCs: dTdt = 0 on all sides

%dT/dt without the wand
for i = 1:par.Nx
    for j = 1:par.Ny
       n = par.Nx*(j-1) + i;
       if i == 1 || j==1 || i == par.Nx || j == par.Ny %boundaries
           if i == 1  % left boundary
               dTdt(n) = (T(n) - T(n+1))/dy;
           elseif i == par.Nx         % right boundary
               dTdt(n) = (T(n) - T(n-1))/dy;
           elseif j == 1         % bottom
               dTdt(n) = (T(n) - T(n+par.Ny))/dz;
           elseif j == par.Ny         % top
               dTdt(n) = (T(n) - T(n-par.Ny))/dz;
           end
       else
        dTdt(n) = (alpha*(T(n-1)-2*T(n)+T(n+1))/dy^2) + ... % node
right/left
(alpha*(T(n-par.Ny)-2*T(n)+T(n+par.Ny))/dz^2) - ... % node up/down
(h/rho/Cp/thickness*(T(n)-298)) - (alpha_glass*(T(n)-
298))/(thickness^2) + ((k1(n) + k2(n)*(X(n)^mx))*(1-
X(n))^nx)*dHrxn(n)/Cp;
       end
    end
end

    % Proportional Control
    par.wandpower = 0;
```

```
    if par.Ttarget > max(T) %max T over all space
          par.wandpower = par.wandpowerstrength*abs(par.Ttarget -
max(T));  %K = wandpower
    end

xwand = interp1(par.table(:,1),par.table(:,2),t);
ywand = interp1(par.table(:,1),par.table(:,3),t);
connect_dots = interp1(par.table(:,1),par.table(:,4),t);

wand_location = [xwand ywand];

%connect dots CHECK
if connect_dots < 1e-3 %turn it off if it's going from 0 to 0
    par.wandpower = 0;
else
    par.wandpower = par.wandpower;
end

for i = 1:par.Nx
    for j = 1:par.Ny
        n = par.Nx*(j-1) + i;
        node_location = [par.y(i) par.z(j)];

     if norm(node_location - wand_location) < par.wandrange &&
(t<par.wandtime)
        dTdt(n) = dTdt(n) + par.wandpower; %volumetric heat
    end
   end
end


% X ODEs
dXdt = X*0;
for i = 1:par.Nx
    for j = 1:par.Ny
        n = par.Nx*(j-1) + i;

    dXdt(n) = (k1(n)+(k2(n)*X(n)^mx)) * (1-X(n))^nx;

    end
end

f = [dTdt;dXdt];

end
```

A.2. Chapter 3: Helix/Spring MATLAB code

```
function [Xplot3] = epoxy_heat_time3D_alpha_sc()
%this is the one with the alpha air
close all;
clear;
clc;

%parameters
par.Nx = 15;
par.Ny = 15;
par.Nz = 25;
par.Nt = 40;
par.N = par.Nx*par.Ny*par.Nz;

finaltime = 5175; %sec, total time to simulate
par.wandtime = 5175; %sec, how long is wand on
par.wandrange = 0.015; %m, how far does wand volumetric heating extend
par.systemrange = 0.2; %m, how far does system extend
par.systemlength = 0.2; %m
par.systemdepth = 0.25; %m

par.Ttarget = 543;
par.wandpowerstrength = 1; %this is wandpower/rho/Cp.
%how much heat does wand generate (temp/time)

par.x = linspace(-par.systemrange,par.systemrange,par.Nx);
par.y = linspace(-par.systemlength,par.systemlength,par.Ny);
par.z = linspace(-0.1,par.systemdepth,par.Nz);
t = linspace(0,finaltime,par.Nt);
par.table = wandlocation_3D_helix(t,par); %% SHAPE Function Call
%wand location table of [t,x,y,z] changing w time

M = speye(par.N*2);
%create mass matrix; BCs for temperature: dTdy or dTdz = 0 on all
sides
for i = 1:par.Nx
    for j = 1:par.Ny
        for k = 1:par.Nz
            n = par.Nx*(j-1) + i + par.Nx*par.Ny*(k-1);
            % M = 0 at all sides faces
            if i==1 || i==par.Nx || j==1 || j==par.Ny || k==1 ||
k==par.Nz
                M(n,n) = 0;
            % M = 1 inside
            else
                M(n,n) = 1;
            end
        end
    end
end
```

```
Tinitial = zeros(1,par.N)+298; %initial T = 25C = 298K
Xinitial = Tinitial*0+1e-10; %initial X = 0 everywhere
opt = odeset('Mass',M);

tic;
Zinitial = [Tinitial Xinitial]; %T,X initial values
[t,Z] = ode15s(@subf,t,Zinitial,opt,par);
T = Z(:,1:par.N); % 49x2601
X = Z(:,(par.N+1):end); % 49x2601
% SIZE Z: 49x5202
T=real(T);
X=real(X);
toc;

%%%results save

save('results_helix_t.mat','t')
save('results_helix_T.mat','T')
save('results_helix_X.mat','X')
end


function f = subf(t,Z,par)
%Z is the vector of variables at that moment in time
%f=Z*0;%initialize
%unpack T, X
T = Z(1:par.N);
X = Z((par.N+1):end);
X=real(X); T=real(T);

%density of uncured polymer
rho = 900; %kg/m^3
%heat capacity of polymer
Cp = 2000; %J/kg/K
%thermal conductivity
k = 0.2; %W/m/K
%alpha
alpha = k/rho/Cp; %thermal diffusivity, m^2/s.

dx = par.x(2)-par.x(1); %m
dy = par.y(2)-par.y(1); %m
dz = par.z(2)-par.z(1); %m

%kinetics inputs (DSC PARAMETERS)
k1base = 0; %DSC value
k2base = 0.00276; %DSC value
mx = 0.352; % 80C
nx = 1; % 80C
E1 = 17520.0922; %DSC data
E2 = 33043.1616; %DSC data
R = 8.314; %J/mol*K
Tbase = 80+273; %K, Tbase is 80C
dHrxnbase = 396.5*1000; %J/kg*K (at 42.6C = 315.6K)
```

```
% convection + heat into glass conduction parameters
thickness = 0.002; %thickness = 2 mm
h = 30; %W/m^2/K
kglass = 1.4; %W/m*K
rhoGlass = 2500; %kg/m^3
cpGlass = 750; %J/kg*K
alpha_glass = kglass/(rhoGlass*cpGlass); %m^2/s
alpha_air = 22.5e-6; %m^2/s at 300K for stagnant air

rhoAir = 1.1614; %kg/m3
cpAir = 1007; %J/kg*K
conv_air = (dz*h)/(rhoAir*cpAir);

%T ODEs
dTdt = T*0;

%BCs: no flux

xwand = interp1(par.table(:,1),par.table(:,2),t);
ywand = interp1(par.table(:,1),par.table(:,3),t);
zwand = interp1(par.table(:,1),par.table(:,4),t);

wand_location = [xwand ywand zwand];

%node location where the interface is:
[zinterface,kinterface] = max(par.z(par.z < zwand));

alphavar = T*0;%vector of alpha values
for i = 1:par.Nx
    for j = 1:par.Ny
        for k = 1:par.Nz
               n = par.Nx*(j-1) + par.Nx*par.Ny*(k-1) + i;
               if k <= kinterface
                    alphavar(n)= alpha;
               else
                   alphavar(n)= conv_air;
               end
        end
    end
end

%dT/dt without the wand
for i = 1:par.Nx
    for j = 1:par.Ny
        for k = 1:par.Nz
               n = par.Nx*(j-1) + par.Nx*par.Ny*(k-1) + i;
               k1(n) = k1base*exp((E1/R)*(1/Tbase - 1/T(n)));
               k2(n) = k2base*exp((E2/R)*(1/Tbase - 1/T(n)));
               dHrxn(n) = dHrxnbase + 0*((T(n) - 315.6));

            if i==1 || j==1 || k==1 || i==par.Nx || j==par.Ny ||
k==par.Nz %boundaries
```

```
                if i == 1 % east
                    dTdt(n) = alpha*(T(n) - T(n+1))/dx -
((alpha_glass*(T(n)-298))/(thickness));
                elseif i == par.Nx % west
                    dTdt(n) = alpha*(T(n) - T(n-1))/dx -
((alpha_glass*(T(n)-298))/(thickness));
                elseif j == 1 % north
                    dTdt(n) = alpha*(T(n) - T(n+par.Nx))/dy -
((alpha_glass*(T(n)-298))/(thickness));
                elseif j == par.Ny % south
                    dTdt(n) = alpha*(T(n) - T(n-par.Nx))/dy -
((alpha_glass*(T(n)-298))/(thickness));
                elseif k == 1 % bottom
                    dTdt(n) = alpha*(T(n) - T(n+par.Nx*par.Ny))/dz -
((alpha_glass*(T(n)-298))/(thickness));
                elseif k == par.Nz
                    dTdt(n) = alpha*(T(n) - T(n-par.Nx*par.Ny))/dz +
((h/rho/Cp*(T(n)-298)));

                end
            else     %interior

                if k > kinterface
                        dTdt(n) = 0;
                else
                    dTdt(n) = (alphavar(n)*(T(n-1)-
2*T(n)+T(n+1))/dx^2) + ... % node east/west
(alphavar(n)*(T(n-par.Nx)-2*T(n)+T(n+par.Nx))/dy^2) + ... % node
north/south

((alphavar(n)+alphavar(n+par.Nx*par.Ny))/2*(T(n+par.Nx*par.Ny)-
T(n))/dz ... -(alphavar(n)+alphavar(n-par.Nx*par.Ny))/2*(T(n)-T(n-
par.Nx*par.Ny))/dz)/dz + ... % node top/bottom
((k1(n) + k2(n)*(X(n)^mx))*(1-X(n))^nx)*dHrxn(n)/Cp;

                end
            end
        end
    end
end


    % Proportional Control
    par.wandpower = 1e-3;
    if par.Ttarget > max(T) %max T over all space (change to different
variable ~= Ttarget)
          par.wandpower = par.wandpowerstrength*abs(560 - max(T));  %K
= wandpower
    end

for i = 2:par.Nx-1
    for j = 2:par.Ny-1
        for k = 2:par.Nz-1
```

```
        n = par.Nx*(j-1) + par.Nx*par.Ny*(k-1) + i;
        node_location = [par.x(i) par.y(j) par.z(k)];
            if k <= kinterface %only stuff in the resin
                if norm(node_location - wand_location) < par.wandrange
&& (t<par.wandtime)
                    dTdt(n) = dTdt(n) + par.wandpower*exp(-
(norm(node_location - wand_location))/par.wandrange); %volumetric heat
source
                end
            end

        end
    end
end

% X ODEs
dXdt = X*0;
for i = 1:par.Nx
    for j = 1:par.Ny
        for k = 1:par.Nz
            n = par.Nx*(j-1) + par.Nx*par.Ny*(k-1) + i;
            if k <= kinterface   %on the top or in the resin
                 if T(n) < 323
                        dXdt(n) = 0;
                 else
                        dXdt(n) = (k1(n)+(k2(n)*X(n)^mx)) * (1-
X(n))^nx;
                 end
            end
        end
    end
end

f = [dTdt;dXdt];
end
```

A.3. Chapter 4: Wall MATLAB code

```
function [] = hyrel_simulation_complex_v10_final
close all;
clear;
clc;
%parameters
par.Nx = 41;
par.Nz = 41;
par.Nt = 30;
par.N = par.Nx*par.Nz;

finaltime = 7000; %sec, total time to simulate
par.wandtime = 5350; %sec, how long is wand on
par.wandrange = 0.002; %m, how far does wand volumetric heating extend
par.systemrange = 0.02; %m, how far does system extend
par.systemlength = 0.02; %m     [2D]
par.Ttarget = 423; %150 C to start
par.wandpowerstrength = 1; % this is wandpower/rho/Cp. degC/s
%how much heat does wand generate (temp/time)

par.x = linspace(0,par.systemrange,par.Nx);
par.z = linspace(0,par.systemlength,par.Nz);
t = linspace(0,finaltime,par.Nt);
% SHAPE Function Call
par.table = wandlocation_wall(t,par);
%wand location table of [t,x,z] changing w time
par.state = state_calculator(t,par);
% calculate state - epoxy or air

statemap = zeros(par.Nx,par.Nz);
for i = 1:par.Nx
    for j = 1:par.Nz
        n = par.Nx*(j-1) + i;
        statemap(i,j) = par.state(n);
    end
end
figure
surf(par.x,par.z,statemap');
xlabel('x'); ylabel('z')
colorbar;
view(0,90);

M = speye(par.N*2);
%create mass matrix; BCs for temperature: dTdx or dTdz = 0 on all
sides
for i = 1:par.Nx
    for j = 1:par.Nz
        n = par.Nx*(j-1) + i;
       % M = 0 at all sides faces
         if i==1 || i==par.Nx || j==1 || j==par.Nz
          M(n,n) = 0;
```

```
       % M = 1 inside
         else
             M(n,n) = 1;
         end
    end
end

Tinitial = zeros(1,par.N)+298; %initial T = 25C = 298K
Xinitial = Tinitial*0+1e-10; %initial X = 0 everywhere
opt = odeset('Mass', M);

tic;
Zinitial = [Tinitial Xinitial]; %T,X initial values
[t,Z] = ode15s(@subf,t,Zinitial,opt,par);
T = Z(:,1:par.N); % 49x2601
X = Z(:,(par.N+1):end); % 49x2601
% SIZE Z: 49x5202
T=real(T);
X=real(X);
toc;

save('results_wall1_t.mat','t')
save('results_wall1_T.mat','T')
save('results_wall1_X.mat','X')
end

%%% Subfunction %%%

function f = subf(t,Z,par)
%Z is the vector of variables at that moment in time
f=Z*0; %initialize

%unpack T, X
T = Z(1:par.N); %1x2601
X = Z((par.N+1):end); %1x2601
X=real(X);T=real(T);

%density of uncured polymer
rho = 900; %kg/m^3
%heat capacity of polymer
Cp = 2000; %J/kg/K
%thermal conductivity
k = 0.2; %W/m/K
%alpha
alpha = k/rho/Cp; %thermal diffusivity, m^2/s
dx = par.x(2)-par.x(1); %m
dz = par.z(2)-par.z(1); %m     [2D]

%kinetics inputs (DSC PARAMETERS)
k1base = 0; %DSC value
k2base = 0.00276; %DSC value
mx = 0.352; % 80C
nx = 1; % 80C
```

```
E1 = 17520.0922; %DSC data
E2 = 33043.1616; %DSC data
R = 8.314; %J/mol*K
Tbase = 80+273; %K, Tbase is 80C
dHrxnbase = 396.5*1000; %J/kg*K (at 42.6C = 315.6K)


% convection + heat into glass conduction
thickness = 0.001; %thickness = 2 mm
h = 30; %W/m^2/K

kglass = 1.4; %W/m*K
rhoGlass = 2500; %kg/m^3
cpGlass = 750; %J/kg*K
alpha_glass = kglass/(rhoGlass*cpGlass); %m^2/s

alpha_air = 22.5e-6; %m^2/s at 300K for stagnant air
rhoAir = 1.1614; %kg/m3
cpAir = 1007; %J/kg*K
conv_air = (dz*h)/(rhoAir*cpAir); %alpha-convection air term

k1 = zeros(length(par.Nz));
k2 = zeros(length(par.Nz));
dHrxn = zeros(length(par.Nz));

%k
for i = 1:par.Nx
    for j = 1:par.Nz
        n = par.Nx*(j-1) + i;

        k1(n) = k1base*exp((E1/R)*(1/Tbase - 1/T(n)));
        k2(n) = k2base*exp((E2/R)*(1/Tbase - 1/T(n)));
        dHrxn(n) = dHrxnbase + 0*((T(n) - 315.6));
    end
end

% wand location and z-interface location
xwand = interp1(par.table(:,1),par.table(:,2),t);
zwand = interp1(par.table(:,1),par.table(:,3),t);
connect_dots = interp1(par.table(:,1),par.table(:,4),t);

wand_location = [xwand zwand];
[zinterface, jinterface] = max(par.z(par.z < zwand));

% varying alpha
alphavar = T*0; %vector of alpha values
for i = 2:par.Nx-1
    for j = 2:par.Nz-1
        n = par.Nx*(j-1) + i;
        %state(n)
        if par.state(n) < t
             alphavar(n) = alpha; %in resin
        else
```

```
             alphavar(n) = alpha_air; %in air
        end
    end
end

%T ODEs
dTdt = T*0;
%BCs [2D] dTdt = 0 on all sides

%dT/dt without the wand
for i = 1:par.Nx
    for j = 1:par.Nz
       n = par.Nx*(j-1) + i;
       if i == 1 || j==1 || i == par.Nx || j == par.Nz %boundaries
           if i == 1 % left boundary
               dTdt(n) = alphavar(n)*(T(n) - T(n+1))/dx +
((h/rho/Cp*(T(n)-298)));
           elseif i == par.Nx % right boundary
               dTdt(n) = alphavar(n)*(T(n) - T(n-1))/dx +
((h/rho/Cp*(T(n)-298)));
           elseif j == 1 % bottom
               dTdt(n) = alphavar(n)*(T(n) - T(n+par.Nx))/dz +
((alpha_glass*(T(n)-298))/(thickness));
           elseif j == par.Nz % top
               dTdt(n) = alphavar(n)*(T(n) - T(n-par.Nx))/dz +
((h/rho/Cp*(T(n)-298)));
           end
       else
            if par.state(n) < t

                 dTdt(n) = ((alphavar(n)+alphavar(n+1))/2*(T(n+1)-
T(n))/dx - ...
(alphavar(n)+alphavar(n-1))/2*(T(n)-T(n-1))/dx)/dx + ... % node
right/left
((alphavar(n)+alphavar(n+par.Nx))/2*(T(n+par.Nx)-T(n))/dz - ...
(alphavar(n)+alphavar(n-par.Nx))/2*(T(n)-T(n-par.Nx))/dz)/dz + ... %
node up/down
((k1(n) + k2(n)*(X(n)^mx))*(1-X(n))^nx)*dHrxn(n)/Cp - ...
2*(h/rho/Cp/thickness*(T(n)-298));
            else
                dTdt(n) = 0;

            end

       end

    end
end

    % Proportional Control
    par.wandpower = 0;
    if par.Ttarget > max(T) %max T over all space
```

```
          par.wandpower = par.wandpowerstrength*abs(par.Ttarget -
max(T));  %K = wandpower
    end

for i = 2:par.Nx-1
    for j = 2:par.Nz-1
        n = par.Nx*(j-1) + i;
        node_location = [par.x(i) par.z(j)];
        if par.state(n) < t %only stuff in the resin
            if norm(node_location - wand_location) < par.wandrange &&
(t<par.wandtime)
                dTdt(n) = dTdt(n) + connect_dots*par.wandpower;
                %volumetric heat source
            end
        end
    end
end


% X ODEs
dXdt = X*0;
for i = 2:par.Nx-1
    for j = 2:par.Nz-1
        n = par.Nx*(j-1) + i;
        if par.state(n) < t %only stuff in the resin
                dXdt(n) = (k1(n)+(k2(n)*X(n)^mx)) * (1-X(n))^nx;
        else
            dXdt(n) = 0;
        end
    end
end

f = [dTdt;dXdt];

end
```

References

1. Johannisson, W., D. Zenkert, and G. Lindbergh, *Model of a structural battery and its potential for system level mass savings.* Multifunctional Materials, 2019. **2**(3): p. 035002.
2. Young, R.J. and P.A. Lovell, *Introduction to polymers*. 2011: CRC press.
3. Kamal, M.R., *Thermoset Characterization for Moldability Analysis.* Polymer Engineering and Science, 1974. **14**(3): p. 231-239.
4. Pattanaik, A., M. Mukherjee, and S.B. Mishra, *Influence of curing condition on thermo-mechanical properties of fly ash reinforced epoxy composite.* Composites Part B-Engineering, 2019. **176**.
5. Sweeney, C.B., et al., *Welding of 3D-printed carbon nanotube-polymer composites by locally induced microwave heating.* Science Advances, 2017. **3**(6).
6. Vashisth, A., et al., *Continuous processing of pre-pregs using radio frequency heating.* Composites Science and Technology, 2020. **195**.
7. May, C., *Epoxy resins: chemistry and technology*. 2018: Routledge.
8. Daniel, I.M., *Engineering mechanics of composite materials*. Vol. 1994.
9. Chung, D.D., *Composite material structure and processing.* Composite Materials: Science and Applications, 2010: p. 1-34.
10. Khelifa, I., et al., *New poly(o-phenylenediamine)/modified-clay nanocomposites: A study on spectral, thermal, morphological and electrochemical characteristics.* Journal of Molecular Structure, 2019. **1178**: p. 327-332.
11. Bekyarova, E., et al., *Multiscale carbon nanotube-carbon fiber reinforcement for advanced epoxy composites.* Langmuir, 2007. **23**(7): p. 3970-3974.
12. Rafique, I., et al., *Exploration of Epoxy Resins, Hardening Systems, and Epoxy/Carbon Nanotube Composite Designed for High Performance Materials: A Review.* Polymer-Plastics Technology and Engineering, 2016. **55**(3): p. 312-333.
13. Popov, V.N., *Carbon nanotubes: properties and application.* Materials Science & Engineering R-Reports, 2004. **43**(3): p. 61-102.
14. Jacobsen, R.L., et al., *Mechanical-Properties of Vapor-Grown Carbon-Fiber.* Carbon, 1995. **33**(9): p. 1217-1221.
15. Suche, E., A. Formate, and B.P. Grady, *Carbon nanotube-Polymer composites.* 1982.
16. Sweeney, C.B., et al., *Dielectric Barrier Discharge Applicator for Heating Carbon Nanotube-Loaded Interfaces and Enhancing 3D-Printed Bond Strength.* Nano Letters, 2020. **20**(4): p. 2310-2315.
17. Anas, M., et al., *Radio frequency heating of metallic and semiconducting single-walled carbon nanotubes.* Nanoscale, 2019. **11**(19): p. 9617-9625.

18. Debnath, D., et al., *Radio frequency heating and reduction of Graphene Oxide and Graphene Oxide - Polyvinyl Alcohol Composites.* Carbon, 2020. **169**: p. 475-481.

19. Odom, M.G.B., et al., *Rapid curing and additive manufacturing of thermoset systems using scanning microwave heating of carbon nanotube/epoxy composites.* Carbon, 2017. **120**: p. 447-453.

20. Patil, N., et al., *Rapid Heating of Silicon Carbide Fibers under Radio Frequency Fields and Application in Curing Preceramic Polymer Composites.* Acs Applied Materials & Interfaces, 2019. **11**(49): p. 46132-46139.

21. Sweeney, C.B., et al., *Radio Frequency Heating of Carbon Nanotube Composite Materials.* Acs Applied Materials & Interfaces, 2018. **10**(32): p. 27252-27259.

22. Vashisth, A., et al., *Radio frequency heating and material processing using carbon susceptors.* Nanoscale Advances, 2021. **3**(18): p. 5255-5264.

23. Habib, T., et al., *Heating of Ti3C2Tx MXene/polymer composites in response to Radio Frequency fields.* Scientific Reports, 2019. **9**.

24. Tezel, G.B., et al., *Kinetics of carbon nanotube-loaded epoxy curing: Rheometry, differential scanning calorimetry, and radio frequency heating.* Carbon, 2021. **175**: p. 1-10.

25. Domínguez, J.C., *Chapter 4 - Rheology and curing process of thermosets*, in *Thermosets (Second Edition)*, Q. Guo, Editor. 2018, Elsevier. p. 115-146.

26. Cai, H.Y., et al., *Curing kinetics study of epoxy resin/flexible amine toughness systems by dynamic and isothermal DSC.* Thermochimica Acta, 2008. **473**(1-2): p. 101-105.

27. McCoy, J.D., et al., *Cure mechanisms of diglycidyl ether of bisphenol A (DGEBA) epoxy with diethanolamine.* Polymer, 2016. **105**: p. 243-254.

28. Terenzi, A., et al., *Chemorheological behaviour of double-walled carbon nanotube-epoxy nanocomposites.* Composites Science and Technology, 2008. **68**(7-8): p. 1862-1868.

29. Johnson, R.J. and R. Pitchumani, *Characterization of the Rheology and Cure Kinetics of Epoxy Resin with Carbon Nanotubes.* Frontiers in Heat and Mass Transfer, 2010. **1**(1).

30. Xie, H.F., et al., *Cure kinetics of carbon nanotube/tetrafunctional epoxy nanocomposites by isothermal differential scanning calorimetry.* Journal of Polymer Science Part B-Polymer Physics, 2004. **42**(20): p. 3701-3712.

31. Ehlers, J.E., et al., *Theoretical study on mechanisms of the epoxy - Amine curing reaction.* Macromolecules, 2007. **40**(12): p. 4370-4377.

32. Vashisth, A., et al., *Accelerated ReaxFF Simulations for Describing the Reactive Cross-Linking of Polymers.* Journal of Physical Chemistry A, 2018. **122**(32): p. 6633-6642.

33. Heinze, S. and A.T. Echtermeyer, *A Practical Approach for Data Gathering for Polymer Cure Simulations.* Applied Sciences-Basel, 2018. **8**(11).

34. Li, Q., X.Y. Li, and Y. Meng, *Curing of DGEBA epoxy using a phenol-terminated hyperbranched curing agent: Cure kinetics, gelation, and the TTT cure diagram.* Thermochimica Acta, 2012. **549**: p. 69-80.

35. Sarmah, A., et al., *Rapid Manufacturing via Selective Radio-Frequency Heating and Curing of Thermosetting Resins.* Advanced Engineering Materials, 2022.

36. Yang, K., M.Y. Gu, and Y.P. Jin, *Cure Behavior and Thermal Stability Analysis of Multiwalled Carbon Nanotube/Epoxy Resin Nanocomposites.* Journal of Applied Polymer Science, 2008. **110**(5): p. 2980-2988.

37. Abdalla, M., et al., *Cure behavior of epoxy/MWCNT nanocomposites: The effect of nanotube surface modification.* Polymer, 2008. **49**(15): p. 3310-3317.

38. Mahmoudi, M., et al., *Additive-Free and Support-Free 3D Printing of Thermosetting Polymers with Isotropic Mechanical Properties.* Acs Applied Materials & Interfaces, 2021. **13**(4): p. 5529-5538.

39. Wei, L., et al., *Fabrication of SiOC ceramic with cellular structure via UV-Assisted direct ink writing.* Ceramics International, 2020. **46**(3): p. 3637-3643.

40. Wu, T., et al., *Additively manufacturing high-performance bismaleimide architectures with ultraviolet-assisted direct ink writing.* Materials & Design, 2019. **180**.

41. Compton, B.G., et al., *Electrical and Mechanical Properties of 3D-Printed Graphene-Reinforced Epoxy.* Jom, 2018. **70**(3): p. 292-297.

42. Hmeidat, N.S., et al., *Processing and mechanical characterization of short carbon fiber-reinforced epoxy composites for material extrusion additive manufacturing.* Composites Part B-Engineering, 2021. **223**.

43. Hmeidat, N.S., J.W. Kemp, and B.G. Compton, *High-strength epoxy nanocomposites for 3D printing.* Composites Science and Technology, 2018. **160**: p. 9-20.

44. Hmeidat, N.S., et al., *Mechanical anisotropy in polymer composites produced by material extrusion additive manufacturing.* Additive Manufacturing, 2020. **34**.